A THESIS

FOR THE DEGREE OF DOCTOR OF PHILOSOPHY

Plasma Catalytic Hybrid Reactor System for Air Pollution Control

NGUYEN VAN TOAN

Major of Energy & Chemical Engineering

FACULTY OF APPLIED ENERGY SYSTEM

GRADUATE SCHOOL

JEJU NATIONAL UNIVERSITY

August - 2021

Plasma Catalytic Hybrid Reactor System for Air Pollution Control

NGUYEN VAN TOAN
(Supervised by Professor, Dr. **Young Sun Mok**)

A thesis submitted in partial fulfillment of the requirement for the degree of
Doctor of Philosophy
2021. 06
The thesis has been examined and approved.

………………………………	
Professor, Dr. **Howon Lee** Thesis Director	Department of Chemical and Biological Engineering, Jeju National University
………………………………	
Professor, Dr. **Heonju Lee** Thesis Committee Member	Department of Nuclear and Energy Engineering, Jeju National University
………………………………	
Professor, Dr. **Hyomin Lee** Thesis Committee Member	Department of Chemical and Biological Engineering, Jeju National University
………………………………	
Dr. **Duy Khoe Dinh** Thesis Committee Member	Department of Industrial Plasma Engineering, Korea Institute of Machinery and Materials
………………………………	
Professor, Dr. **Young Sun Mok** Thesis Committee Member & Supervisor	Department of Chemical and Biological Engineering, Jeju National University

June – 2021

Major of Energy & Chemical Engineering
FACULTY OF APPLIED ENERGY SYSTEM
GRADUATE SCHOOL
JEJU NATIONAL UNIVERSITY

CONTENTS

LIST OF FIGURES

LIST OF TABLES

ABBREVIATIONS

Abbreviation	Explanation
AC	Alternative Current
Ag	Silver
Al_2O_3	Alumina oxide
C_7H_{16}	n-Heptane
C_8H_8	Styrene
$C_{10}H_8$	Naphthalene
CO_2	Carbon dioxide
CO	Carbon monoxide
DBD	Dielectric barrier discharge
DC	Direct Current
EA	Ethyl acetate
EDS	Energy-dispersive X-ray Spectroscopy
FTIR	Fourier Transform Infra-Red
GC	Gas Chromatography
GHSV	Gas Hourly Space Velocity
HC	Hydrocarbon
HV	High Voltage
ID	Inner diameter
kV	Kilovolt
MFC	Mass Flow Controller
NO	Nitric oxide
NO_2	Nitrogen dioxide
NO_x	Nitrogen Oxides
NTP	Non-Thermal Plasma
OD	Outer diameter
PID	Proportional-integral-derivative
Pd	Palladium
PM	Particulate Matter

ppm	Parts per million
SCR	Selective Catalytic Reduction
SEM	Scanning electron microscopy
SIE	Specific Input Energy
VOC	Volatile Organic Compound
XRD	X-ray diffraction
ZSM5	Zeolit

ABSTRACT

The thesis focuses on investigating plasma catalytic hybrid reactors towards controlling air pollution (e.g., NO_x removal and VOC decomposition). The influence of critical process parameters on the removal process such as gas temperature, humidity, gas flow rate, hydrocarbon, energy density, and so on were investigated. The byproducts in the plasma catalytic oxidation process were also analyzed to understand the role of the plasma-activated catalytic in governing the reaction pathways according to the oxidation process. Additionally, screening of different suitable catalytic materials and suitable plasma technologies has been carried out towards practical applications.

In this study, three different processes for NO_x and soot removal, and VOC degradation using plasma catalytic hybrid are investigated. The first is the removal efficiency of NO_x and soot at a low-temperature range below 350 ℃. The key for this study is plasma-induced activation of the catalyst at relatively low temperatures, which can efficiently remove NO_x at low temperatures and fluctuating below 350 ℃. The second work has discussed the degradation of VOCs in the ambient air by using a DBD plasma reactor packed with Pd/ZSM5 catalyst that acts as both an adsorbent and catalyst. For the sake of practical application, the third work is to develop a honeycomb catalysts plasma reactor system for dealing with large amounts of air pollutions in the environment.

From the first work, an evaluation of low-temperature NO_x removal over Ag/ZSM5 and Cu/ZSM5 catalysts coupled with plasma is performed in a wide temperature range below 350 ℃. The experimental results show that the NO_x removal rate over Ag/ZSM5 was higher than that over Cu/ZSM5. The NO_x removal efficiency based on Ag/ZSM5 catalyst coupled with

plasma exceeded 80% at low operating temperatures. The oxidation of NO to NO_2 was approximately 100% at temperatures of 200–300 ℃. Furthermore, the effects of water vapor, hydrocarbons, and operating temperature on NO_x removal efficiency were also investigated. Mechanisms for low-temperature NO_x removal by plasma catalysis have also been discussed in detail. Besides, the removal of NO_x and soot simultaneously by selective catalytic reduction (HC-SCR) coupled with plasma under temperature fluctuation conditions ranging from 150-350 ℃ is also investigated. The results revealed that the HC-SCR coupled with plasma maintained high NO_x and soot reduction efficiency regardless of the temperature variations in the range from 150 to 350 ℃. In comparison, the average NO_x removal efficiency of the HC-SCR process at various SIE was varied from 37.6 to 76.6%, depending on the specific input energy (SIE).

In the second work, the styrene degradation was investigated in a DBD plasma reactor packed with Pd/ZSM5 pellets acting as both an adsorbent and a catalyst at atmospheric pressure. The effects of SIE, styrene concentration on the removal of styrene, the CO_2 selectivity, and the formation of organic and inorganic byproducts were discussed. The results demonstrated that the plasma-coupled Pd/ZSM5 catalyst significantly enhanced both the styrene oxidation and the CO_2 selectivity as compared with the plasma-alone case, greatly reducing the byproducts. The styrene degradation efficiency proportionally increased with increasing the specific input energy. Ozone formed by the plasma played an important role in the oxidation of styrene. The Pd/ZSM5 catalyst could be activated by the plasma, which greatly enhanced the performance of the styrene removal.

In the third work, a plasma-assisted catalysis reactor system comprising different types of corona discharge and honeycomb catalysts have been investigated for degradation of ethyl-acetate (EA) in the air under various parameters such as humidity, space velocity (GHSV), and temperature. The honeycomb catalyst used in this work was successfully prepared by applying

a coating of γ-alumina (γ-Al_2O_3) powder to the bare cordierite monolith on which to support the palladium (Pd) catalyst. An attempt has been made to successfully generate a large volume of uniform plasma at atmospheric pressure in the channels of the nearly practical-scale honeycomb catalyst. The results demonstrated DC honeycomb catalyst discharge is more stable and easier to operate at higher voltages under various atmospheric conditions. Furthermore, EA conversion in the DC honeycomb catalyst discharge (96%) is significantly higher than that at the given applied voltage. The by-products of EA degradation were also analyzed to understand the role of the plasma in governing the reaction pathways according to which the oxidation process of EA proceeds in the plasma discharge over the honeycomb catalyst. The honeycomb catalyst discharge renders the proposed system suitable for practical applications.

CHAPTER 1

INTRODUCTION

1.1. Overview

The emissions of NO_x, and VOC by various industrial, mobile, and natural processes are sources of air pollution and adversely affect human health. There are several problems such as photochemical smog, acid rain, and ozone layer depletion [1]–[3]. Acid rain has the potential to generate further environmental impacts such as deforestation, soil, and water acidification [4]. The component of smog can cause eye damage and throat irritation, reduce visibility, and damages plants and materials [5]. The VOCs (i.e., styrene, ethyl-acetate) are mainly emitted from industrial processes such as refineries, chemical and pharmaceutical plants, automobile manufacturers, etc [6]–[9]. Styrene is a typical VOC that is widely used in the resin and pharmaceutical industry. It has high toxicity and odorous smell and is hard to destroy due to the resonance hybrid of its benzene ring [8]. The primary sources of NO_x emission include motor vehicles (55%) and industrial, commercial combustion processes (45%) [10]. The NO_x (the sum of NO and NO_2) are considered toxic [1], [11]. Around 95% of NO_x emitted from incineration processes is NO while NO_2 is 5% [12]–[14]. However, NO is unstable and reacts readily with oxygen through photochemical oxidation to form NO_2 [15]. Thus, developing a cost-effective approach for the removal of NO_x and VOC in the air is a major environmental problem now.

In this regard, several available technologies have been applied for the control of air pollution such as absorption and adsorption, thermal incineration and catalytic oxidation, biological treatment, non-thermal plasma (NTP), or non-thermal plasma catalytic [5], [16]–[24]. Among these methods, adsorption and absorption are considered efficient technologies for the removal of VOCs from the gas stream. However, these technologies have some drawbacks such as post-treatment/reactivating and disposal of used adsorbents, which may lead to an increase in the overall cost [25]. Thermal incineration and catalytic oxidation methods require a supply of a high-temperature and catalytic deactivation represents a serious problem for these technologies [19], [26], [27]. Biological treatment is considered one of the most environmentally friendly technologies for minimizing VOCs, as it provides an economical and environmentally alternative to traditional technologies such as adsorption, thermal oxidation, and catalytic oxidation. However, their disadvantages are slow biological oxidation of less water-soluble and less biodegradable VOCs, the system is very large [28]. Catalysis is featured as a selective process, but most traditional catalysts are activated at high temperatures over 300 ℃ [29]. Indeed, commercially available catalysts hardly exhibit catalytic activity at low temperatures, behaving just like adsorbents. Moreover, the pollution itself and the partially oxidized products formed on the catalyst surface covered the active site and filled the micropores to debase the adsorption capacity of the catalyst, which would weaken and even destroy the catalytic activity, when the temperature is not enough [30].

Recently, non-thermal plasma (NTP) has been proved as a promising technique for the treatment of air pollution [16], [18], [31], [32]. The remarkable features of this technology are very efficient sources of active species at atmospheric pressure. In comparison with the other sources at lower pressures, NTP can be directly used in the ambient air without using any vacuum system [33]. A large number of strong oxidizing agents and highly reactive species are produced, capable of promoting the decomposition of gaseous pollutants, even at low temperatures [34], [35]. The dissociation and ionization of the ambient gases caused by the impact of energetic electrons in the plasma region can generate many kinds of chemically activated radicals such as oxygen radical (O), ozone (O_3), nitrogen radical (N), excited nitrogen radical (N*), and OH radicals, which strongly promoted the decomposition of pollution [16], [36]. NTP can be generated through a variety of ways including corona discharge [37], [38], microwave discharge [39], and arc/plasma torch [40], glide discharge reactors [41], and dielectric barrier discharge (DBD) [42], [43]. Among the different types of NTPs, the DBD and corona discharge for air pollution have received a lot of attention recently since it has a simple configuration and can be operated under atmospheric pressure [29], [44], [45]. However, a disadvantage of plasma technology is incomplete oxidation, which leads to the formation of unwanted degradation products (i.e., ozone, NO_x), possibly more harmful than the parent molecule, and poor energy efficiency, which is a serious obstacle towards their industrial implementation [18], [42], [46], [47].

To address these drawbacks, more effective use of NTP is possible by exploiting its inherent synergetic potential through a combination with heterogeneous catalyst as emphasized by different groups [48]–[50]. Hybrid plasma catalysis combines the advantages of high selectivity from the catalysis and rapid reaction rate from the NTP [42], [44], [51]. In addition, its simple operational procedure and economic viability in industrial applications while most of the other technologies face difficulties such as incomplete degradation, slow reaction rate, high investment and operational cost, high-temperature requirement, and so forth [16], [23]. The plasma induces the desorption and the oxidation of low-volatile products deposited on the catalyst surface, which can regenerate the catalyst. On the other hand, the catalyst with a plasma reactor can enhance product selectivity and energy efficiency [52], [53]. Especially, the catalyst can solve the problem related to the formation of unwanted byproducts while the plasma makes up for the weak points of the catalyst such as deactivation and low activity at low temperatures [42], [54], [55]. Furthermore, NO_x cannot be reduced to N_2 effectively just with electrical discharges and without the help of a catalyst [18], [56], and the power consumption for NTP for decomposition NO_x is extremely high [57]. Briefly, plasma-assisted catalysis is widely used for improved air pollutant removal efficiency and selectivity because of its simple operational procedure and economic viability in industrial applications.

Multifarious catalysts for processes using plasma such as zeolites (ZSM5) [42], [58], [59], photo-catalyst (TiO_2) [30], [60], and alumina (γ-Al_2O_3) [45], [61]–[63] loaded with different metals such as Ag [26], [43], [64], Pd [42], [65] catalysts have been used for air purification. Among the common catalysts are porous adsorbents such as zeolite (ZSM5) and γ-Al_2O_3 [66]. It has shown outstanding properties with respect to specific surface area and adsorption capacity [59]. Zeolite materials are advantageous due to their acidic nature and shape-selective behavior, which had unique micropores, cavies, and channels in their frame structures, which have the size of micropores range from 3 to 20 Å [67], [68], whereas could be adsorbed the pollution molecules enter into the internal pore of catalyst. Moreover, the micro discharge in the plasma might be generated inside the catalyst pores [69]. Besides, the γ-Al_2O_3 is also a widely used catalyst supported, which combined Lewis acidity and basicity, good porosity, and high surface area [70]. The catalysts supported by noble metals or transition metal oxides have been used for NO_x removal and VOC decomposition [5], [71]–[73]. Zeolite-supported active metals are able to improve the CO_2 selectivity by facilitating the oxidation of intermediates [59], [74]. These catalysts can prolong the retention time of the VOC molecules in the plasma catalytic bed, which may lead to a higher collision probability between reactive species and VOC molecules when combined with the plasma [36], [74]. The excellent adsorption ability of catalysts could improve pollution removal in the plasma [75]. Among the noble metal or transition metal, oxides-based catalysts, silver [76], [77], and palladium [42], [74], [78] containing catalysts have exhibited interesting activity in the removal of NO_x and

VOC at low temperatures.

The selective catalytic reduction (SCR) of NO_x can obtain high conversion with several reducing agents such as H_2, NH_3, urea, and hydrocarbon (HC) at high operating temperatures (300–400 ℃) [79]–[84]. Among these agents, the use of HC-SCR for NO_x removal can be considered to be easier to apply due to the practicability and cost-effectiveness. The exhaust gas of diesel engines usually contains HC and particulate matter [85], which can be directly used as a reducing agent for NO_x reduction. The n-heptane is used as a reducing agent simulant in this work, which has a cetane number and ignition properties comparable to that of diesel fuel, and is a major component in reference and surrogate fuels for diesel fuel [86]–[88]. The suitable temperature window of operation for light-duty diesel engine exhaust gas streams is the range of 150–300 °C [89]. To date, a high NO_x removal rate at low operating temperatures (<300 ℃) and fluctuating gas temperatures are still challenges. To address this problem, a plasma catalyst hybrid uses for NO_x and soot removal in a wide temperature range below 350 °C.

1.2. Aim of the work

The main purpose of this work is special focus on plasma catalytic hybrid reactor system for Air pollution control. The influence of various parameters (such as water vapor, operating temperature, and gas flow rate) on the NO_x removal and VOC decomposition efficiency were investigated. Screening for various suitable catalytic materials (e.g., pellets, honeycomb catalyst) for incorporation with other types of discharge plasma (e.g. DBD, AC & DC corona) towards improving efficiency and deploying industrial applications have been investigated. Specific objectives are based on the different processes as follow:

➢ Firstly, removal of NO_x and Soot by selective catalytic reduction (HC-SCR) coupled with plasma under low-temperature conditions and fluctuate below 350 ℃. Understand the plasma-catalytic NO_x removal mechanisms at low temperatures.

- Secondly, the plasma-assisted catalyst for VOC degradation in the air. Understand the plasma catalytic oxidation mechanism through byproducts analysis.
- Lastly, development of a plasma catalytic reactor configuration based on honeycomb corona discharge (HCD) toward practical application.

1.3. Organization of the thesis

The thesis is organized into six chapters.

Chapter 1- This chapter presents an overview of the literature on air pollution, several methods of air pollution control, and the advantage of the plasma catalytic techniques compared to traditional methods in close detail. From there, the research objectives were proposed in detail.

Chapter 2- The experimental setup, materials, and analysis methods have been described in detail. Depending on the study, the experimental setup has been adapted to the goals of that study and details will be shown in related chapters.

Chapter 3- In this chapter, A modeling for hydrocarbon (HC) – based selective catalytic reduction (SCR) of NO_x reduction couple with plasma under low-temperature and temperature fluctuation conditions are investigated. The influence of various operational parameters such as water vapor, hydrocarbon, and temperature on NO_x removal was discussed. Commonly used catalyst support materials such as ZSM5, Al_2O_3 have been used in this work.

Chapter 4- In this chapter, the degradation of VOC is investigated in the DBD plasma catalytic hybrid reactor at atmospheric pressure. The catalyst used in this study is Pd/ZSM5, which acts as both an adsorbent and a catalyst at atmospheric pressure. The ozone formation and decomposition, and the byproducts formation were analyzed in detail.

Chapter 5- Towards practical application, a plasma-catalytic reactor configuration (HCD) has been developed based on honeycomb catalysts to handle large flows, which can be scaled-up or commercial. The effect of humidity, gas velocity, and reactor temperature on the discharge characteristic and VOC decomposition was investigated in detail. Two types of plasma sources (i.e., AC, and DC) are used in this study.

Chapter 6- Several conclusions present in this chapter, and some recommendations for future work.

CHAPTER 2

METHODOLOGY

2.1. Selected plasma catalytic reactor configurations

2.1.1. DBD reactor

The DBD plasma catalytic reactor is illustrated in Fig. 2.1. It was comprised of a cylindrical ceramic tube that served as a dielectric layer separating the high voltage electrode and the outer ground electrode. The reactor consists of two electrodes, a high-voltage electrode, and a grounded electrode. The steel-threaded rod acting as the high voltage electrode (discharging electrode) was placed at the center of the ceramic tube. A thin copper foil wrapped around the outer surface of the ceramic tube served as the ground electrode.

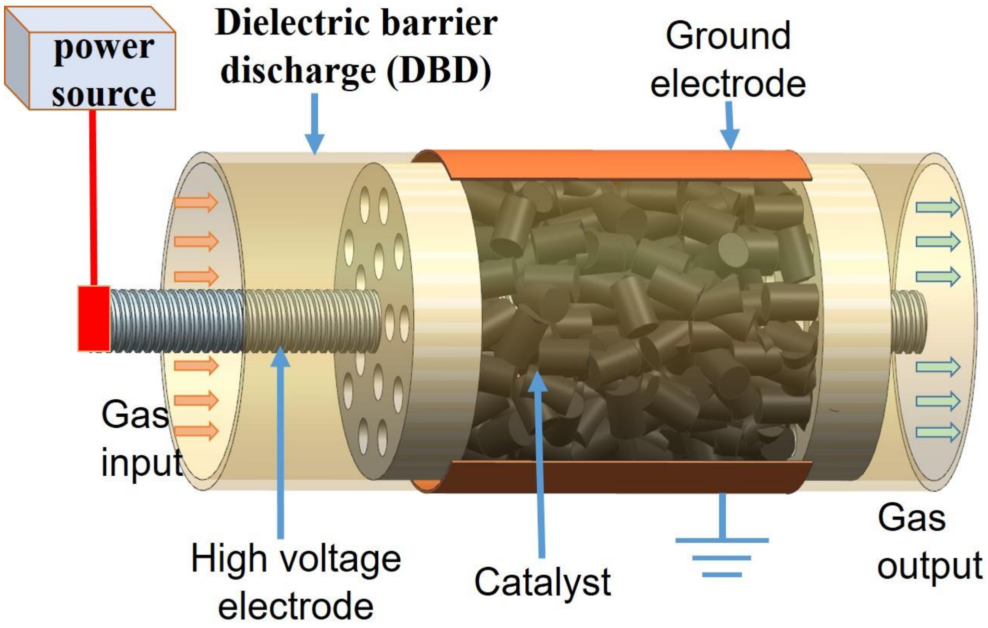

Fig. 2.1. Illustration of the DBD plasma catalysts reactor.

A high-voltage alternating current (AC) operated at 400 Hz was applied across the electrodes of the DBD packed-bed reactor, which was supplied by a frequency converter (Sampoong Power Co., Ltd., Incheon, Korea) and integrated with a transformer (Taehwa Electric Co., Seoul, Korea). The DBD reactor was filled with different catalysts in the space between the dielectric barrier and the electrode to construct the plasma catalysis systems, depending on specific experiments. The advantage of this system is that a relatively low applied voltage can be used to form a plasma over a relatively large separation of the electrodes (∼5 cm) [90]. Furthermore, the duration of residence has been proposed as one of the criteria affecting the efficiency of the process [91]. The residence time can be improved by using the dielectric-packed pellets inside the reactor. More details about the DBD reactor parameters used in this work are summarized in Table 1.

Table 1. Parameters of DBD plasma catalysts reactors in this work

Experiments	**Dielectric barrier**		**Discharge length** (mm)	**HV electrode** OD (mm)	**Catalysts packed amount** (g)
	OD (mm)	ID (mm)			
Evaluation NO_x removal over Ag/ZSM5 and Cu/ZSM5	35	28	50	6	20
Removal of NO_x and Soot simulant	29	23	75	6	20
Degradation of styrene over Pd/ZSM5	30	23	70	6	10

2.1.2 Corona reactor

The corona reactor consisted of a quartz cylinder with an inner diameter of 50 mm, two perforated disk electrodes, and a monolith catalyst. Each of the two electrodes comprised a stainless-steel perforated disk (ϕ50 × 2 mm) with 65 holes (each with a diameter of 3 mm), covering both sides of the monolith. The gap between the high-voltage electrode and the monolith surface was fixed at 2 mm, whereas the distance from the ground electrode to the honeycomb surface was 0.5 mm. A frequency converter (Sampoong Power Co., Ltd., Incheon, Korea) was adjusted to supply AC power at 400 Hz. The AC voltage from the frequency converter was stepped up using a high-voltage transformer. The high-voltage DC power supply was purchased from Taehwa Electric Co., Seoul, Korea. The corona plasma reactor is illustrated in Fig. 2.2.

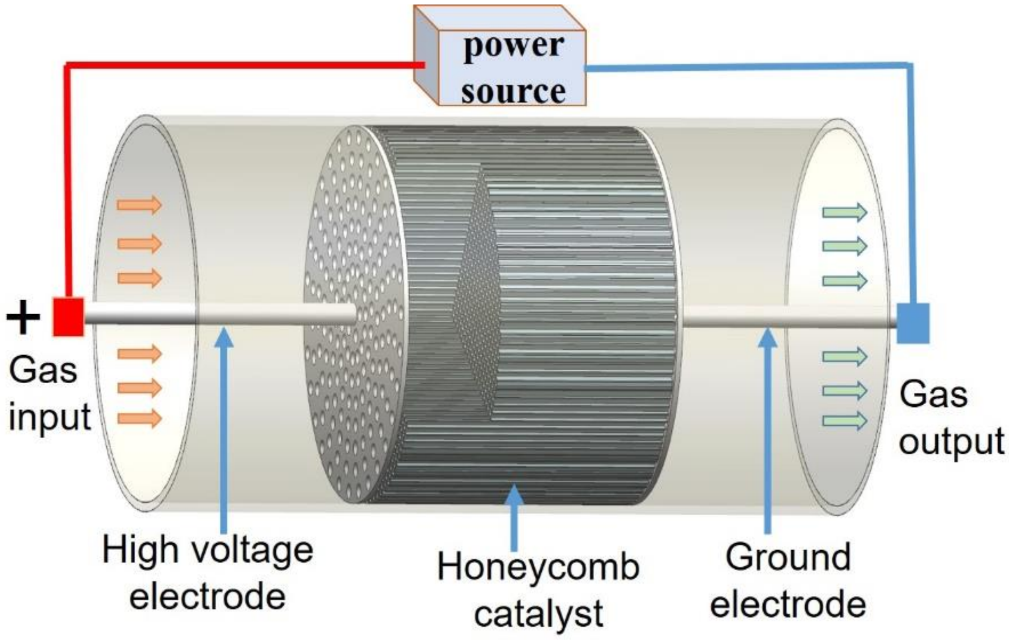

Fig. 2.2. Illustration of the corona plasma honeycomb catalysts reactor.

2.2. Experimental setup

2.2.1. General experimental setup for NO_x and Soot removal using DBD plasma catalyst reactor

The schematic diagram of the experimental setup for NO_x reduction in a fixed-bed DBD plasma reactor is shown in Fig. 2.3. The NO_x removal was performed with a synthetic exhaust gas whose composition was 10% oxygen, 3.7% H_2O, 265 ppm n-heptane (C_7H_{16}), 300 ppm NO_x (288 ppm NO and 12 ppm NO_2), and N_2 as balance. The total flow rate was 2 L/min. The concentration of n-heptane in the feed gas stream was adjusted by its vapor pressure. The temperature of the n-heptane containing flask was maintained at 15 °C. In the experiment for removal NO_x and soot simulant, 48 ppm naphthalene ($C_{10}H_8$) was diluted with the gas stream by passing a mixture of O_2 and N_2 through an Erlenmeyer flask containing naphthalene powder. The flask was kept in a water bath at 17 °C. Subsequently, the flow passed through the saturated aqueous solution

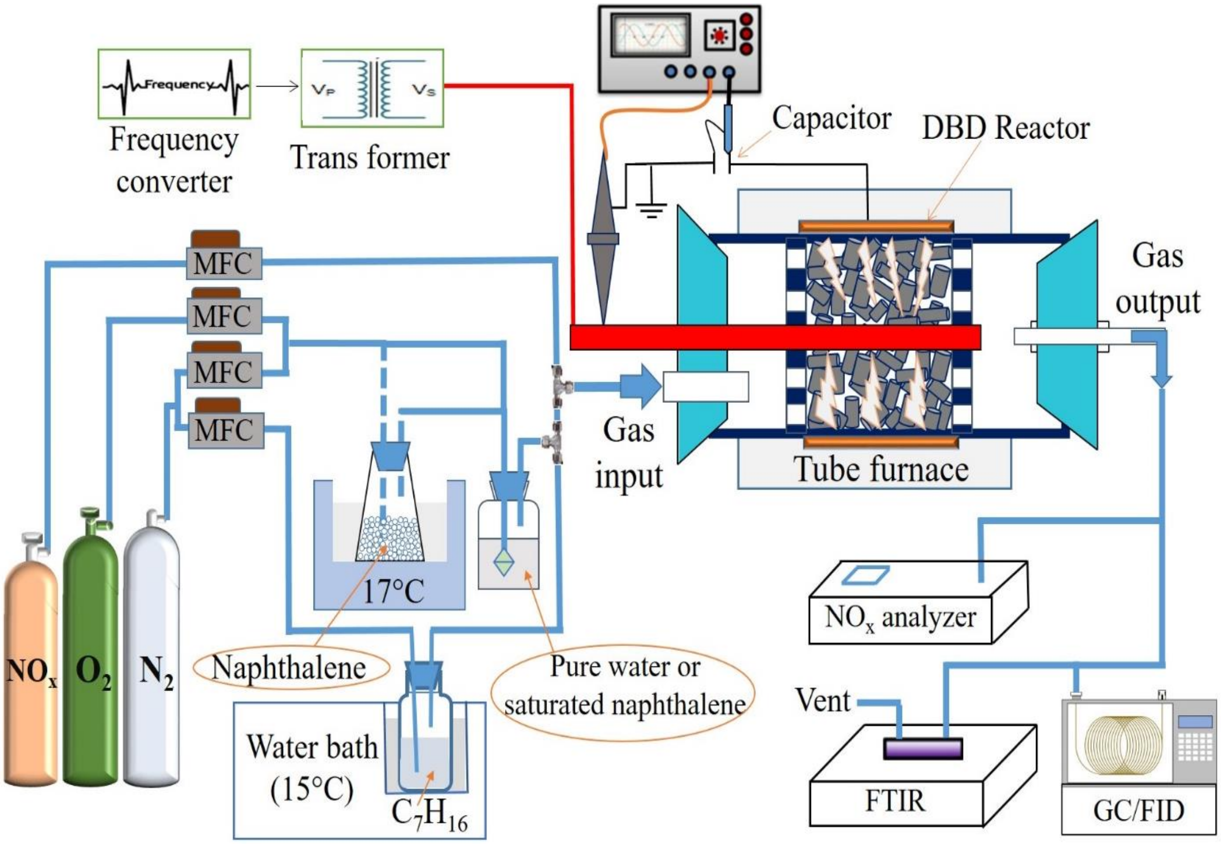

Fig. 2.3. Schematic diagram of the experimental setup for the removal of NO_x and Soot.

of naphthalene. Pure water was used when naphthalene was absent from the feed. The input gases were controlled by mass flow rate controllers (MFC). The feed gas was passed through the reactor placed in an electrical furnace with a proportional-integral-derivative (PID) controller (DTF-50300, Daesung Science Co., Korea) that was controlled in the range of 150-350 ℃.

2.2.2. Experimental setup for styrene removal using DBD plasma catalyst reactor

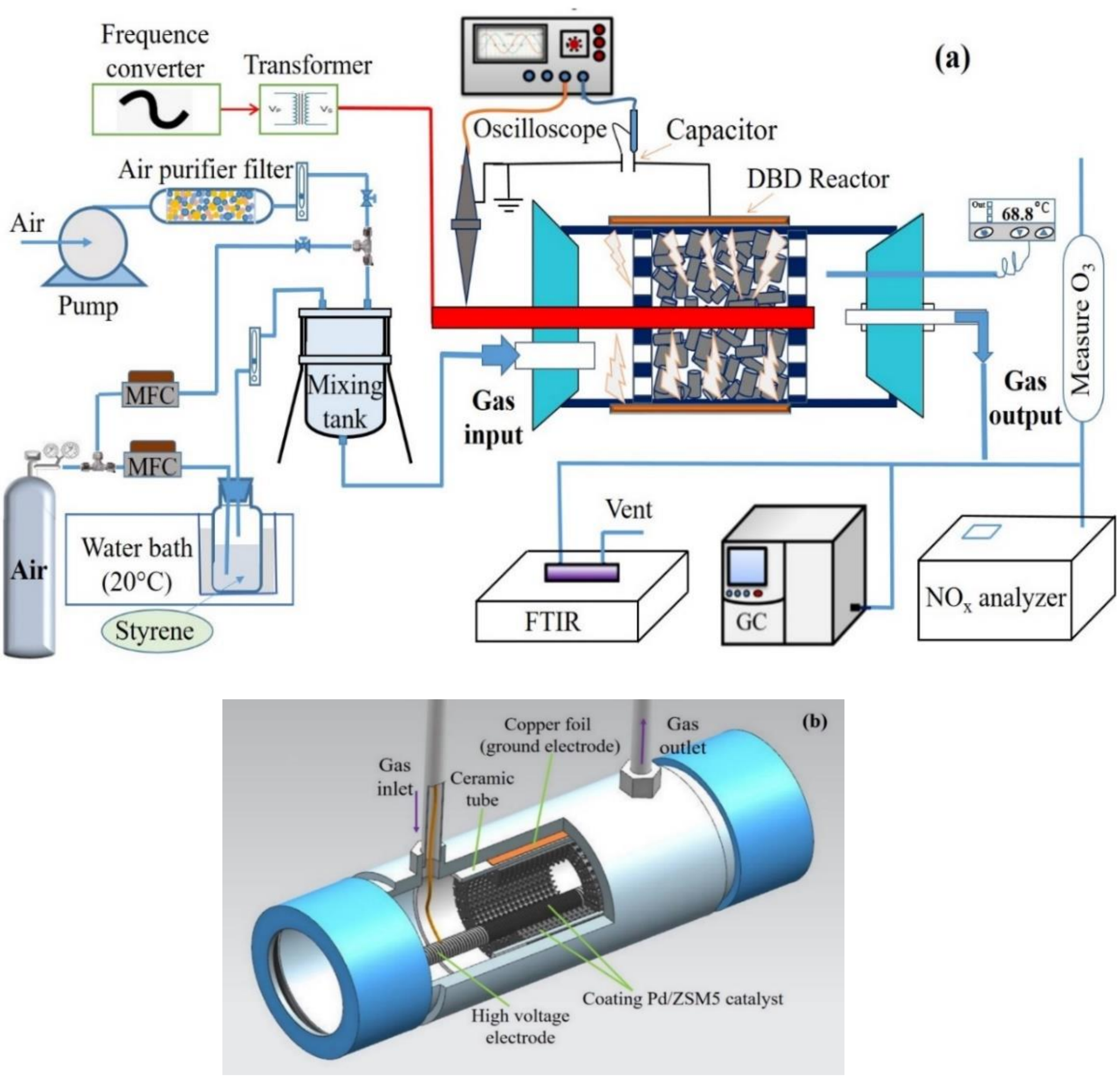

Fig. 2.4. (a) Schematic diagram of the experimental setup, and (b) the cut-away view of the plasma catalytic reactor built in the gas cell.

The removal of styrene by plasma–catalytic reactor was performed in a packed-bed DBD reactor system. Figure 2.4 presents the schematic diagram of the experimental setup. 5 L/min of air containing styrene was fed into the reactor. The concentration of styrene at the reactor inlet was adjusted by bubbling an appropriate amount of air through a flask containing pure styrene liquid kept in a water bath at 20 ℃ and then mixing with the main air stream. The airflow rates were regulated by mass flow controllers (MFCs, Atovac, Korea). All the experiments for the styrene removal were carried out at room temperature and atmospheric pressure

2.2.3. Experimental setup for ethyl acetate removal using corona plasma-honeycomb catalysts system

Figure 2.5(a) shows a schematic diagram of the experimental setup for this study. The reactant gas was prepared by mixing air and EA to obtain the required concentration of EA (30 ppm (v/v). An air pump, of which the flow rate was adjusted by a ball flowmeter (RMA-25-SSV, Dwyer, USA), was used to generate airflow, which was passed through the corona discharge reactor containing the Pd/γ-Al_2O_3-honeycomb (ϕ50 × 50 mm) between the two electrodes. The EA concentration was controlled by a mass flow controller (MFC, Model 1179A, MKS Instruments, Inc., Wilmington, MA, USA), and was obtained by bubbling air through a flask containing pure EA liquid that was kept in a water bath at 5 °C. This gas stream was then diluted with the main air stream. The desired humidity of the flow was achieved by bubbling air through water and was controlled by changing the gas flow through the water at room temperature.

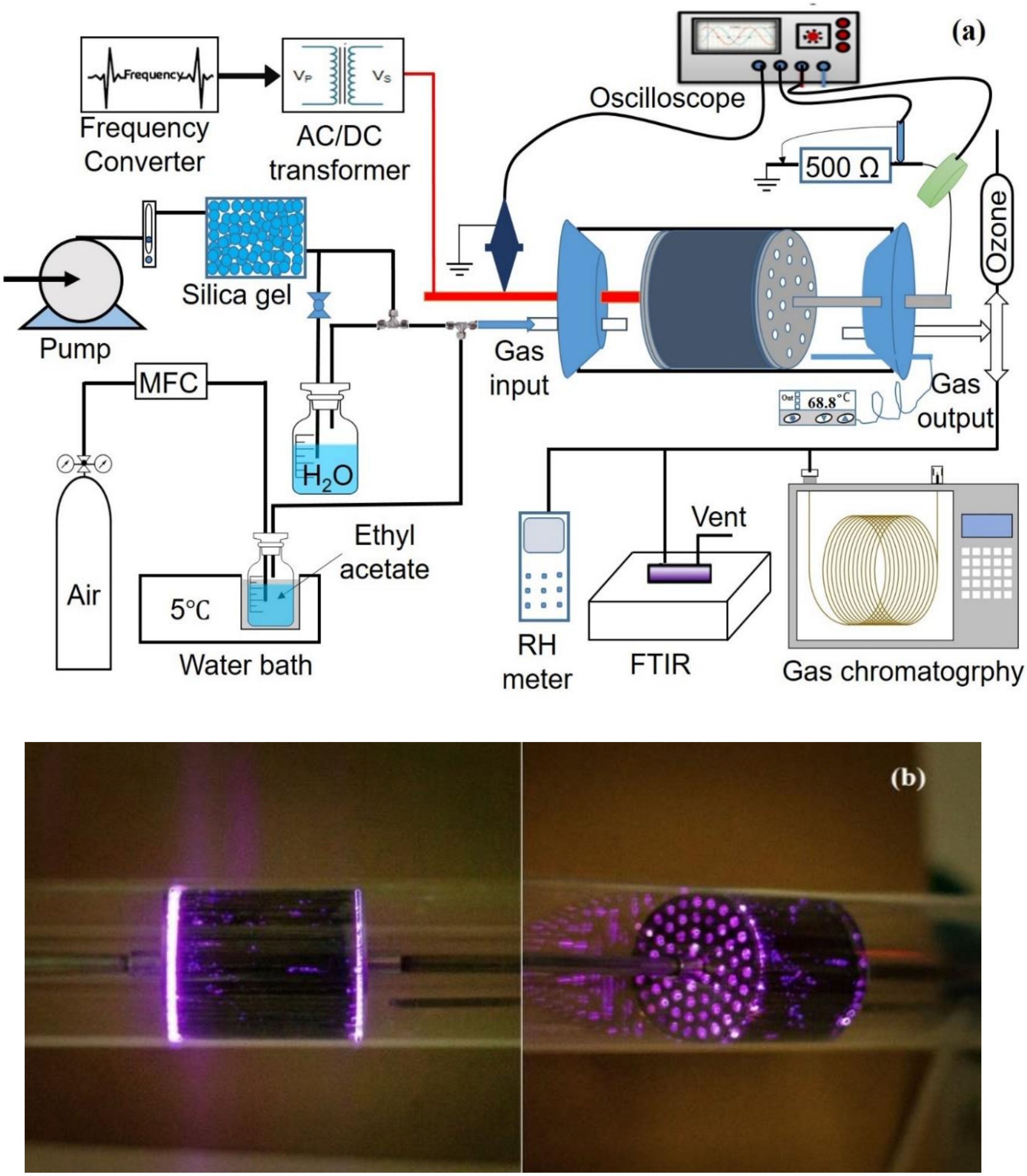

Fig. 2.5. (a) Schematic diagram of the experimental setup, and (b) the photo of corona discharge plasma (applied voltage: 11.2 kV, GHSV: 9000 h^{-1}, water vapor: 3%(v/v)).

2.3. Materials and catalyst preparation

2.3.1. Pellets catalyst

Fig. 2.6. Image of the pellets used in this study.

The pellets catalysts (α-Al_2O_3 and ZSM5 (TOSOH Corp., Japan); pellet size: 3 mm) were prepared by the incipient wetness impregnation method according to the following steps. The pellets were impregnated with an aqueous solution of the nitrate salts contain transition metals ($AgNO_3$ or $Cu(NO_3)_2.3H_2O$, or Pd $(NO_3)_2.2H_2O$). After the impregnation, drying at room temperature for 3 h in air and 110 ◦C overnight was performed. Subsequently, the dried pellets were calcined at 550 ◦C for 6 h. The metal loading on the pellets has been calculated depending on different studies (i.e., $Ag_{0.02}$/α–Al_2O_3, $Ag_{0.02}$/ZSM5, and $Cu_{0.02}$/ZSM5, or $Pd_{0.032}$/ZSM5). The image of the pellets used in this study shows in Fig. 2.6.

2.3.2. Honeycomb catalyst

The cylindrical honeycomb monoliths (50 × ϕ 50 mm) (Fig. 2.7(a)) were obtained by cutting a piece from a commercial cordierite honeycomb (Ceracomb Co., Korea). The honeycomb consists of square cells in a parallel arrangement with a density of 300 cells per square inch (the dimensions of each cell being 1 × 1 mm) along the axial direction and separated by thin walls with a thickness of 0.36 mm. A coating of Pd/γ-Al_2O_3 was deposited on the surface of the honeycomb monolith by the wash-coating method to form the catalytic layer.

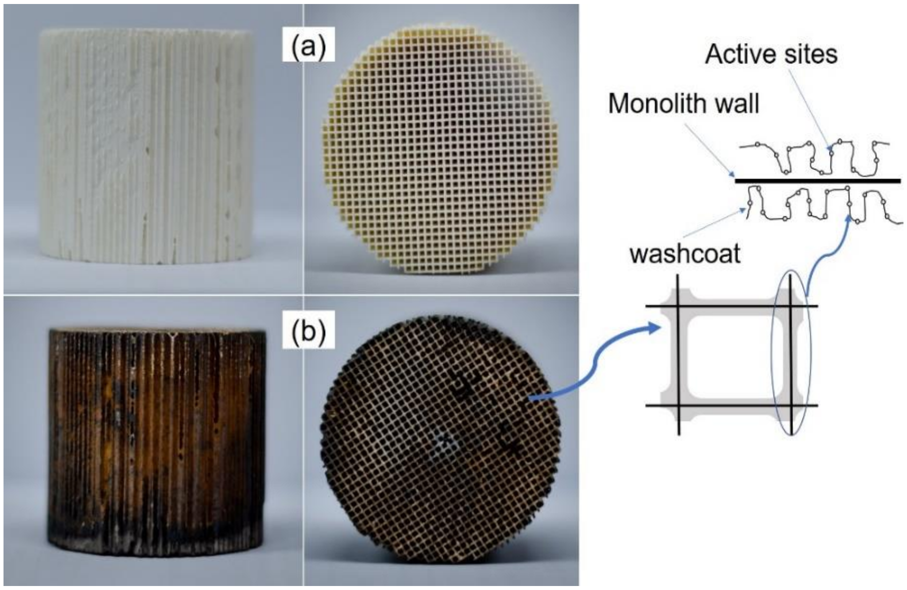

Fig. 2.7. (a) Image of the bare honeycomb monolith, and (b) the honeycomb catalyst after coating used in this study.

First, the honeycomb monolith was washed with ethanol, followed by drying in the oven at 110 °C overnight. Then, γ-Al_2O_3 powder with an average particle size of 45 μm (Sasol Puralox SBa-200) was directly deposited on the monolith by immersing it into an γ-Al_2O_3 slurry (a mixture of γ-Al_2O_3, SiO_2, ethanol, and deionized water in a mass ratio of 1: 0.6: 3.5: 3.5). The slurry was stirred for 1 h at room temperature and used to coat the honeycomb monolith by the impregnation method. The excess gel inside the cells of the monolith substrate was blown off by air. Afterward, the γ-Al_2O_3/honeycomb was dried overnight at 110 °C in an oven. This procedure was repeated three times until the coated layer was uniform.

The loading obtained by wash coating was determined by weighing followed by calcination at 550 °C for 6 h in a tube furnace equipped with a proportional-integral-derivative

(PID) controller (DTF-50300, Daeheung Science Co., Korea). The Pd introduced into the Al_2O_3/honeycomb was prepared by the incipient wetness impregnation method as follows: a certain amount of palladium nitrate $Pd(NO_3)_2.2H_2O$ was dissolved in deionized water and the Al_2O_3/honeycomb monolith was soaked in this solution. Then, the monolith was dried overnight at 110 °C in the oven before it was calcined at 550 °C for 6 h in a tube furnace. This procedure was repeated three times, which allowed the Pd loading to be controlled at 3.5 wt.% ($Pd_{0.035}$/γ-Al_2O_3/honeycomb). The honeycomb monolith structure is coated with Pd/γ-Al_2O_3 as shows in Fig 2.7(b). The supposition for the distributed active sites is illustrated based on literature [70], [92].

2.4. Measurements and analyses methods

The instantaneous waveforms of the voltage applied across the electrodes were recorded with a digital oscilloscope (Tektronix TBS 1064, 60 MHz) using a high voltage probe with a DC attenuation ratio of 1000:1 (Tektronix P6015A). The voltage (V(2)) across the capacitor (1 μF) was measured by a low-voltage probe (P6139B, Tektronix, USA) in the DBD reactor. The power dissipated in the DBD reactor was estimated by the voltage-charge (V-Q) Lissajous figure [93], [94], where the charge Q was measured from the voltage across a 1.0 μF ceramic capacitor connected to the ground electrode in series. A current transformer (Model 2100, Pearson, USA) was used to measure the current of the DBD plasma reactor and the AC corona discharge. The DC discharge current was measured by connecting a 500 Ω resistor (r) to the plasma reactor in series. A 10:1 voltage probe (Tektronix P6139B) was used to measure the voltage across the non-inductive resistor. Optical emission spectroscopy (OES, Maya 2000Pro, Ocean Optics) was used to analyze the plasma chemistry by positioning the spectrometer about 30 mm away from the plasma zone of the reactor.

The concentrations of NO_x were measured by a gas analyzer (rbr-ecom-MK 6000, Germany).

The decomposition rate of n-heptane, naphthalene, styrene, and ethyl-acetate was derived by analyzing the composition of the gas reaching the outlet of the reactor using gas chromatography (GC, DS6200, DS Science Inc., Korea, and DS-624, DS Science Inc., Seoul, Korea) and a flame ionization detector (FID)) with a flame ionization detector (FID).

A Fourier-transform infrared (FTIR) spectrometer (FTIR-7600, Lambda Scientific, Australia) was used to measure the concentrations of CO_2 and other byproducts formed from the NO_x and VOC oxidation. A specially designed plasma-catalytic reactor built in an infrared gas cell was used to record the FTIR spectra, which is illustrated in Fig. 2.4(b). The gas mixture that was employed to analyze the by-products was composed of a high concentration of VOC (i.e., 500 ppm styrene, and 300 ppm EA) diluted by air. The reason for increasing the concentration is to facilitate the detection of reactive products.

The oil-like byproduct collected from the reactor was dissolved in acetone and then analyzed by the FTIR and a gas chromatograph-mass spectrometer (GC–MS, QP2010Plus, Shimadzu, Japan).

The concentration of ozone was monitored by a chemical detector (No.18 M, Ozone, Gastec Corp., Japan). The water vapor content was monitored using an indoor air quality meter (Model 8762, TSI Inc., USA). The temperature of the outlet gas was measured at intervals of oxidation time using a thermocouple placed downstream 20 mm away from the ground electrode, as depicted in Fig. 2.4(a).

The surface morphology was observed and the semi-quantitative compositional analyses of the honeycomb catalyst were carried out by using scanning electron microscopy (SEM)

(MIRA3, TESCAN instrument, Czech Republic). The X-ray diffraction (XRD) patterns were recorded on a PANalytical EMPYREAN instrument using monochromatic Cu-Kα radiation. The scan ranged from 5 to 90° (2θ) at a scanning rate of 2° (2θ)/min.

2.5. Calculation methods

The average discharge power (P) delivered to the reactor was calculated by equation (1). The specific input energy (SIE) was defined by the ratio of the power to the gas flow rate at room temperature and atmospheric pressure as in equation (2) [29], [43], [44].

$$\text{Discharge power, } P(W) = \frac{1}{T}\int_0^T V(t) \times I(t)\ dt = \int_{t_0-\frac{T}{2}}^{t_0+\frac{T}{2}} V_{DBD}(t).dq(t)$$

$$= \quad f.C.\sum_{j=1}^{n}\left(\frac{V^{(1)}{}_{j+1}-V^{(2)}{}_{j+1}+V^{(1)}{}_{j}-V^{(2)}{}_{j}}{2}\right)\left(V^{(2)}{}_{j+1}V^{(2)}{}_{j}\right) \qquad (1)$$

$$\text{Specific input energy, } SIE(J/L) = \frac{P(W)}{Q\left(\frac{L}{min}\right)}\,60\left(\frac{s}{min}\right) \qquad (2)$$

Here, $V^{(1)}$, and V(t) is the applied high voltage, $V^{(2)}$ is the voltage across the 1-μF capacitor, current (I(t) (A), P is the discharge power (W), Q is the flow rate, and n denotes the number of data points recorded by the oscilloscope. For this work, n was 2,500.

The root mean square of the current (I_{RMS}) was determined by Eq. 3.

$$\text{Current, } I_{RMS}\ (mA) = \sqrt{\sum_{i=1}^{n}\frac{(I_i)^2}{n}} \qquad (3)$$

where I_i is instantaneous current values

The energy efficiency (EE) was calculated using Eq. (4).

$$\text{Energy efficiency, EE } (g/kWh) = \frac{\text{weigh of } C_4H_8O_2 \text{ conversion (g)}}{\text{Energy consumption (kWh)}} = \frac{3.6 \times 88.11 \times \eta \times C_{in}}{24.45 \times SIE} \qquad (4)$$

Here C_{in} (ppm) is the inlet concentration of ethyl-acetate ($C_4H_8O_2$); 1mol of ethyl-acetate weights 88.11 g; 1 mol of gas under atmospheric conditions and experimental operating temperature (298 K) has a volume of 24.45 L; 3.6 is a factor to obtain g/kWh corresponding concentration unit as ppm.

The efficiency of NO_x reduction (X (%)) was calculated by [83], [95].

$$\text{NO}_\text{x}\text{ conversion efficiency, X (\%)} = \frac{C_{NO_x}^{in} - C_{NO_x}^{out}}{C_{NO_x}^{in}} \times 100\% \qquad (5)$$

where $C_{NO_x}^{in}$ is the concentration of NO_x at the inlet, and $C_{NO_x}^{out}$ is the concentration of the NO_x at the outlet of the reactor.

The conversion efficiency of n-heptane, styrene, and ethyl-acetate was determined from the concentrations of the feed and effluent as follows [29], [43]:

$$\text{Conversion efficiency, H (\%)} = \frac{C_{C_xH_yO_z}^{In} - C_{C_xH_yO_z}^{Out}}{C_{C_xH_yO_z}^{In}} \times 100\% \qquad (6)$$

where $C_{C_xH_yO_z}^{In}$ and $C_{C_xH_yO_z}^{Out}$ are the concentrations of n-heptane, styrene, and ethyl-acetate at the inlet and the outlet of the reactor, respectively.

The selectivity towards CO_2 (S_{CO_2}) was defined as follows:

$$\text{CO}_2\text{ selectivity, } S_{CO_2} = \frac{C_{CO_2}^{Outlet}}{m \times (C_{C_xH_yO_z}^{In} - C_{C_xH_yO_z}^{Out})} \times 100\% \qquad (7)$$

CHAPTER 3

LOW-TEMPERATURE HC-SCR OF NO_X AND SOOT REMOVAL USING PLASMA COUPLED WITH CATALYSTS

The experimental setup and catalyst preparation for this work was presented in sections 2.2.1 and 2.3.1 (chapter. 2).

3.1. Evaluation of low-temperature NO_x removal over Ag/ZSM5 and Cu/ZSM5 catalysts coupled with plasma

Redrafted from:

V. T. Nguyen et al., IEEE Trans. PLASMA Sci., vol. 48, no. 7, pp. 2448–2456, 2020

3.1.1. Characterizations of the catalysts

1. SEM

Scanning electron microscopy was carried out on a MIRA3 TESCAN instrument. The SEM images and EDS spectra of the samples are presented in Fig. 3.1 where it can be seen that the Ag^+ and Cu^{2+} particles are well dispersed. The presence of Ag and Cu crystals on the surface of ZSM5 can be considerably enhanced the catalytic activity in comparison with conventional zeolites.

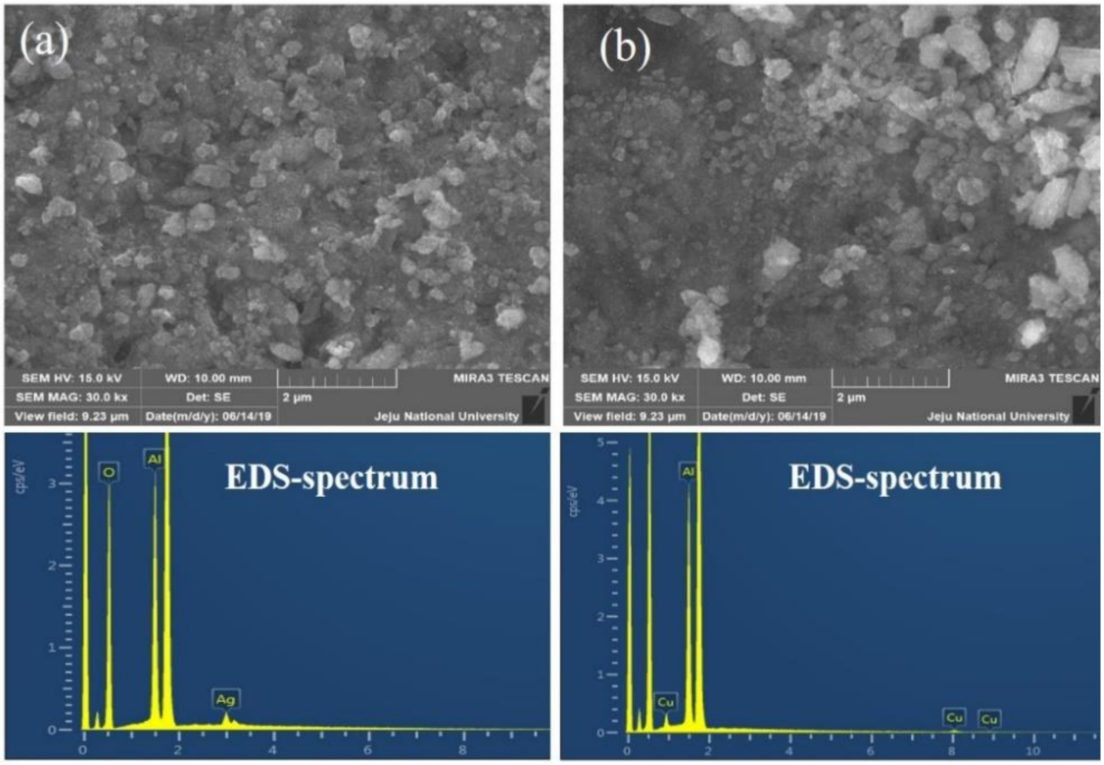

Fig. 3.1. SEM images of the samples (a) 2 wt.% Ag/ZSM5, (b) 2 wt.% Cu/ZSM5 and the corresponding EDS spectra.

2. XRD

The structure and crystallinity of the catalysts were examined by X-ray diffraction (XRD). The XRD patterns of the catalysts were analyzed by a PANalytical EMPYREAN instrument using monochromatic Cu-Kα radiation. The XRD data were collected from 5 to 90° (2θ) at a scanning rate of 2° (2θ)/min. Figure 3.2 shows the XRD results for the bare ZSM5, Ag/ZSM5, and Cu/ZSM5. These results indicated the absence of peaks associated with the crystalline phase of Cu^{2+} and Ag^{+}, suggesting that the Cu^{2+} and Ag^{+} deposited on the surface of the ZSM5 zeolite were well dispersed. Furthermore, the characteristic reflections of Cu^{2+} and Ag^{+} were not discernible because of their low concentration.

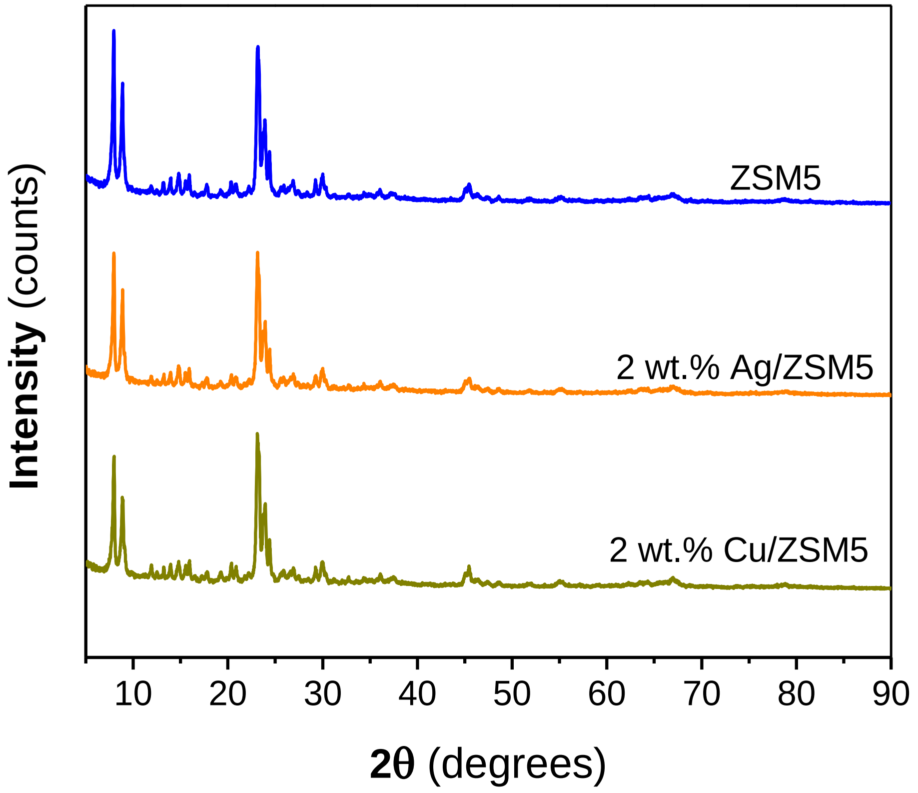

Fig. 3.2. XRD patterns of the ZSM5, Ag/ZSM5, and Cu/ZSM5.

3. Catalyst absorption capacity

The adsorption capacities of the catalysts for n-heptane were evaluated in a fixed bed reactor at 100 ℃. The inlet mixture contained 85 ppm n-heptane, 10% oxygen, and 3.7% H_2O. As shown in Fig. 3.3, most of the n-heptane in the feed gas was adsorbed on the catalyst in the first 2 min, which was followed by a sharp increase in the n-heptane concentration during the next 10 min, indicating that the catalyst was saturated with the hydrocarbon. The adsorption capacity of the bare ZSM5 was lower than those of the metal-loaded ZSM5. This result is consistent with the previous study [96]. In addition, the result also indicated that the adsorption capacity of the Ag/ZSM5 catalyst was higher than that of the Cu/ZSM5 catalyst, which also agrees with the literature [97].

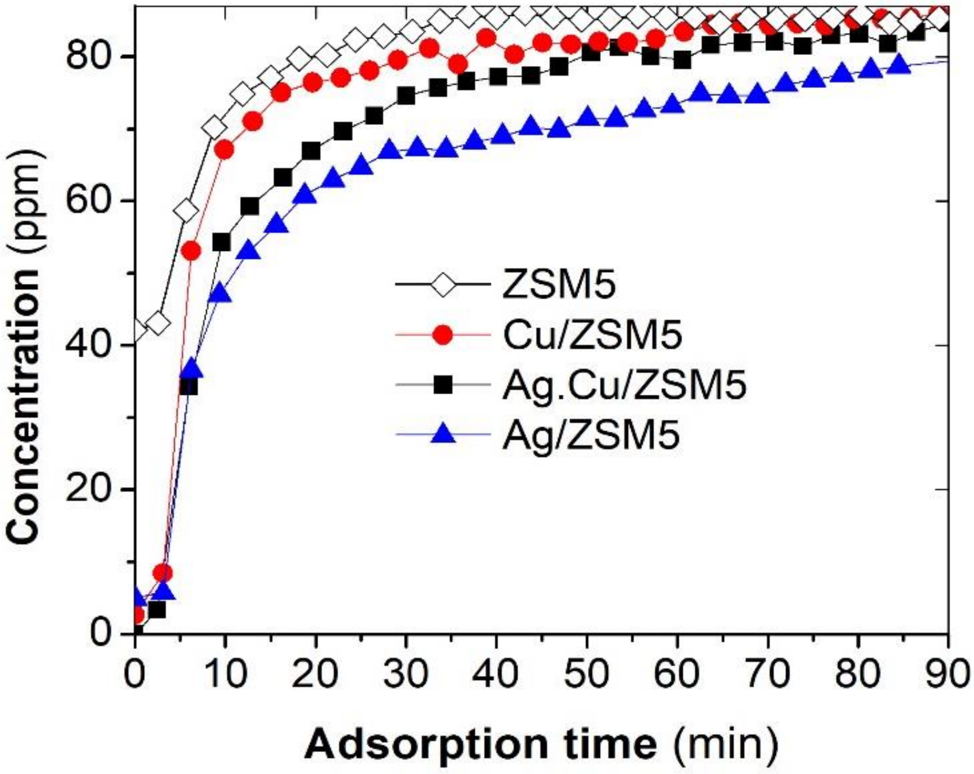

Fig. 3.3. The adsorption capacity of n-heptane by the catalysts at 100 ℃ (total flow is 2 L/min, which includes 85 ppm n-heptane, 3.7% H_2O, 10% O_2 with the balance being N_2, 1g catalysts).

The adsorption capability is closely related to the pore structure of the catalyst that can contain reactants, active species, and reaction products. The diffusion of NO, NO_2, hydrocarbon, and plasma-generated active species into zeolite micro-pores causes heterogeneous reactions for NO_x removal. The oxidation of NO to NO_2 by plasma occurs mainly in the gas phase. Thus, it can be said that both homogeneous and heterogeneous reactions take place in the plasma-catalytic system. The pore size calculation of ZSM5 was carried out in previous studies that reported an average pore size of approximately 10 nm determined from transmission electron microscopy measurements [98], [99].

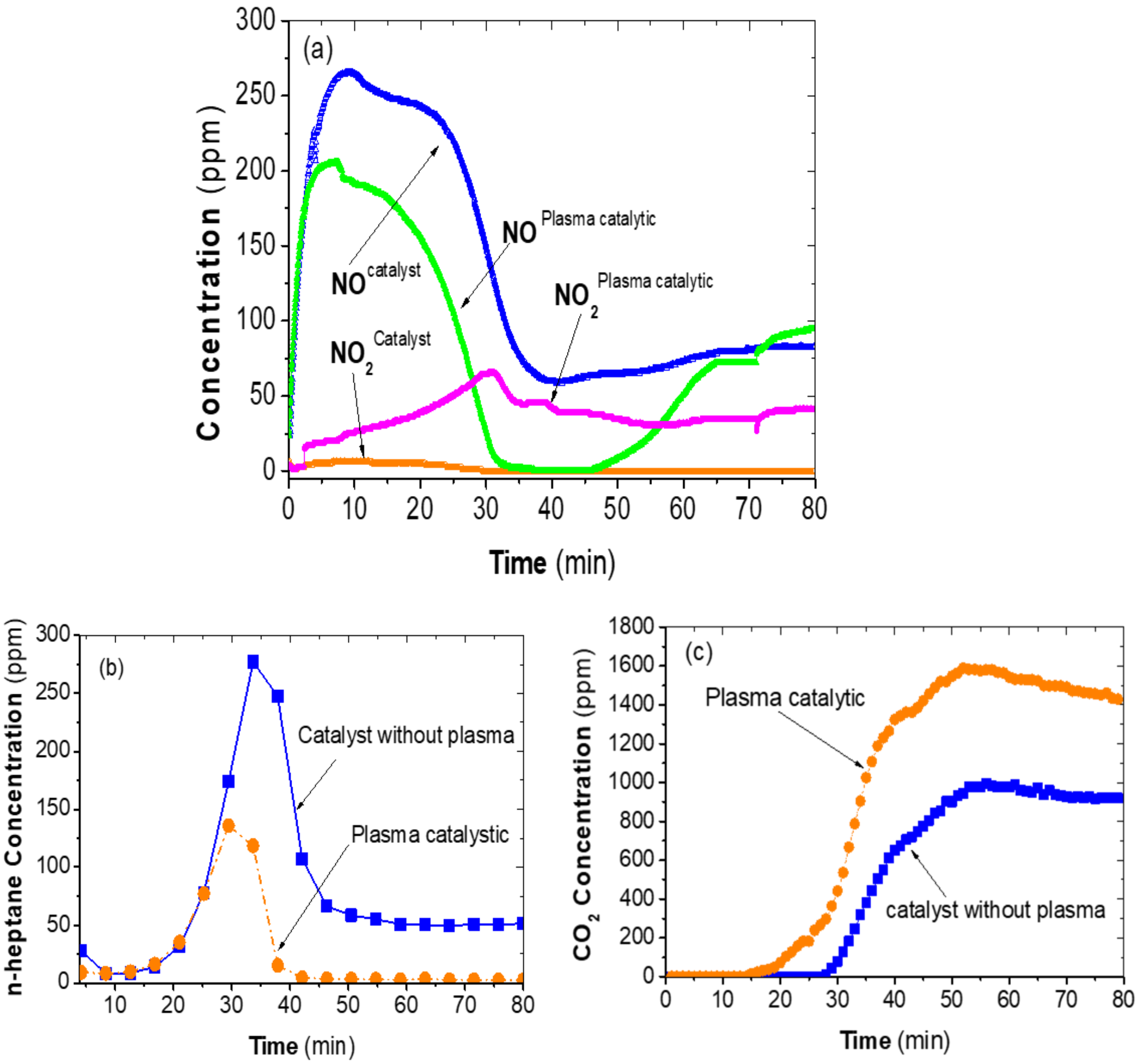

Fig. 3.4. The evolution of gas composition obtained with and without plasma: (a) NO and NO_2 concentration, (b) n-heptane concentration, and (c) CO_2 concentration (the temperature was increased from 150 to 350 °C within 50 minutes and maintained at 350 °C, Ag/ZSM5 catalyst, applied voltage 9 kV).

The results in Fig. 3.4(a) show that a considerable amount of NO_2 and a small part of NO were adsorbed on the Ag/ZSM5 catalyst in the early stage. This result is consistent with the previous study [100]. The presence of O_2 in the gas stream promoted the adsorption under plasma because NO was easily oxidized to NO_2. As shown in Fig. 3.4(b) and (c), the concentration of n-heptane in the output gas stream was very low, and CO_2 was not observed in the early stage even in the presence of plasma. This result clearly shows that both n-heptane, CO_2, and NO_2 were efficiently adsorbed by the catalyst at low temperatures. As the temperature increases, adsorption generally decreases but catalytic activity increases. The reason that the NO concentration continued to decrease after the initial stage can be interpreted by the increase in catalytic activity due to the increased temperature.

3.1.2. NO_x removal over Ag/ZSM5 and Cu/ZSM5 coupled with plasma

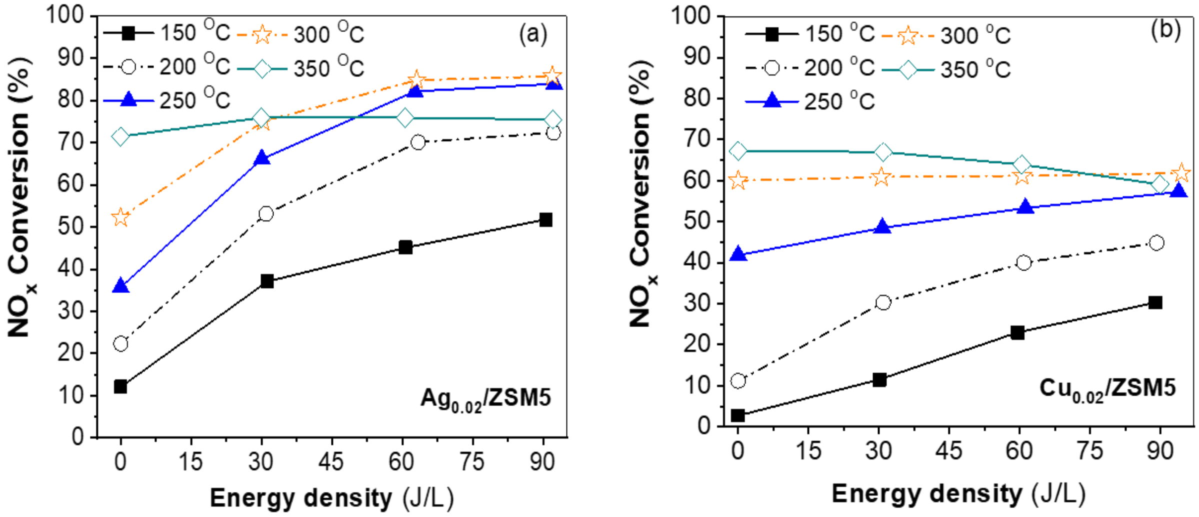

Fig. 3.5. Dependence of the efficiency of NO_x removal on SIE and the operating temperature over (a) Ag/ZSM and (b) Cu/ZSM catalysts coupled with plasma (total flow is 2 L/min, which includes 300 ppm NO_x, 265 ppm n-heptane, 3.7% H_2O, 10% O_2 with the balance being N_2).

As mentioned above, although the Ag/ZSM5 catalyst capacity than Cu/ZSM5, its efficiency in terms of NO_x reduction at low temperatures was still low. In the absence of plasma, the catalyst becomes effective at high temperatures. So as to achieve a high NO_x removal rate at low temperatures below 350 °C, the catalyst was combined with plasma. Firstly, the efficiencies of the Ag/ZSM5 and Cu/ZSM5 catalysts for NO_x reduction were evaluated in the range of 150–350 °C. The results in Fig. 3.5 exhibit that the plasma-catalyst can enhance the efficiency of NO_x reduction at low operating temperatures. The oxygen in the gas stream had a positive effect on the removal of NO_x even at low temperatures under the influence of plasma [101], [102]. The presence of O_2 in the flue gas may be essential because of the formation of O_3 and O by the plasma, which can oxidize NO to NO_2. Note that NO_2 is more easily adsorbed on the active sites of the catalyst than NO [100]. The dielectric barrier discharge can provide reactive species such as electrons, excited species, and radicals (O_3, OH, and O) at low temperatures.

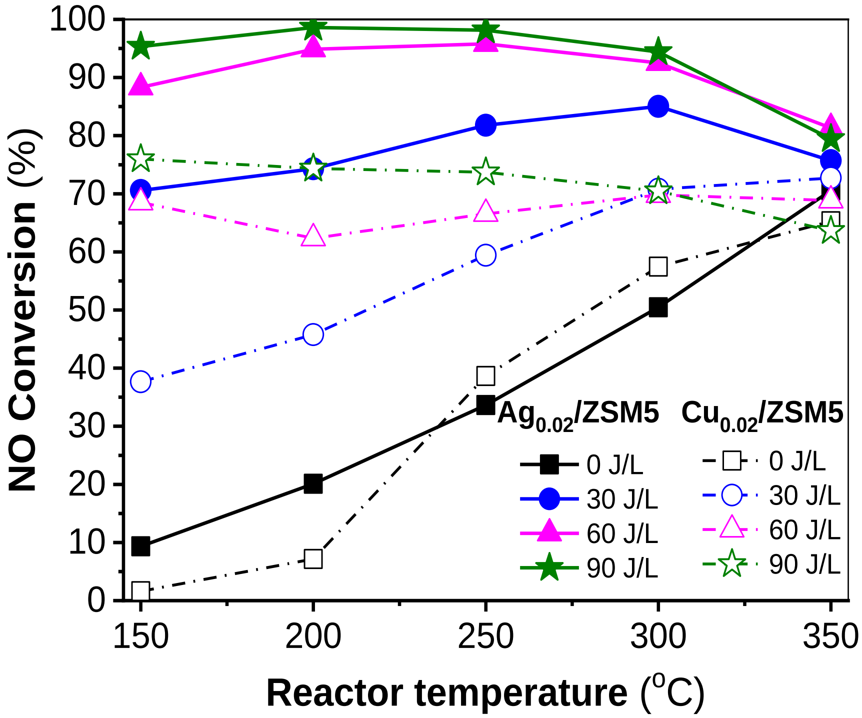

Fig. 3.6. Comparison of NO conversion efficiency over Ag/ZSM5 and Cu/ZSM5 catalysts coupled with plasma.

In addition, the use of electrical discharge can enhance the activation of the catalyst surface to increase catalytic NO_x conversion. The increase in the applied voltage had a positive effect on NO_x removal at low operating temperatures. The efficiency of NO_x conversion over the Ag/ZSM5 catalyst increased from approximately 20% to over 70% according to the increase of SIE from 0 to 90 J/L at 200 ℃, whereas 10% to about 40% over the Cu/ZSM5. In the case of DBD, the voltage in the discharge gap remains generally independent from the applied voltage when the voltage change remains slow [103]–[105]. The increase of the applied voltage increased the number of micro-discharges, in turn increasing the discharge power and current [106]–[108]. As a result, the number of energetic electrons, radicals, and ions in the plasma region increased, which accelerated the NO_x reduction reactions. Figure 3.6 presents the conversion of NO as a function of the operating temperature. NO conversion by the Ag/ZSM5 catalyst was much higher than that of the Cu/ZSM5. However, a significant decrease in NO_x removal rate was observed at 350 ℃. This result can be explained as follows. At a high temperature of 350 ℃, the combination of plasma is not needed because the catalytic activity itself is good. The presence of plasma can have a negative effect on the NO_x removal rate because some radicals such as O generated in the plasma region can reduce NO_2 back to NO [83], [108], [109]. As well, the reaction between O_2 and N_2 to generate a considerable amount of NO_x also decreases net NO_x removal efficiency [110]. For the above reasons, it is necessary to turn off the plasma at high temperatures. In summary, the NO_x removal rate can be above 80% in Ag/ZSM5 catalyst coupled with plasma in the low operating temperature range below 350 ℃.

In the presence of plasma, the n-heptane decomposition was also significantly enhanced. As seen in Fig. 3.4(b) and Fig. 3.7, the decomposition of n-heptane increased significantly with increasing the operating temperature and energy density. Moreover, the decomposition of n-heptane and the concentration of CO_2 when using the plasma-catalyst were higher than those in the catalyst alone. For example, the consumption of n-heptane at 250 ℃ reached approximately 50% with the catalyst alone, whereas it exceeded 80% with the plasma-catalyst under the same condition, which resulted from the oxidation process enhanced by the plasma.

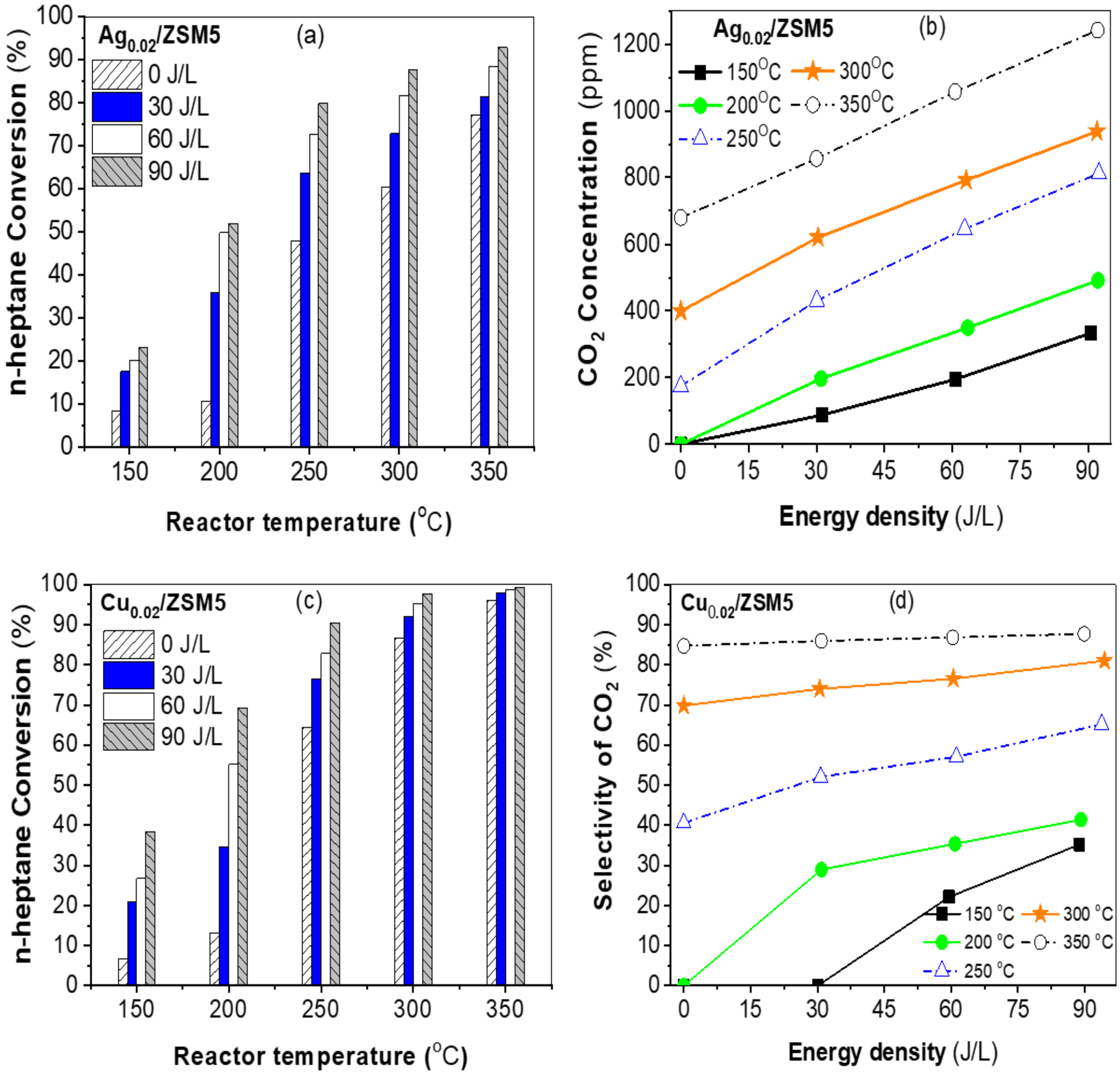

Fig. 3.7. Effect of SIE and the operating temperature on the decomposition of n-heptane, the concentration of CO_2, and the selectivity of CO_2 based on Ag/ZSM5 and Cu/ZSM5 catalysts coupled with plasma (total flow is 2 L/min, which includes 300 ppm NO_x, 265 ppm n-heptane, 3.7% H_2O, 10% O_2 with the balance being N_2).

3.1.3. Effect of H_2O on NO_x reduction and storage capacity

In reality, exhaust gas contains 5–10 % water vapor by the combustion process of fossil fuel. The presence of H_2O in the gas stream considerably affects the efficiency of NO_x reduction by the catalyst in that it reduces the NO_x adsorption capacity on the catalyst surface [96], [111]. To evaluate the effect of H_2O on NO_x reduction, a comparison was made between with and without H_2O in the gas stream.

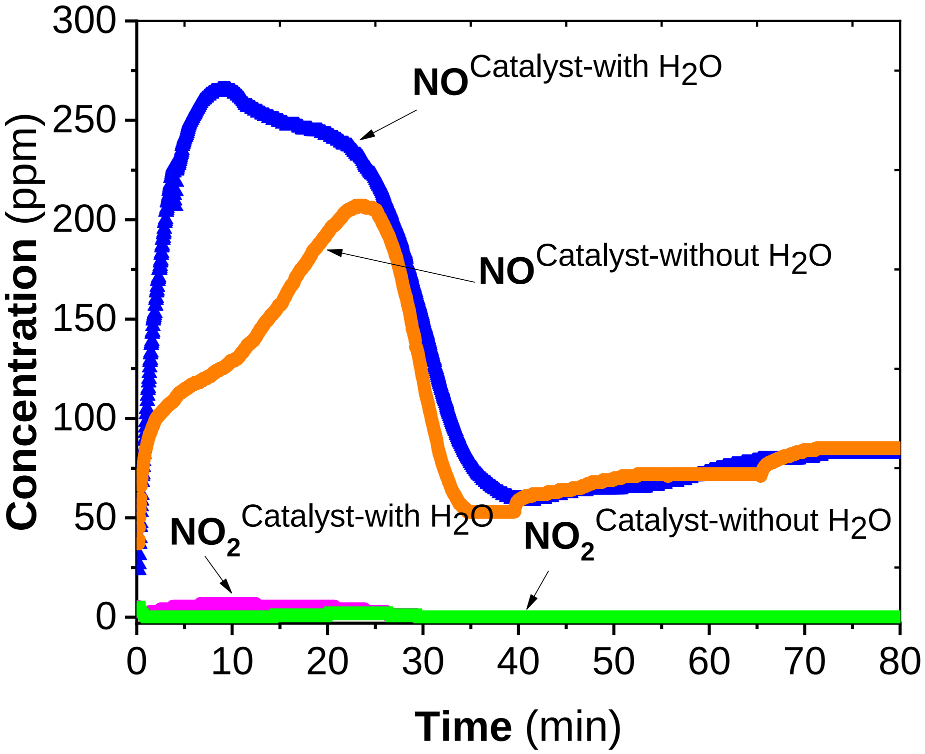

Fig. 3.8. Effect of H_2O on NO_x reduction efficiency over Ag/ZSM5 catalyst (operating temperature was increased from 150 to 350 ℃ within 40 minutes and maintained at 350 ℃ based on Ag/ZSM5 catalyst with 3.7% H_2O and without H_2O, total flow 2 L/min, 300 ppm NO_x, 265 ppm n-heptane and 20g catalyst).

The results in Fig. 3.8 revealed that most of NO_2 and a fraction of NO were adsorbed on the catalyst surface at low temperatures and NO_x reduction took place at high temperatures. Humidity significantly reduced the adsorption performance of NO rather than NO_2 at low temperatures. However, the effect of moisture was negligible at high temperatures where good catalytic activity was exhibited. Zeolites with a high specific surface area can absorb a large amount of H_2O. The competitive adsorption as a result of H_2O decreases the adsorption capability of NO_x [96], [100], [111]. Furthermore, the adsorbed water could increase the oxidation process of C_7H_{16} in the DBD plasma reactor, resulting in the shortage of reducing agents and thereby dropping off the NO_x removal efficiency. From another point of view, H_2O can also have a positive effect on the overall reaction in catalyst coupled with plasma [112]. H_2O can be activated in the plasma environment, generating H and OH radicals as a result of electron collisions with water molecules. The OH radicals can promote the conversion of NO into NO_2 and NO_2 into HNO_3 [113]. On the other hand, the adsorbed H_2O had an undesirable effect on the discharge power. The presence of water molecules can reduce energy density by consuming high-energy electrons, resulting in a decrease in the NO_x removal rate.

3.1.4. Role of HC-SCR in the efficiency of NO_x reduction

The HC-SCR in the gas stream plays an important role in the reduction of NO_x over the plasma catalyst. The positive effect of hydrocarbon on NO conversion in presence of plasma can be explained by the suppression of back-reaction of NO_2 to NO [108], [113]–[115]. To elucidate the role of n-heptane in the NO_x reduction, the reaction temperature was varied from 150 to 350 ℃ within 40 min and then maintain at 350 ℃ for both with and without 265 ppm n-heptane. The Ag/ZSM5 catalyst coupled with plasma was used. The temporal variations of NO and NO_2 that were obtained by increasing the temperature from 150 to 350 ℃ within 40 min were plotted in Fig 3.4(a) and Fig. 3.9. An interesting observation is that the plasma catalyst did

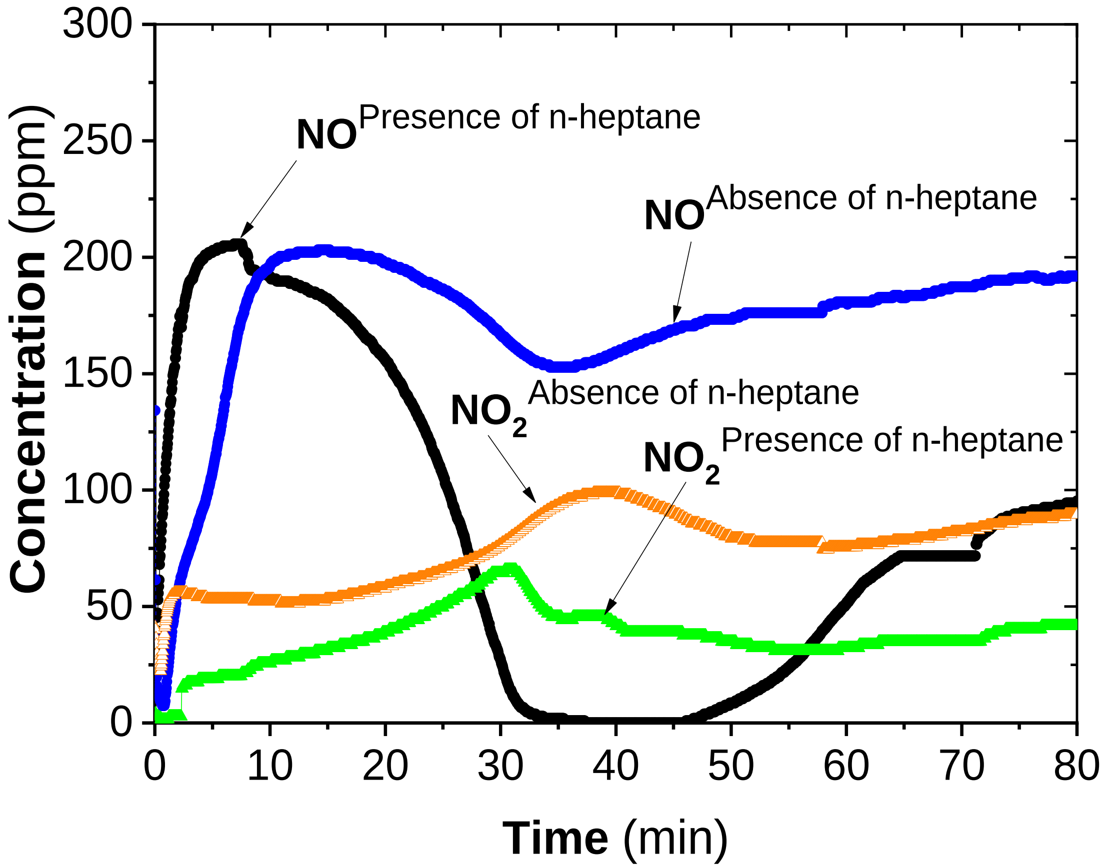

Fig. 3.9. Role of HC-SCR on NO_x reduction efficiency over Ag/ZSM5 catalyst coupled with plasma (operating temperature was increased from 150 to 350 °C within 40 minutes and maintained at 350 °C based on plasma catalyst with and without n-heptane, applied voltage 9 kV).

not show significant activity for the direct oxidation of NO in the absence of the reducing agent, whereas the presence of n-heptane in the gas stream as a reducing agent improved the conversion of NO [113]. The result typically indicated that the conversion of NO was approximately 100% in the range of 200–300 °C. This result suggests that both O atom and HO_2 radicals participated in the oxidation of NO to NO_2. The HO_2, O_3, O, OH, and RO radicals (R is a hydrocarbon radical) are known to be the products of plasma chemistry [108], [115], [116]. In the absence of n-heptane, the reduction of NO_x at low operating temperatures is difficult. In fact, the main function of plasma is to promote the oxidation reaction of NO to NO_2. Thus, the efficiency of NO_x reduction is very poor in this case even when applying plasma, as shown in Fig. 3.9. As mentioned above, the hydrocarbon suppresses the reaction of NO_2 back to NO when plasma is used [113], [115]. A noticeable phenomenon is that the shapes of the NO conversion curves are significantly changed at the operating temperature of 350 ℃. The conversion of NO was observed to decrease when plasma was applied at an operating temperature exceeding 350 ℃. This phenomenon reaffirmed the adverse effects of plasma on the efficiency of NO_x removal at high operating temperatures.

3.1.5. Effect of temperature on discharge

The effect of the operating temperature on the discharge power was investigated by varying the temperature from 150 to 350 ℃ and the applied voltage from 8 kV to 14 kV. Figure 3.10 presents the discharge power of DBD plasma as a function of the applied voltage and the operating temperature. The results revealed that the temperature of the gas significantly affected the discharge power. Increasing the operation temperature increased the amount of charge, which led to an increase in the area of the Lissajous voltage-charge figure. Increasing the voltage significantly increased discharge power, too. According to the Lissajous figure method, the discharge power can be estimated by the area of the voltage-charge figure [93]. The resistance and capacitance depend on the temperature. Furthermore, the current (the root of mean square or I_{rms}) also depended on the operating temperature and the applied voltage as shown in Fig. 3.10(b). The results showed that the current increased as the temperature increased at the same applied voltage. The increase in I_{rms} suggests that more micro-discharges occurred in the plasma

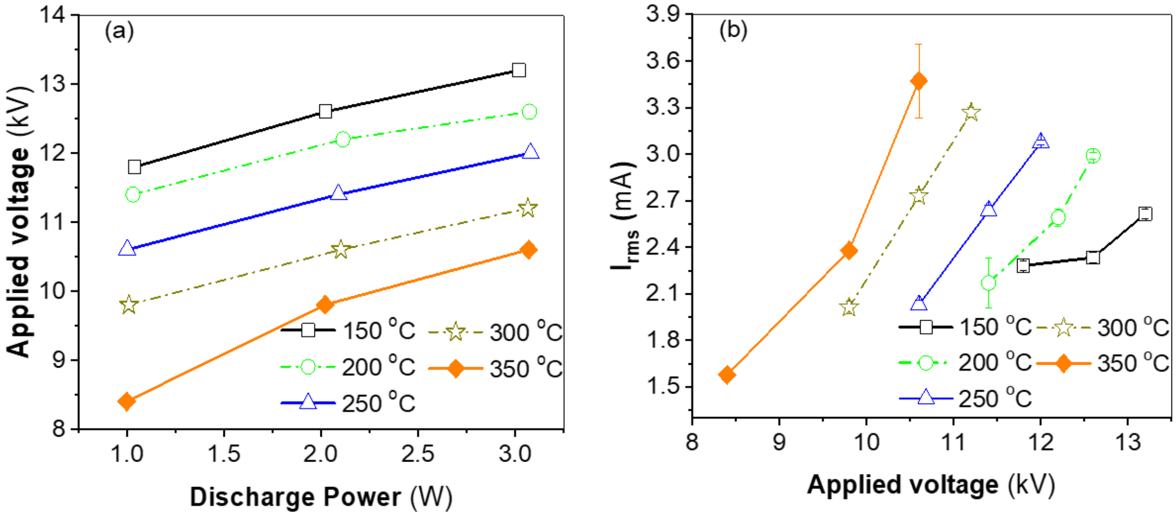

Fig. 3.10. Discharge power as a function of the operation temperature and applied voltage.

zone [106]–[108], intensifying the discharge and generating more reactive species such as electrons, excited species, and radicals. Interestingly, the magnitude of the voltage at high operating temperature tended to decrease, as revealed in Fig. 3.10. The value of the applied voltage depends on the operating temperature. At 30 J/L of SIE, the applied voltage was approximately 12 kV at 150 ℃ while it was only 8.3 kV in the case of 350 ℃. At high gas temperature, the required potential for gas ionization is lowered, which results in the change of discharge power, voltage, and current. Indeed, the efficiency of NO_x reduction and the consumption of n-heptane depended on the discharge power. From the energy use point of view, the optimal condition for a high NO_x removal rate at low temperatures should be the condition exhibiting minimal energy consumption. At 150 ℃, the energy density was around 90 J/L with $Ag_{0.02}$/ZSM5 for achieving NO conversion over 95%, but, at 250 ℃, the same NO conversion can be achieved at the energy density of about 60 J/L. Therefore, appropriate energy density should be determined by considering both desired NO_x removal efficiency and gas temperature.

3.2. Plasma-assisted selective catalytic reduction for low-temperature removal of NO_x and Soot simulant

Redrafted from:

V. T. Nguyen et al., Catalysts, vol. 9, no. 10, pp. 855–869, 2019.

3.2.1. Effects of plasma input parameters on discharge power

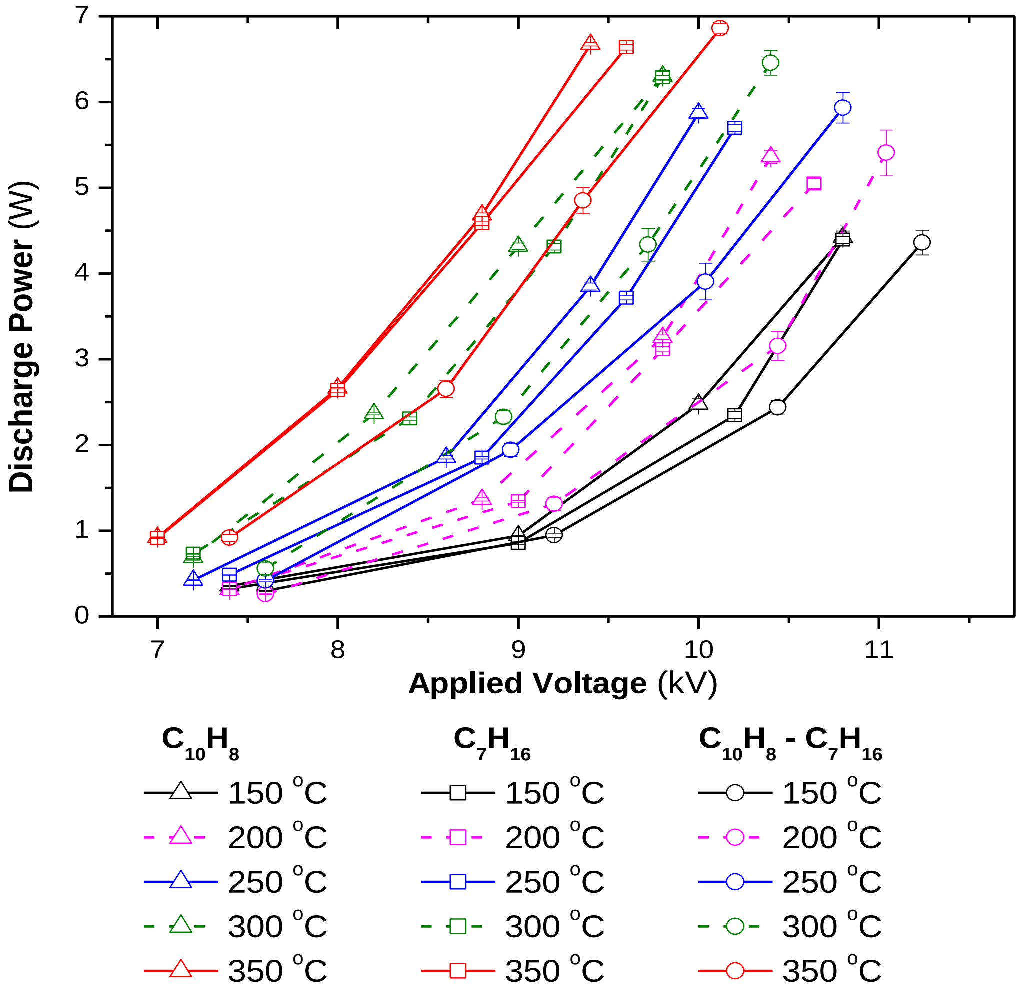

Fig. 3.11. Discharge power as a function of temperature and applied voltage for different gas compositions (total flow rate fixed at 2 L/min including 3.7% H_2O, 10%O_2, reducing agents: 48 ppm $C_{10}H_8$, 265 ppm C_7H_{16}, N_2 as balance; acquire mode of the oscilloscope: the average of 128 waveforms).

Figure 3.11 indicates an increase in discharge power as a function of the temperature and applied voltage. According to the Lissajous figure method [93], the deposition of the input energy of the DBD system depends on the applied voltage and electrical charge of DBD. Consequently, high-amplitude voltage led to considerable discharge power. The discharge power also increased at high temperatures, which can be explained by an increase in the DBD charge. Indeed, the discharge power can be estimated by the area of voltage-charge figures. When the amplitude of the voltage was maintained while increasing the operating temperature, the amount of charge increased and, in turn, the area of the voltage-charge figure, as well as the discharge power, became large [95]. This figure also demonstrates that the presence of n-heptane and naphthalene at the level of a few hundred ppm could change the discharge power significantly. This phenomenon was also observed when the CHF_3 concentration was changed to a few thousand ppm in the feed in the DBD discharge [117]. Equation (8), which is adapted from published work [118], can be used to estimate the discharge power that is suitable for the plasma-catalyst system and the sinusoidal voltage waveform in this experiment. As understood from Equation (8), the inclusion of n-heptane and naphthalene in the feed can significantly change R and C_{cg}, due to the changes in the gas composition and the surface properties of the catalyst when adsorbing the reactants. Moreover, the resistance and capacitance of the materials strongly depend on the temperature. In summary, the discharge power strongly depends on the applied voltage and the temperature of the plasma system. The dependence of the discharge power on the gas composition in the feed followed the order $(C_{10}H_8 + C_7H_{16}) < C_7H_{16} < C_{10}H_8$, which was correlated with the concentration of CO_2 produced during the experiments, i.e., the CO_2 produced was in the order: $C_{10}H_8 < C_7H_{16} < (C_{10}H_8 + C_7H_{16})$. This suggests that the discharge power tended to decrease as the concentration of CO_2 in the discharge zone increased.

$$P = \frac{V_{DBD}^2}{2} \frac{1}{R\cdot(1+\frac{C_{cg}}{C_d})^2 + \frac{1}{\omega^2 C_d^2 \cdot R}} \tag{8}$$

where

VDBD is the amplitude of the voltage applied to the reactor

R is the equivalent resistance of the reactor system

C_{cg} is the equivalent capacitance of the catalyst and gas gap

C_d is the absolute capacitance of the dielectric layers.

3.2.2. Removal of NO_x and soot simulant by SCR coupled with plasma

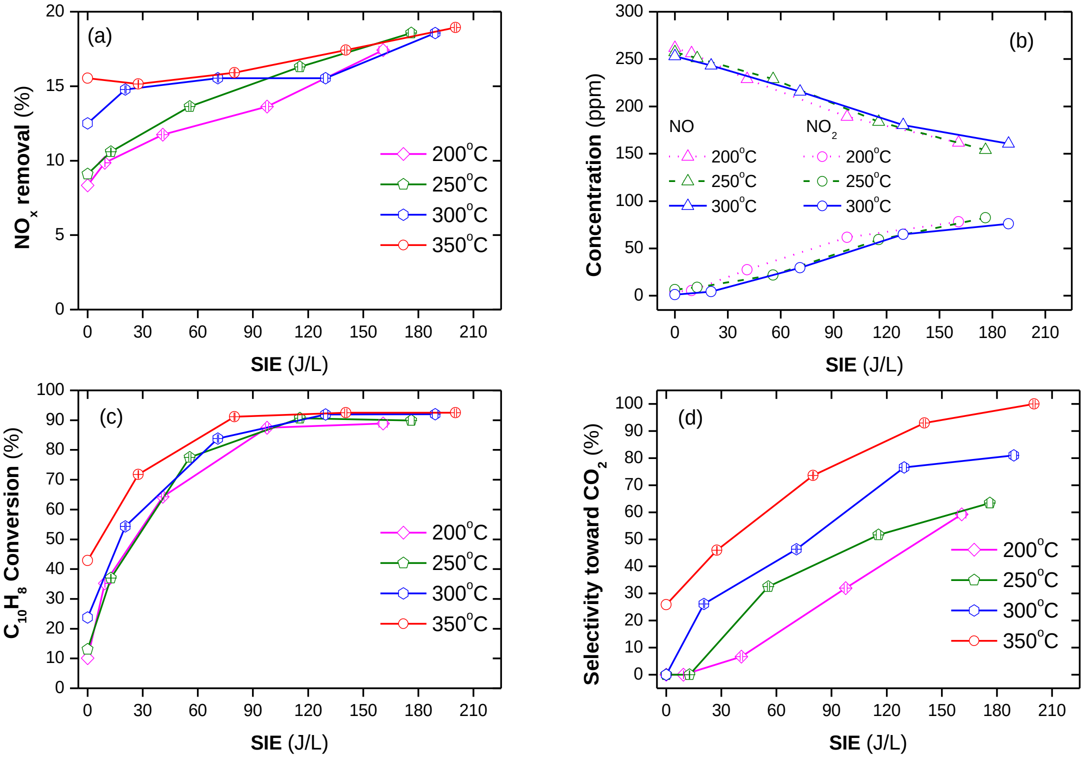

Fig. 3.12. NO_x and naphthalene removal by plasma-catalyst at various temperatures and specific input energy (SIE) (a) NO_x conversion, (b) concentrations of NO and NO_2, (c) naphthalene conversion, and (d) selectivity toward CO_2 (total flow rate of 2 L/min including 300 ppm NO, 48 ppm naphthalene, 3.7% H_2O, 10% O_2, and N_2 as balance).

Naphthalene (soot simulant) played the role of the reducing agent in the SCR of NO_x as shown in Fig. 3.12(a). The conversion of NO_x was 8 to 20% in the temperature range of 200–350 ℃ along with an SIE of 0–210 J/L. The SIE is defined as the power in W divided by gas flow rate in L/s. The removal of NO_x tended to increase with the increasing temperature and SIE. The previous reports indicated that without a reducing agent, NO_x removal neither occurred in the plasma nor the plasma-catalyst processes, only in the oxidization of NO to NO_2 [42,50]. Naphthalene containing two aromatic rings can function as a reducing agent [27,56]. Similar to other hydrocarbons, naphthalene produces partially oxidized intermediate products. Subsequently, NO_x reduction is performed via chemical reactions with the intermediate products. For this experiment, the concentration of naphthalene was 48 ppm. It is argued that this low concentration is the reason for the low NO_x removal. Fig. 3.12(b) shows the concentration of NO and NO_2 when the temperature varies from 200 to 300 ℃ and SIE varies from 0 to 210 J/L. This demonstrated that a part of NO was oxidized to NO_2 in the presence of plasma. The catalytic destruction of naphthalene hardly occurs at low temperatures because it is stabilized by resonance hybrid, i.e., high temperature and high SIE are needed for the decomposition of this compound. Figure 3.12(c) indicates that, even at an operating temperature of 350 ℃, naphthalene conversion was approximately 40%. However, almost all naphthalene was destroyed with SIE above 90 J/L in the temperature range of 200–350 ℃. Furthermore, the selectivity toward CO_2 increased as the temperature and SIE increased, as shown in Fig. 3.12(d). Overall, the soot simulant (naphthalene) can function as a reducing agent of SCR for NO_x removal. Further, poor catalytic destruction of naphthalene at low temperatures can be overcome with the help of plasma. According to the above results, the soot simulant can act as a reducing agent for SCR of NO_x. However, the efficiency of NO_x removal was not satisfactory with 48 ppm naphthalene tantamount to a C/N ratio of 1.6 (the ratio of carbon concentration in the hydrocarbon to nitrogen concentration in NO_x). Previous reports indicated that n-alkane is an effective reducing agent for the HC-SCR process [29], [73].

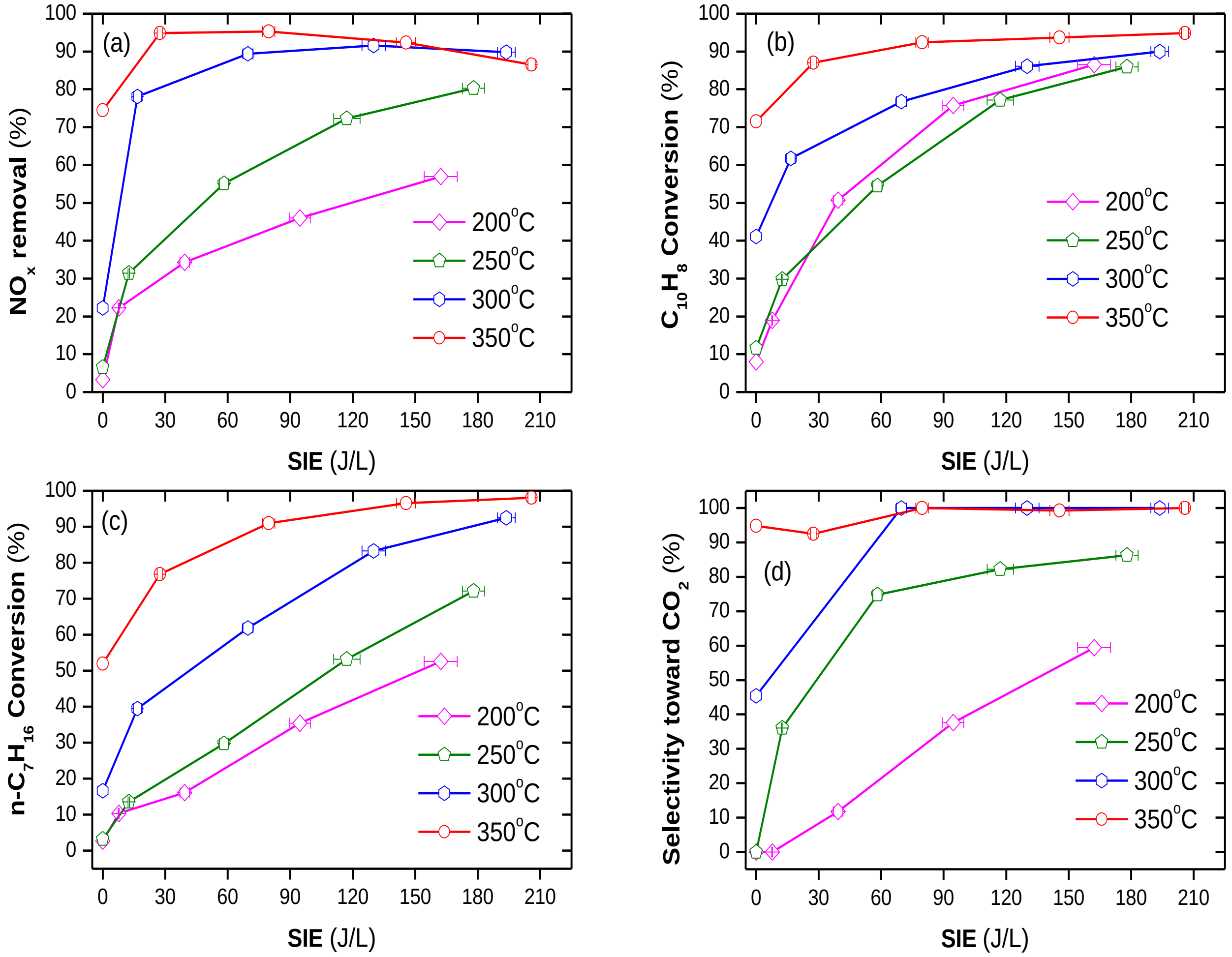

Fig. 3.13. NO_x and naphthalene removal by plasma-catalyst at various temperatures and SIE values (a) NO_x removal efficiency, (b) naphthalene conversion, (c) n-heptane conversion, and (d) selectivity toward CO_2 (total flow rate of 2 L/min including 300 ppm NO, 48 ppm naphthalene, 265 ppm n-heptane, 3.7% H_2O, 10% O_2, and N_2 as balance).

In general, dodecane ($C_{12}H_{26}$) can represent diesel fuel. However, this component has low vapor pressure, making it difficult to vaporize and inject into the feed gas. Thus, for the simplicity of the experimental procedure, n-heptane having relatively low vapor pressure was used as a reducing agent instead of dodecane. The effect of n-heptane on the simultaneous removal of NO_x and the soot simulant was examined at temperatures ranging from 200 to 350 ℃ and SIE from 0 to 210 J/L. The results are shown in Fig. 3.13. The efficiency of NO_x removal increased sharply when a combination of plasma and n-heptane was used, as shown in Fig. 3.13(a-b). Specifically, at an operating temperature at or below 250 ℃, the presence of only n-heptane did not remove NO_x and naphthalene. On the other hand, increasing the SIE value increased the removal of NO_x and naphthalene. At an operating temperature of 300 ℃, NO_x removal without plasma was approximately 22%, whereas a sharp increase was observed in the presence of plasma. The conversion of naphthalene also largely increased to 62–90%, depending on the SIE value. The efficiency of both NO_x and soot simulant removal increased in the presence of n-heptane at 350 ℃ or across the entire temperature range when coupled with plasma. Fig. 3.13(c) demonstrates that there is a correlation between the increase in NO_x removal and n-heptane conversion. This also suggests that n-heptane is the main reducing agent for the NO_x removal process. The tendency of CO_2 to be produced from n-heptane as well as naphthalene increasing with the operating temperature and SIE is shown in Figure 3.13(d). This indicates that, at a high temperature and input energy, complete oxidization of n-heptane and naphthalene to CO_2 occurred, i.e., the selectivity toward CO_2 is nearly 100% at 350 ℃ and SIE $\geq$ 80 J/L. The presence of n-heptane, at operating temperatures at or above 300 ℃ or the presence of plasma at low temperatures, can account for the increase in NO_x and naphthalene removal. This is in line with the previous report [29], which indicated that the conversion of n-heptane to derivative hydrocarbons or CO_2 started to occur at 290 ℃ over the catalyst, whereas the plasma-catalyst process-induced n-heptane conversion at a low operating temperature. Consequently, with the catalyst alone, n-heptane neither enhanced the removal of NO_x nor that of naphthalene at a low operating temperature (≤250 °C), as shown in Fig. 3.14.

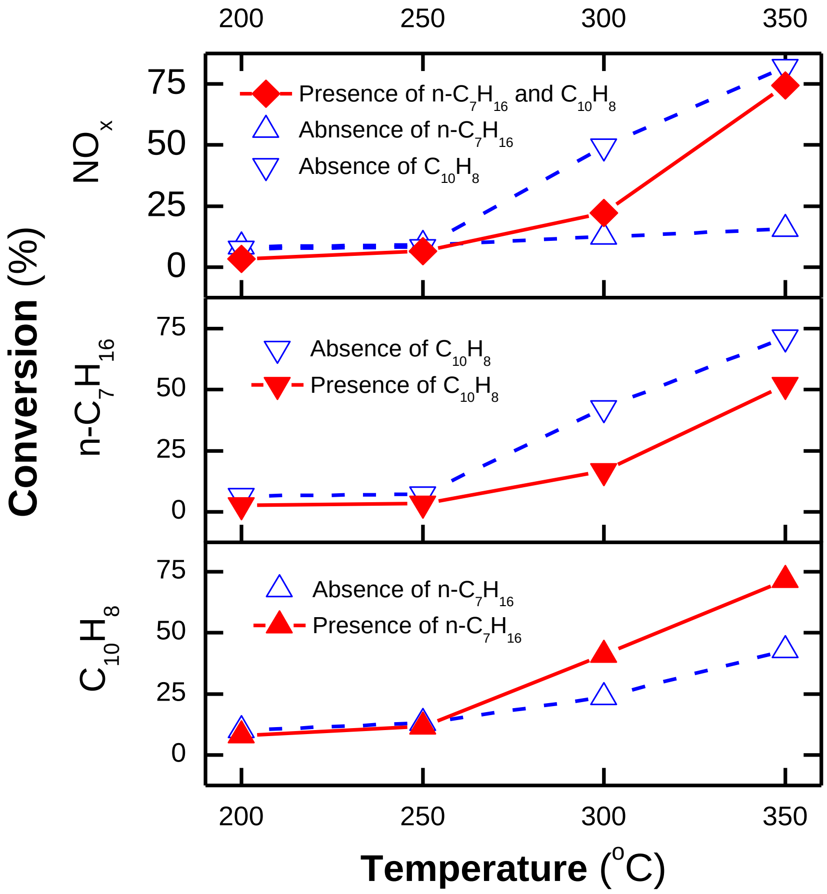

Fig. 3.14. NO_x removal efficiency and conversion of n-heptane and naphthalene by the catalytic process with/out n-heptane and naphthalene at various operating temperatures (total flow rate fixed at 2 L/min, including 300 ppm NO, 48 ppm naphthalene, 265 ppm n-heptane, 3.7% H_2O, 10% O_2, and N_2 as balance).

The conversion of NO_x and n-heptane by the catalytic process decreased in the presence of naphthalene. These phenomena are caused by the adsorption of naphthalene on the catalyst, which deactivates the catalytic active sites. However, the issue was solved by using plasma. Consequently, at high SIE (≥90 J/L) and operating temperatures at or above 300 ℃, more than

70% of NO_x, naphthalene, and n-heptane were converted.

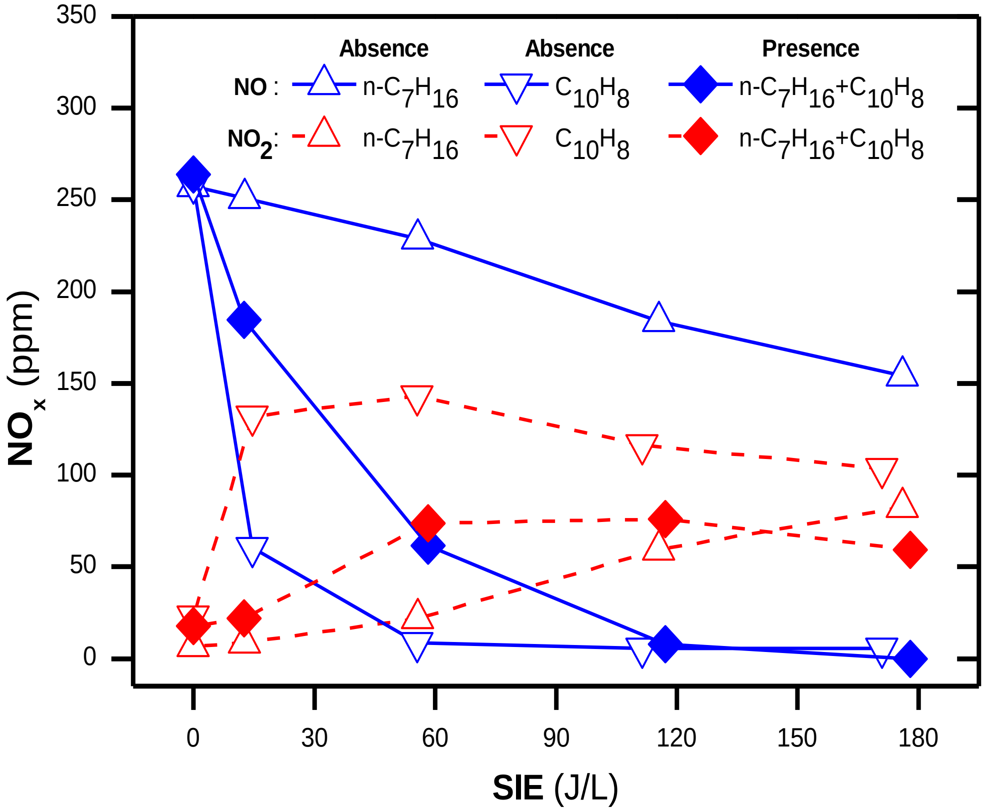

Fig. 3.15. Concentrations of NO and NO_2 as a function of SIE for different gas compositions at 250 ℃ (total flow rate of 2 L/min including; 300 ppm NO, 265 ppm n-heptane, 48 ppm naphthalene, 3.7% H_2O, 10% O_2, and N_2 as balance).

Figure 3.15 demonstrates the difference between using 48 ppm naphthalene (C/N = 1.6) and 265 ppm n-heptane (C/N = 6) as a reducing agent during the NO_x removal process at an operating temperature of 250 ℃. A larger amount of NO is converted or oxidized to NO_2 when n-heptane is present in the feed gas. However, the presence of naphthalene presented little conversion or oxidization of NO. Regarding the mechanism during NO_x removal by the plasma-catalyst (R1–R6), NO can be oxidized to NO_2, which is allowable according to R1–R2. In fact, in the absence of hydrocarbon, NO_x was not removed by using the plasma-catalyst process. However, in the presence of hydrocarbon in conjugation with plasma, NO_x removal can be performed by other reactions (R3–R6), which are also adapted from the same paper [29]. The difference between n-heptane and naphthalene during the NO_x removal process can be explained by the differences in the molecular structure (naphthalene: polycyclic aromatic hydrocarbon; n-heptane: straight-chain hydrocarbons) and in the bond dissociation energies (BDEs) of C-H and C-C in naphthalene and n-heptane. For information, the BDEs of C-H and C-C of n-heptane are (410–415.7 kJ/mol) and (361.0–368.2 kJ/mol), respectively, whereas those of naphthalene are (469.4–482.8 kJ/mol) [57]. Another reason was that the total carbon concentration in 265 ppm n-heptane (1855 ppm carbon) was higher than that of 48 ppm naphthalene (480 ppm carbon).

$$NO + O\bullet + e/M \rightarrow NO_2 + e/M \quad (R1)$$

$$NO + O_3 + e/M \rightarrow NO_2 + e/M \quad (R2)$$

$$HC + O\bullet + e/M \rightarrow \bullet R, RO, RO_2, OH, \ldots + e/M \quad (R3)$$

$$NO + RO_2 + e/M \rightarrow NO_2 + RO + e/M \quad (R4)$$

$$NO_x + \bullet R \rightarrow \text{Products} \quad (R5)$$

$$NO_x + C_xH_yO_z + e/M \rightarrow N_2 + CO_2 + H_2O + e/M \quad (R6)$$

Here, e denotes energetic electrons, and M stands for excited molecules.

3.2.3. Removal of NO_x and soot during operating temperature fluctuations

The temperature of the exhaust gas ordinarily fluctuates and depends on the operating state; e.g., the gas temperature of diesel-powered passenger cars fluctuates in the range of 180–350 ℃ [119]. This suggests that the efficiency of NO_x and soot removal over a catalyst subjected to temperature fluctuation is a factor when evaluating the catalyst for potential practical applications. This section discusses the removal of NO_x and soot by

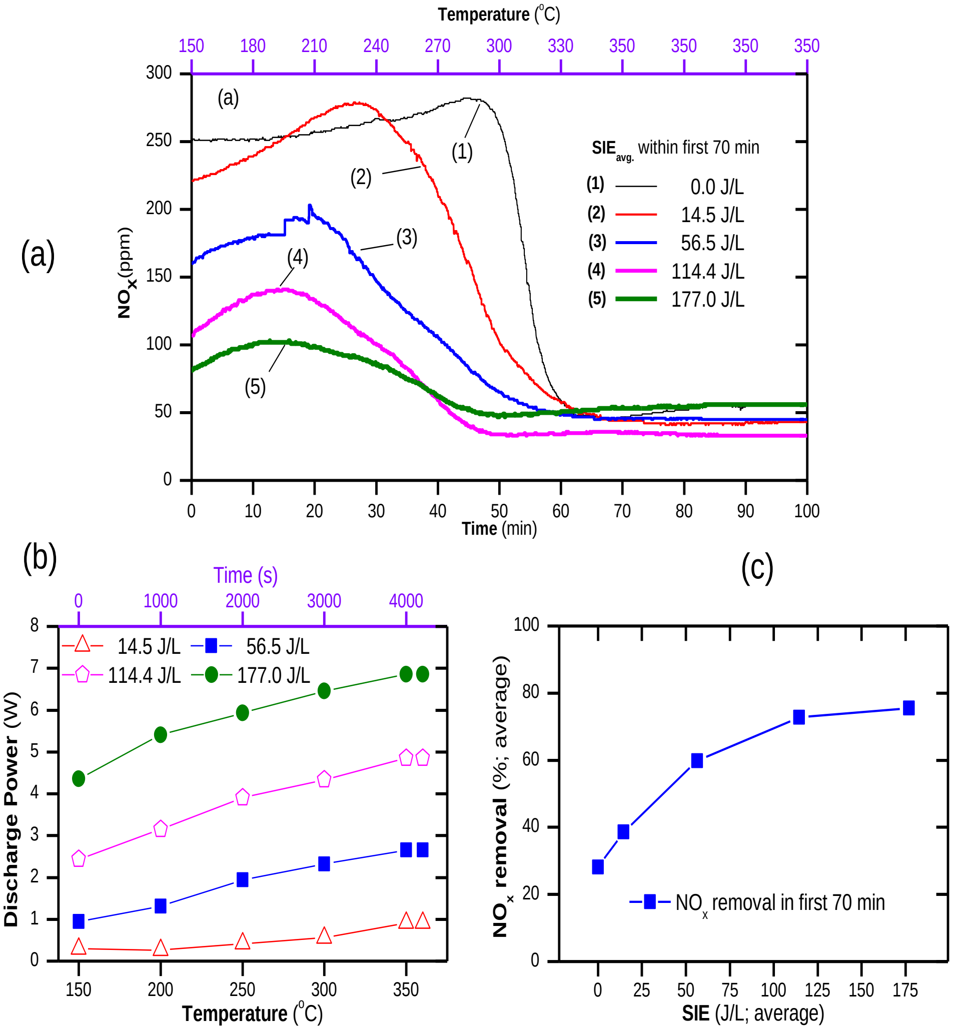

Fig. 3.16. (a) Evolution of NO and NO_2 during the temperature increase from 150 to 350 °C at a rate of 3 °C/min and then being maintained at 350 °C for both catalyst and plasma-catalyst, (b) changes in discharge power with temperature, and (c) average NO_x conversion in the first 70 min (total flow rate of 2 L/min including; 300 ppm NO, 48 ppm naphthalene, 265 ppm n-heptane 3.7% H_2O, 10% O_2 and N_2 as balance).

increasing the temperature at a rate of 3 ℃/min in the range of 150–350 ℃ and by increasing the average SIE within the first 70 min from 0 to 177 J/L. The catalyst temperature window was expanded by the presence of plasma, as shown in Fig. 3.16. As seen, the catalyst-alone process reduced the concentration of NO_x effectively when the operating temperature was above 300 ℃. On the contrary, the plasma catalyst can obtain a low concentration of NO_x at operating temperatures from 150 ℃ upward. The concentration of NO_x decreased with increasing SIE_{avg}. However, at high temperatures (≥ 300 ℃) and high SIE (177 J/L), the NO_x concentration increased slightly due to the generation of NO_x by plasma, as shown in Fig. 3.16(a). As indicated by the above result, the discharge power depends on the discharge state, i.e., the temperature, applied voltage, and gas composition. Therefore, during temperature fluctuation, the discharge power necessarily changed with the processing time. As seen in Fig. 3.16(b), the discharge power was getting increased with the operating temperature. The average SIE, i.e., SIE_{avg}, can be estimated using Eq. 9, and the average NO_x using Eq. 10. As a result, the average NO_x removal within the first 70 min as a function of the average of SIE was plotted and is shown in Fig. 3.16(c). This suggests that poor NO_x removal under the conditions of temperature fluctuation during the catalytic process can be improved by the combination of plasma with an average SIE of 60-120 J/L.

$$\mathrm{SIE_{avg}} = \frac{1}{\mathrm{T \times F}} \int_0^{\mathrm{T}} \mathrm{P(t)dt} \qquad (9)$$

$$\mathrm{Conversion_{avg}} = 1 - \frac{1}{\mathrm{T}} \int_0^{\mathrm{T}} \left(\frac{\mathrm{C}}{\mathrm{C_o}}\right)\mathrm{dt} \qquad (10)$$

Here, F denotes total flow rate, [t1 - t2] is the time duration for collecting data during temperature fluctuation, and the subscript “avg” indicates the average value.

The ratio of the concentration at the outlet and inlet (C/C_o) for both naphthalene and n-heptane during the temperature program (150–350 ℃ at a rate of 3 ℃/min) is shown in Fig. 3.17. These conversions can be also estimated by equation 10. The initial increases of naphthalene at low SIE_{avg} can be explained by desorption. Due to its low vapor pressure, naphthalene adsorbed at low temperatures, after which it underwent desorption at high operating temperatures. Here, the temperature at which C/C_o of naphthalene reached a maximum value decreased as the SIE increased, which is a result of the decomposition of naphthalene by plasma. Specifically, the temperature showing maximum for the catalyst-alone process was 315 ℃, whereas the temperatures showing maximum decreased to 270 and 250 ℃ with SIE_{avg} of 14.5 and 56.5 J/L, respectively.

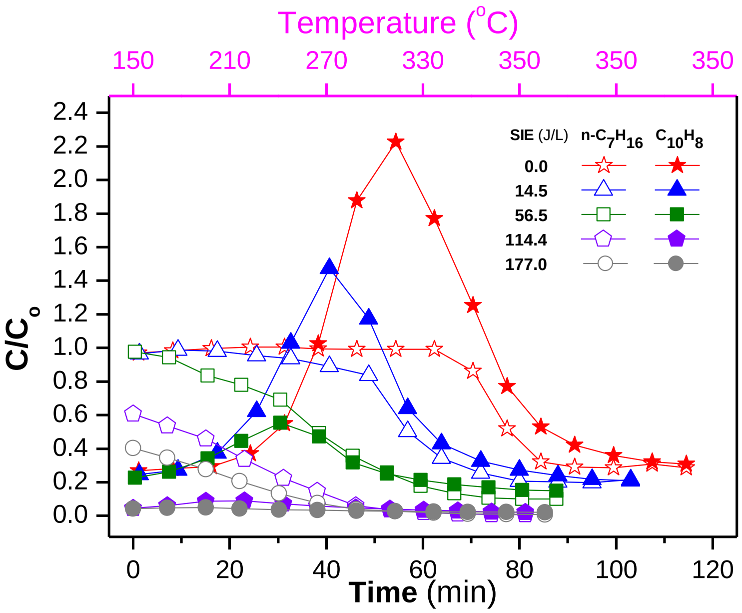

Fig. 3.17. Evolution of concentration ratio of outlet and inlet (C/Co) of naphthalene and n-heptane during the temperature increase from 150 to 350 °C with a rate of 3 °C/min and then maintained at 350 °C for both catalyst and plasma-catalyst (the conditions are the same as in Fig. 3.16).

Not only the temperatures showing maximum, but also C/C_o of naphthalene largely decreased with the combination of plasma. In the case of high SIE_{avg} of 114.4 and 177.0 J/L, almost all naphthalene in the feed was removed. In contrast to naphthalene, the concentration of n-heptane did not show maximum and decreased as the SIE and operating temperature increased. The difference between n-heptane and naphthalene is due to their adsorption capabilities and vapor pressures. Note that the vapor pressure of n-heptane (3,985 Pa at 290 K) is greater than that of naphthalene (4.9 Pa at 290 K). The presence of plasma-enhanced the removal of NO_x and naphthalene under fluctuating temperature conditions.

3.3. Summary

This work presented catalytic NO_x removal coupled with plasma in a wide temperature range below 350 ℃. Ag and Cu supported on ZSM5 zeolite were used as the catalysts to remove NO_x. The results showed that the NO_x removal rate over Ag/ZSM5 was higher than that over Cu/ZSM5. The NO_x removal efficiency based on Ag/ZSM5 catalyst coupled with plasma exceeded 80% at low operating temperatures. The oxidation of NO to NO_2 was approximately 100% at temperatures of 200–300 ℃. Plasma-catalytic NO_x removal mechanisms at low temperatures were discussed. This article demonstrated that the plasma-coupled Ag/ZSM5 catalyst can be an efficient solution for low-temperature NO_x removal.

In the case of NO_x and the soot simulant removal simultaneously from diesel emissions in a fixed-bed DBD reactor in the temperature range from 150 to 350 ℃. The results demonstrated that the use of a plasma-catalyst process at low operating temperatures increased the removal of both NO_x and naphthalene (soot simulant). Moreover, the soot simulant functioned as a reducing agent for NO_x removal, but with low NO_x conversion. The high efficiency of NO_x removal required the addition of hydrocarbon fuel. In summary, the combined use of the catalyst and plasma (specific input energy, SIE ≥ 60 J/L) solved the poor removal of NO_x and soot at low operating temperatures or during temperature fluctuations in the range of 150–350 ℃. Specifically, highly efficient naphthalene removal was achieved with low-temperature adsorption on the catalyst followed by the complete decomposition by the plasma-catalyst at 350 ℃ and SIE of 90 J/L.

CHAPTER 4

PLASMA ASSISTED CATALYSIS FOR VOC DECOMPOSITION

The experimental setup and catalyst preparation for this work was presented in sections 2.2.2 and 2.3.1 (chapter. 2).

4.1. Degradation of styrene in a nonthermal plasma-catalytic system over Pd/ZSM-5 catalyst

Redrafted from:

V. T. Nguyen et al., Plasma Chem. Plasma Process., vol. 40, no. 5, pp. 1207–1220, 2020.

4.1.1. Characterizations of the catalysts

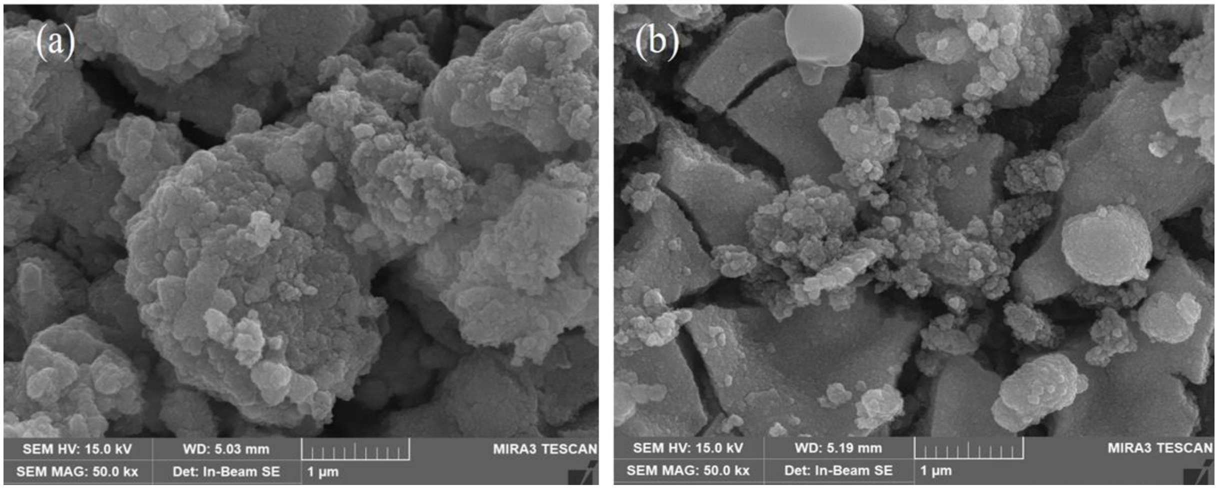

Fig. 4.1. SEM images of (a) the Pd/ZSM-5 catalyst before, and (b)after the reactions.

Figure 4.1 shows the SEM images of the Pd/ZSM-5 before the reaction and after the reaction. The particle size of Pd before the reactions (Fig. 4.1(a)) was found to be larger than that after the reactions (Fig. 4.1(b)). This change in the particle size distribution indicates that the plasma treatment of the catalyst can lead to highly dispersed metal clusters. According to the previous study [120], the metal particles supported on the surface can act as electron sinks, and thus strong Coulomb repulsions existing between the electrons captured on the same particle results in splitting it up.

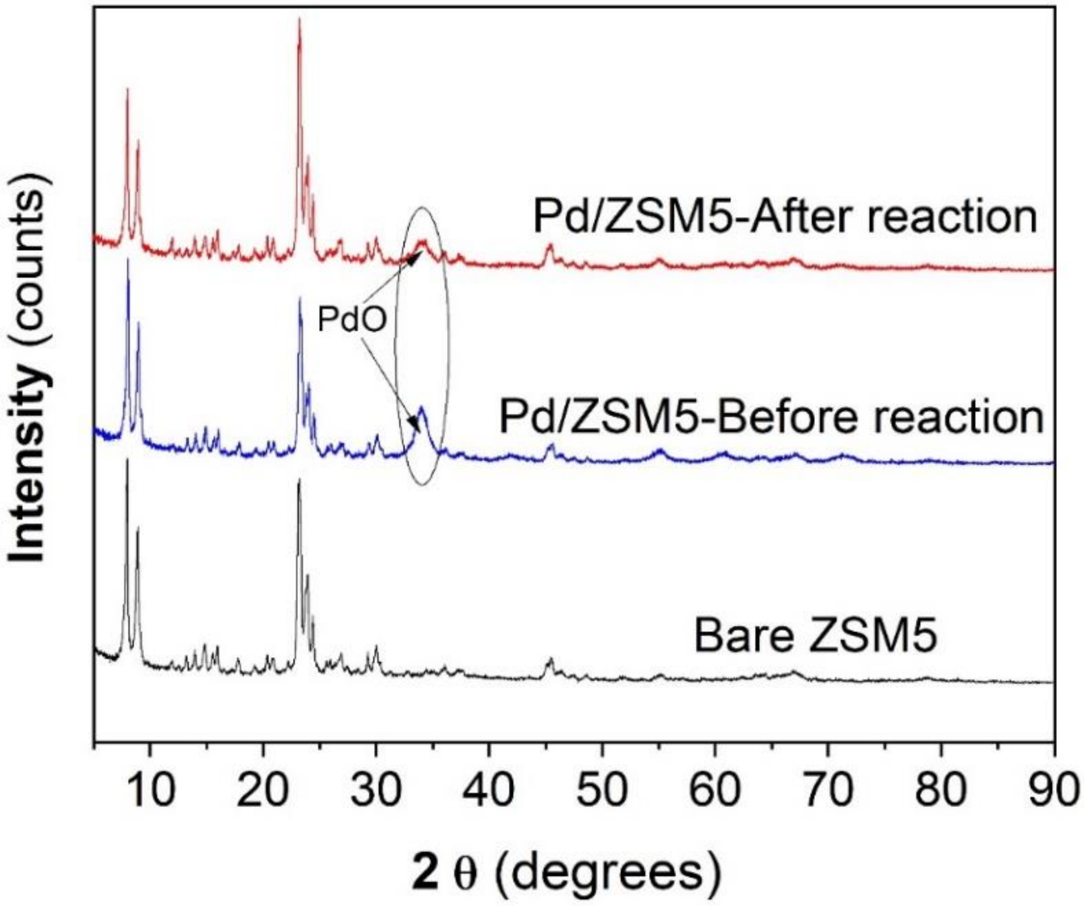

Fig. 4.2. XRD patterns of the bare ZSM5 and Pd/ZSM5 before and after the reactions.

The change in the Pd particle size can be further confirmed by the X-ray diffractograms. Fig. 4.2 presents the XRD patterns for the bare ZSM5 and Pd/ZSM5 before and after the plasma-catalytic reactions. The ZSM5 crystalline structure was maintained regardless of the plasma treatment. It is noteworthy that the peak related to the crystalline phase of Pd^{2+} before the reactions is bigger in height than that after the reactions. The bigger peak implies that the particle size is bigger, and vice versa, which agrees well with the SEM images in Fig. 4.1. As aforementioned, this result can be explained by the improved dispersion of Pd particles over the ZSM5 surface as a result of the plasma treatment.

4.1.2. Styrene adsorption and decomposition

Figure 4.3 shows the styrene uptake capabilities on the Pd/ZSM5 catalyst, which was obtained by measuring the outlet concentration of styrene as a function of adsorption time. The airstream containing 40 ppm of styrene was passed through the catalyst bed, and the catalyst was saturated with styrene in 12 h. At the very beginning of the adsorption, styrene was almost completely absorbed by the catalyst; afterward, the concentration of styrene gradually increased, reaching the inlet concentration in 720 min. The adsorption capacity of Pd/ZSM5 catalyst was estimated to be 181.6 μmol/g. The pore structure of the catalyst adsorbs the reactant molecules, plasma-generated active species, and the products of the oxidative reactions [121]. The plasma works more efficiently when paired with catalysis because the adsorbed species can be retained longer than those in the gas phase. The diffusion of styrene molecules and plasma-generated active species into zeolite micro-pores results in surface reactions between them.

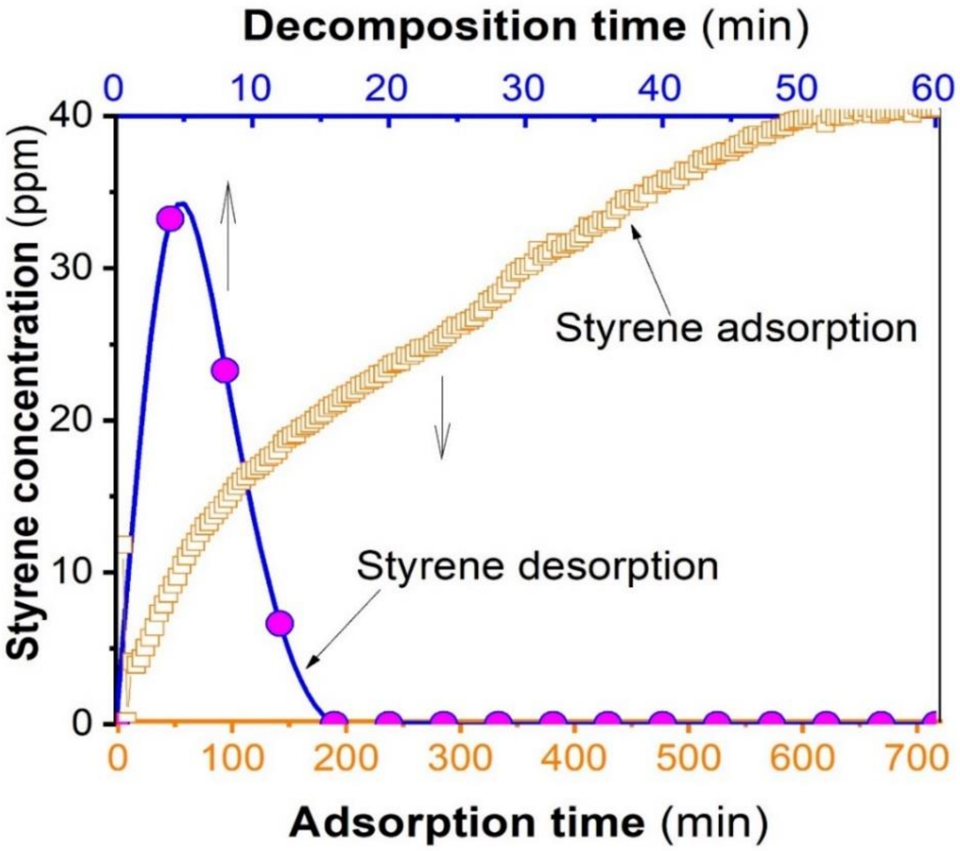

Fig. 4.3. Concentrations of styrene at the reactor outlet obtained during the room-temperature adsorption of 40 ppm styrene in 5 L/min air and that during the plasma-catalytic decomposition at an SIE of 60 J/L.

Right after the adsorption, a stream containing only dry air was fed to the plasma-catalytic reactor, and the plasma was turned on at an energy density of 60 J/L to decompose the adsorbed styrene. In Fig. 4.3, most of the styrene adsorbed on the catalyst was decomposed and desorbed in 20 min. Although all the experiments were conducted with a mixture of styrene and dry air, water vapor can exist due to the oxidation of styrene. The competitive adsorption of water vapor has a negative effect on styrene adsorption [122]. The formation and adsorption of water vapor lead to the replacement and desorption of styrene molecules.

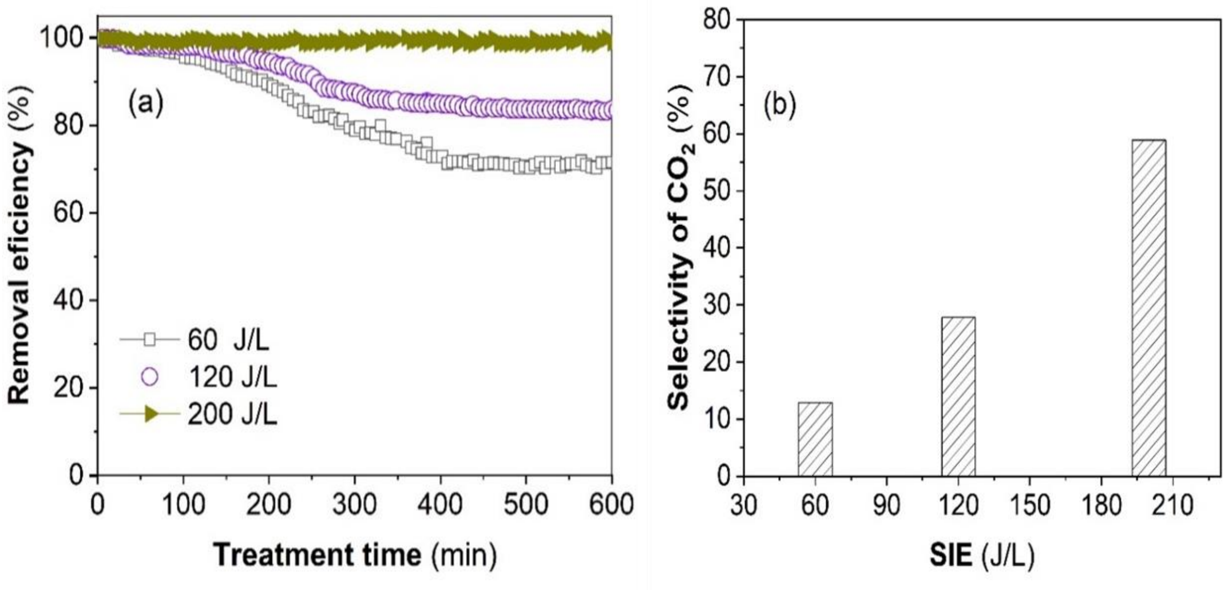

Fig. 4.4. (a) Temporal variations of the plasma-catalytic styrene removal efficiency at different SIE values, and (b) the steady-state CO_2 selectivities (5 L/min of air; 100 ppm styrene).

Fig. 4.4(a) shows the temporal variations of the styrene removal efficiency at different SIE values. When the SIE was lower, the styrene removal decreased with time to 78% and 88% after 600 min at 60 J/L and 120 J/L, respectively. On the other hand, the styrene degradation efficiency at 200 J/L was maintained at approximately 100%. The energy efficiency for styrene removal depends on the degree of removal, the inlet concentration, the type of catalyst, the oxygen content, etc. The energy efficiencies estimated at the SIE values of 60, 120, and 200 J/L were 5.5×10^{-6}, 3.1×10^{-6} kg/kJ and 2.1×10^{-6}, respectively, which are in the same order as in a previous study (3.0×10^{-6} ~ 5.3×10^{-6} kg/kJ) conducted with TiO_2/γ-alumina at a styrene concentration of 1000 mg/m^3 [30]. The formation and adsorption of byproducts, especially low-volatile organic compounds on the catalyst surface deactivate the catalyst. The increase in the SIE promotes the generation of reactive species such as energetic electrons and oxidative radicals in the plasma zone, leading to more mineralization, which can explain the stable removal efficiency over time. Besides, the selectivity towards CO_2 was significantly improved with increasing the SIE, as observed in Fig. 4.4(b). In detail, the selectivity towards CO_2 increased by approximately 50% with increasing the SIE from 60 to 200 J/L.

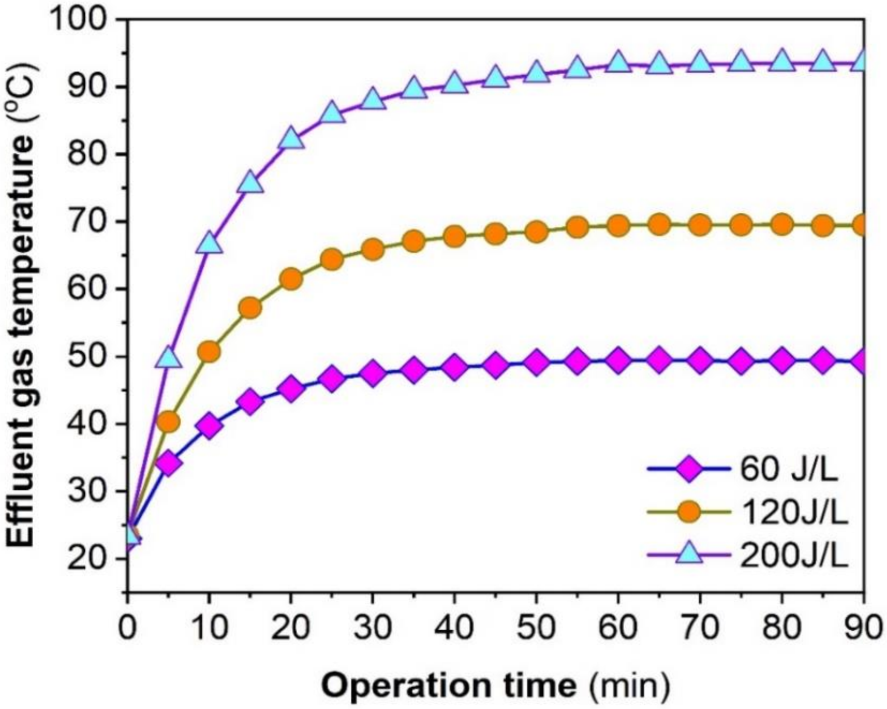

Fig. 4.5. Temporal variations of the effluent temperature at different SIE values.

Again, this result can be explained by the more mineralization owing to the increased production of reactive species. Fig. 4.5 shows the effluent temperatures measured at different SIE values as a function of time. Following the increase in the early stage, the temperature reached a steady state. The temperature increased up to higher than 90 °C, depending on the SIE value. This temperature increase can also explain in part the better plasma-catalytic activity at higher SIE values. The SIE at a given voltage did not nearly change during the operation time, after a slight increase in the beginning due to the temperature increase, as presented in Fig. 4.6(a). The higher the applied voltage is, the higher the SIE value is, since the discharge power mainly depends on the applied voltage. The applied voltage required for an SIE value was much lower when the reactor was packed with the catalyst pellets (Fig. 4.6(b)). For instance, 12.6 kV was needed to get an SIE of 60 J/L with the Pd/ZSM, which is much lower than 17 kV without packing. The dielectric constant of the catalyst is greater than the gas, and it is natural that a higher electric field is required for plasma inception without packing [123].

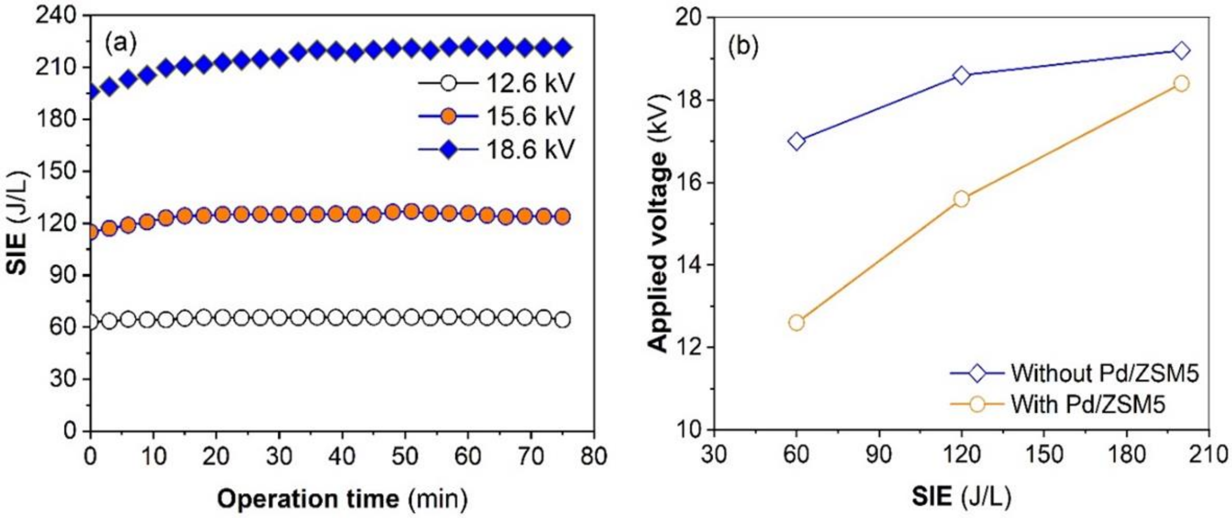

Fig. 4.6. Temporal variations of the SIE values (a) and the relation between the applied voltage and the SIE (b).

4.1.3. Formation and decomposition of ozone

Ozone is the most abundant product of the plasma discharge in the air since oxygen is one of the main constituents of air and its bond dissociation energy is much lower than nitrogen [34], [123]. Ozone, a long-lived species, takes an important part in the mineralization of organic compounds to CO_2 [124]–[126]. It directly participates in heterogeneous oxidation reactions on the catalyst surface and enhances the catalytic activity [127]. To get an insight into the role of ozone in the styrene oxidative process, the ozone concentration at the outlet of the reactor was monitored by varying the SIE in the range of 60 to 200 J/L.

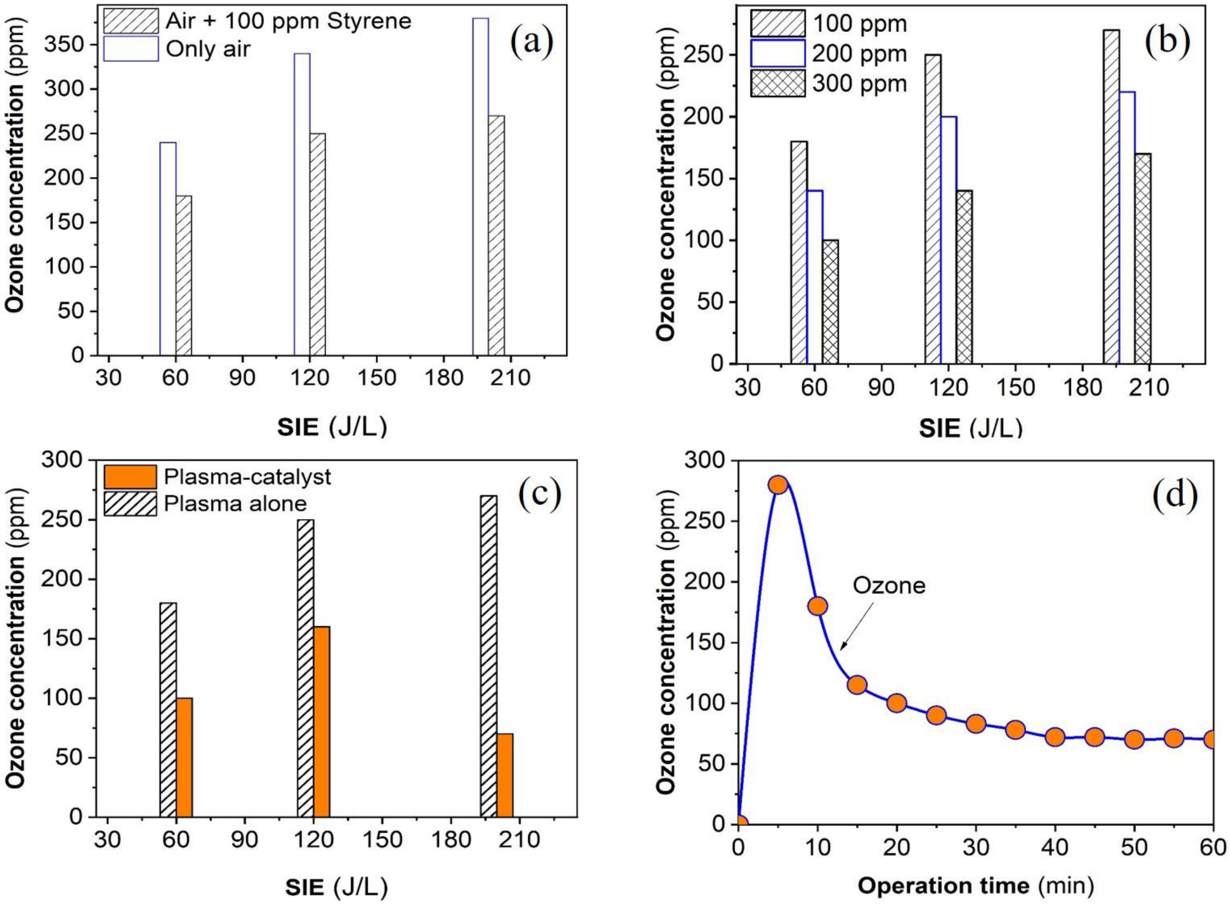

Fig. 4.7. Ozone concentrations obtained after 1-h operation at the outlet of the reactor without the catalyst packing (a), the effect of the styrene concentration on the emission of ozone (after 1-h operation) (b), the effect of the catalyst presence on the emission of ozone (after 1-h operation) (c), and the temporal variations of the ozone concentration during the operation at 18.6 kV (d).

Fig. 4.7(a) presents the outlet ozone generation obtained with the plasma reactor without packing the catalyst, where the ozone concentration of the discharge in pure air is compared with the case of a mixture of air and styrene. It is obvious from the figure that the ozone concentration is lower with 100 ppm styrene at all SIE values. Moreover, the ozone concentration decreased with increasing the styrene concentration from 100 ppm to 300 ppm, as in Fig. 4.7(b), indicating that ozone participated in the oxidation reactions [128]. Even though ozone was involved in the styrene oxidation, the outlet concentration was still high without catalyst packing. The issue associated with the unreacted ozone may be overcome by the use of catalysts. The results in Fig. 4.7(c) clearly show that the ozone concentration largely decreased with the catalyst. This phenomenon can be explained by either the catalytic decomposition or the surface reactions between ozone and styrene. Fig4.7(d) shows the temporal variations of the ozone concentration at the reactor outlet obtained at an applied voltage of 18.6 kV (200 J/L). The emission of ozone sharply increased to 280 ppm in 5 min and then decreased, leaving a concentration tail behind. As described earlier in relation to Fig. 4.5, the reactor temperature started to increase when the high voltage was applied. In the early stage before reaching the steady-state, the reactor temperature was low, which can explain the sharp increase in the ozone concentration. Note that the decomposition of ozone strongly depends on the temperature.

4.1.4. Formation of byproducts

The energetic electrons and excited species collide with nitrogen, oxygen, H_2O, and styrene to generate reactive species such as O_3, O, OH, HO_2, N, and H_2O_2 [14,35], which in turn react with styrene both in the gas phase and on the surface. The simultaneous homogeneous and heterogeneous reactions efficiently decompose the styrene molecules. Furthermore, the catalyst with a strong adsorption capability can prolong the retention of the reactants, leading to higher collision probability [36]. The radicals, electrons, and excited molecules can act on chemical bonds such as C–H, C=C, and C-C. The bond dissociation energies of C-H, C-C, and C=C in the aromatic ring are 4.3 eV, (5.0-5.3) eV, and 5.5 eV, respectively [36,37]. The fragments from styrene can further react with oxidative species such as O, O_3, and OH, eventually being oxidized to CO and CO_2. The styrene oxidation mechanisms may be understood and elucidated through the identification of the byproducts. In order to make it easier to identify the byproducts, the concentration of styrene was increased to 500 ppm.

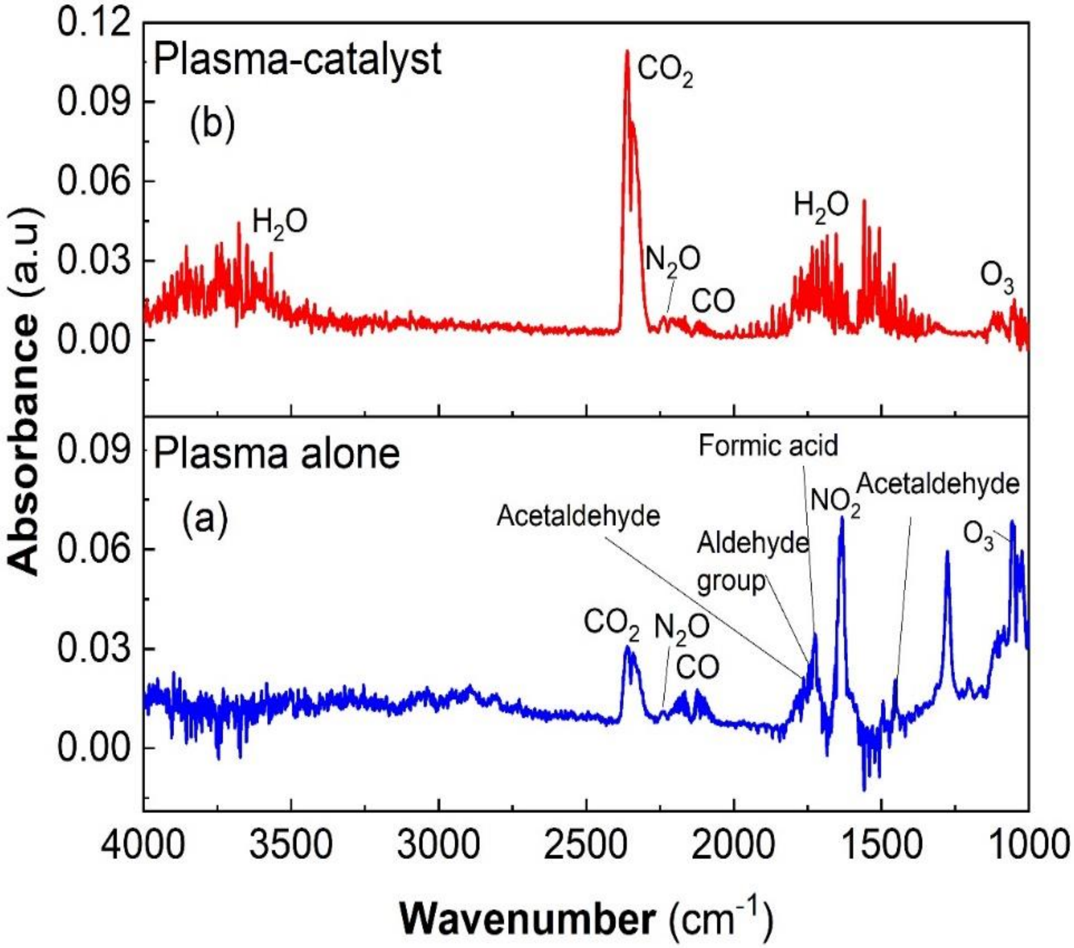

Fig. 4.8. FTIR spectrum of the effluent without the catalyst packing (applied voltage: 16.8 kV) (a) and that with the catalyst packing (b).

The FTIR spectra of the effluent obtained at 16.8 kV are shown in Fig. 4.8, where the results with and without catalyst packing are compared. In the absence of the Pd/ZSM5 catalyst, the plasma produced a variety of byproducts including aldehydes, formic acid, O_3, N_2O, CO, and CO_2. On the other hand, in the presence of the catalyst, aldehydes, formic acid, and O_3 greatly disappeared, and at the same time, the CO_2 concentration largely increased implying that the catalyst promoted the mineralization reactions. The color of the Pd/ZSM5 catalyst after the reaction turned to brownish pink due to the deposition of low-volatile byproducts. The color of the reactor wall and the high voltage electrode surface also changed.

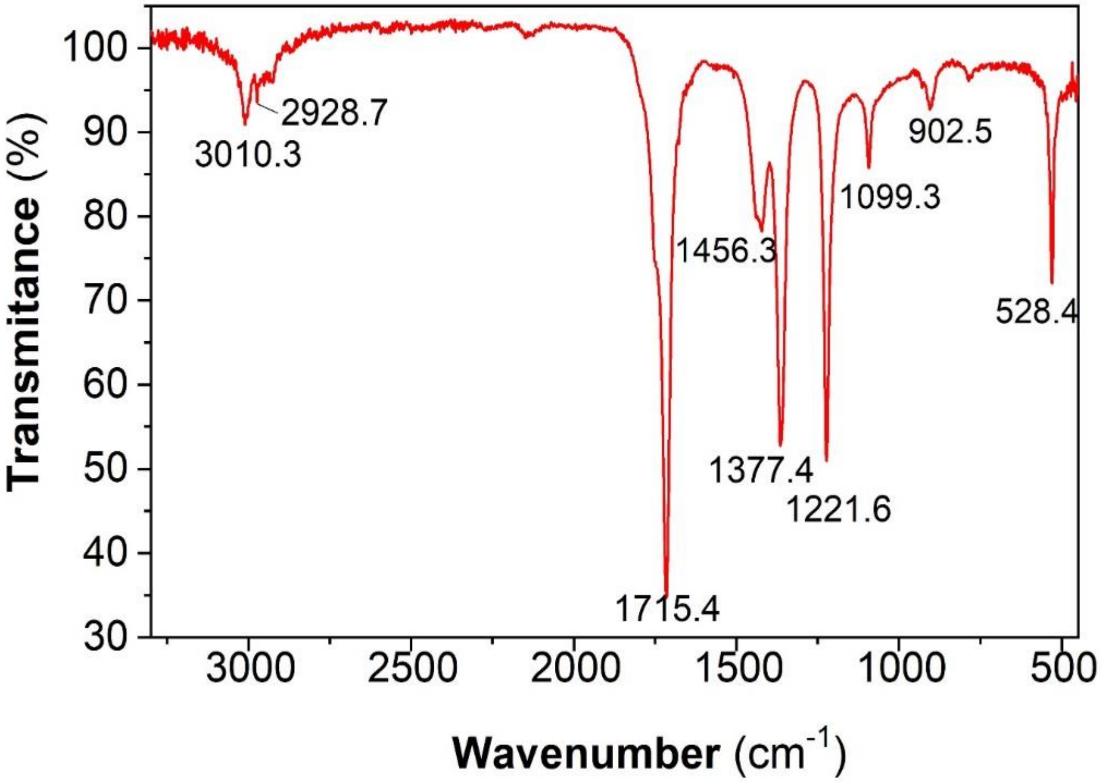

Fig. 4.9. FTIR spectrum of the low-volatile byproduct deposits after the reaction.

The low-volatile byproducts were collected and dissolved in acetone for further analyses using the FTIR and GC-MS. The FTIR spectrum is shown in Fig. 4.9. The symmetrical stretch of the methyl (CH_3) group appears at 3010.3 cm^{-1} [132]. The peak at 2928.7 cm^{-1} is attributed to bending symmetric and asymmetric stretching vibrations of CH_2. The angular deformations of C-H correspond to 1456.3 cm^{-1} (CH_3 asymmetric) and 1377.4 cm^{-1} (CH_3 symmetric). The peak at 1099.3 cm^{-1} is related to the C-O stretching vibrations that correspond to the ester group, and the sharp intensive peak located at 1221.6 cm^{-1} indicates the C-O-C stretching mode [132], [133]. The peak at 1715.4 cm^{-1} confirms the C=O stretching vibrations [121], [132]. Besides, the peak at 528.4 cm^{-1} confirms the presence of styrene copolymers.

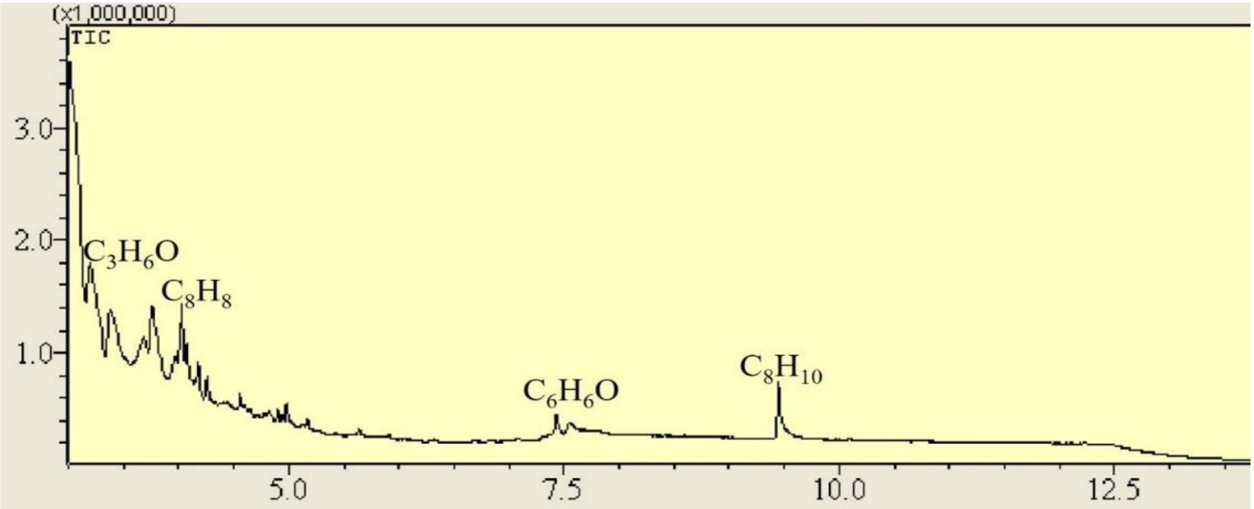

Fig. 4.10. GC-MS spectrum of the low-volatile byproduct deposits (applied voltage 16.8 kV).

Fig. 4.10 provides further information on the deposition of the low-volatile products on the catalyst surface and the reactor wall after the reaction. Through the GC-MS analysis, propionaldehyde (C_3H_6O), styrene (C_8H_8), phenol (C_6H_6O), and ethylbenzene (C_8H_{10}) were identified. The plasma also produced inorganic byproducts.

Fig. 4.11 shows the concentration of NO_2 at the reactor outlet. The concentration of NO_2 increased with increasing the SIE due to the enhanced reaction between oxygen and nitrogen in the air. In this reactor system, NO wasn't detected, which is because NO was quickly oxidized to NO_2 by oxidative species like ozone as soon as it formed. The reactor packed with the Pd/ZSM5 catalyst largely reduced the concentration of NO_2, compared with the plasma-alone case. As shown in Fig. 4.11(b), the concentration of NO_2 decreased with increasing the styrene concentration in the gas stream. This result can be interpreted in part by the reaction of NO_2 with hydrocarbon [38].

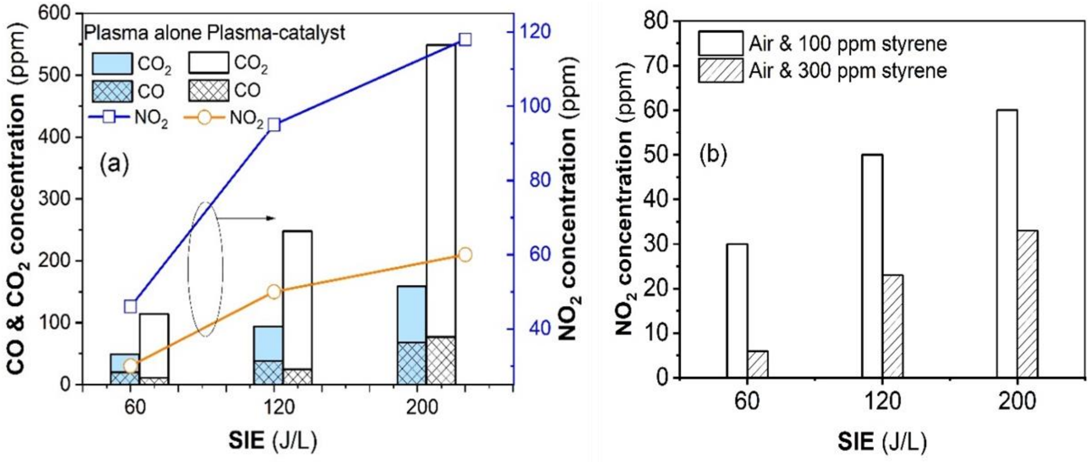

Fig. 4.11. Concentrations of CO, CO_2, and NO_2 were obtained as a function of SIE with and without the Pd/ZSM5 (a) and the concentrations of NO_2 as functions of styrene concentration and SIE (b).

4.2. Summary

The efficient degradation of styrene was investigated in a DBD plasma-catalytic reactor over Pd/ZSM5 catalyst at atmospheric pressure. The problems regarding the individual plasma and catalytic processes such as the poor low-temperature activity of the catalytic process and incomplete oxidation of the plasma process were complemented by the combination of both. The results demonstrated that the plasma-coupled Pd/ZSM5 catalyst significantly enhanced both the styrene oxidation and the CO_2 selectivity as compared with the plasma-alone case, greatly reducing the byproducts. The styrene degradation efficiency proportionally increased with increasing the specific input energy. Ozone formed by the plasma played an important role in the oxidation of styrene. The Pd/ZSM5 catalyst could be activated by the plasma, which greatly enhanced the performance of the styrene removal.

CHAPTER 5

A STUDY ON PLASMA CATALYTIC SYSTEM FOR POLLUTION DEGRADATION TOWARDS PRACTICAL APPLICATION

5.1. Introduction

Although the dielectric barrier discharge reactor filled with catalyst pellets has proven to be efficient for VOC destruction, it still limits solving environmental problems in practice where large amounts of pollutants are processed [16], [134], [135]. This is because the packed-bed DBD reactor using pellets catalyst must be bundled to process a large flow rate of contaminated gas, resulting in a high-pressure drop of the gas across the catalyst layer and also causes the operating cost to increase. Employing a honeycomb structured catalyst is a way to lessen the pressure drop. The advantages of the honeycomb catalyst are its larger surface area, lesser pressure drop, uniform distribution of gas flow, and the ability to process large volumes of gas over packed bed reactors [136]–[139]. However, the main technical challenges are the generation of large volumes of homogenous and stable plasma inside a honeycomb catalyst under atmospheric pressure [137], [140], [141]. Several previous studies have reported that DBD reactor can generate plasma discharge inside the channels of honeycomb-structure [136]–[139]; however, it is difficult to be commercialized or scaled-up when dealing with environmental problems where large amounts of emissions need to be disposed of [16], [23], [44]. Because there is a critical limitation in the discharge gap of the DBD reactor within a few millimeters, which makes it difficult to be generated plasma in a large-size commercial honeycomb monolith catalyst (few centimeters) under atmospheric pressure. In some cases, the DBD reactor can be scaled up in series or parallel by varying the number of reactors. However, this approach can lead to an increase in the overall cost. In addition, the DBD reactors are usually used quartz or glass tubes as a dielectric barrier, which can easily fail by thermal or mechanical shock. These disadvantages make it difficult to apply this technique to solving environmental problems in practice where large amounts of pollutants are processed. In the case of honeycomb corona discharge, the configuration of the reactor is straightforward, with two parallel perforated disk or wire-mesh electrodes covering up both sides of a honeycomb catalyst [44], [142]–[144]. It should also be noted that the electrode system is strong against vibration, therefore, can be used in vehicles [140].

The combined use of plasma and a honeycomb catalyst has been investigated for air pollution removal by several research groups [136], [137], [142], [144]–[148]. However, most of them used a honeycomb catalyst that was small in size and the corona discharge seems to occur outside of the honeycomb catalyst, so the interaction between plasma and catalyst is limited. The honeycomb catalysts used in this work were prepared by applying a coating of γ-alumina (γ-Al_2O_3) powder to the bare cordierite monolith on which to support the palladium (Pd) catalyst to construct a hetero-structural monolithic catalyst. The corona discharge inside the honeycomb catalyst is less affected by its diameter. The AC corona discharge inside real industrial scale catalyst was well reported by our group [38], [44]. However, the changing of operating conditions strongly affects the generation of AC corona plasma inside the honeycomb catalyst. This is a big problem for automobile exhaust treatment or other environmental applications.

In this work, the removal of ethyl-acetate from the air is performed in different types of corona discharge reactor (i.e., generated by AC or DC energization) couple with a honeycomb-structure monolith catalyst (50 × ϕ 50 mm) at atmospheric pressure. EA is widely used as a solvent in the chemical industry, ascendant, and a stable acid ester. EA is also used as an organic raw material and a solvent for coatings and plastic. EA is highly toxic and exposure to this VOC even at low concentrations can cause nausea, dizziness, and even cancer [9], [149], [150].

The effects of various conditions such as the humidity, gas hourly space velocity (GHSV), and gas temperature on the electrical characteristic of both AC and DC discharge were also evaluated and compared with each other. Further, the focus was on identifying the byproducts, which were expected to improve our understanding of the degradation pathway of EA in the NTP plasma catalyst. The use of honeycomb catalyst discharge plasma opens up opportunities for its widespread industrial application for effective VOC treatment.

5.2. Experiment setup

The schematic diagram of the experimental setup for this study is shown in Fig. 2.5. The experimental setup system, catalyst preparation was described in sections 2.2.3, and section 2.3.2 (chapter 2).

5.3. Removal of ethyl-acetate in Air by different types of corona discharges generated in a honeycomb monolith structure coated with Pd/γ-alumina

5.3.1. Characterization of the catalyst

The structure and crystallinity of the bare monolith, γ-Al_2O_3/honeycomb monolith, and Pd/γ-Al_2O_3/honeycomb monolith were analyzed by X-ray diffraction (XRD) as shown in Fig. 5.1. The results indicated the absence of peaks associated with the crystalline phase of γ-Al_2O_3.

The characteristic reflections of γ-Al_2O_3 were not discernible because of its low concentration. The peak at 2θ = 33.55° for Pd/γ-Al_2O_3/honeycomb monolith corresponds to the reflection of (101) plane of palladium oxide (PdO) phase, which is consistent with the standard pattern (JCPDS No. 00-043-1024) [151]. The presence of PdO increases the surface conductivity of the monolith channels, which helps the plasma propagate along the channel surface. In addition, it provides the catalytic activity for the removal of EA.

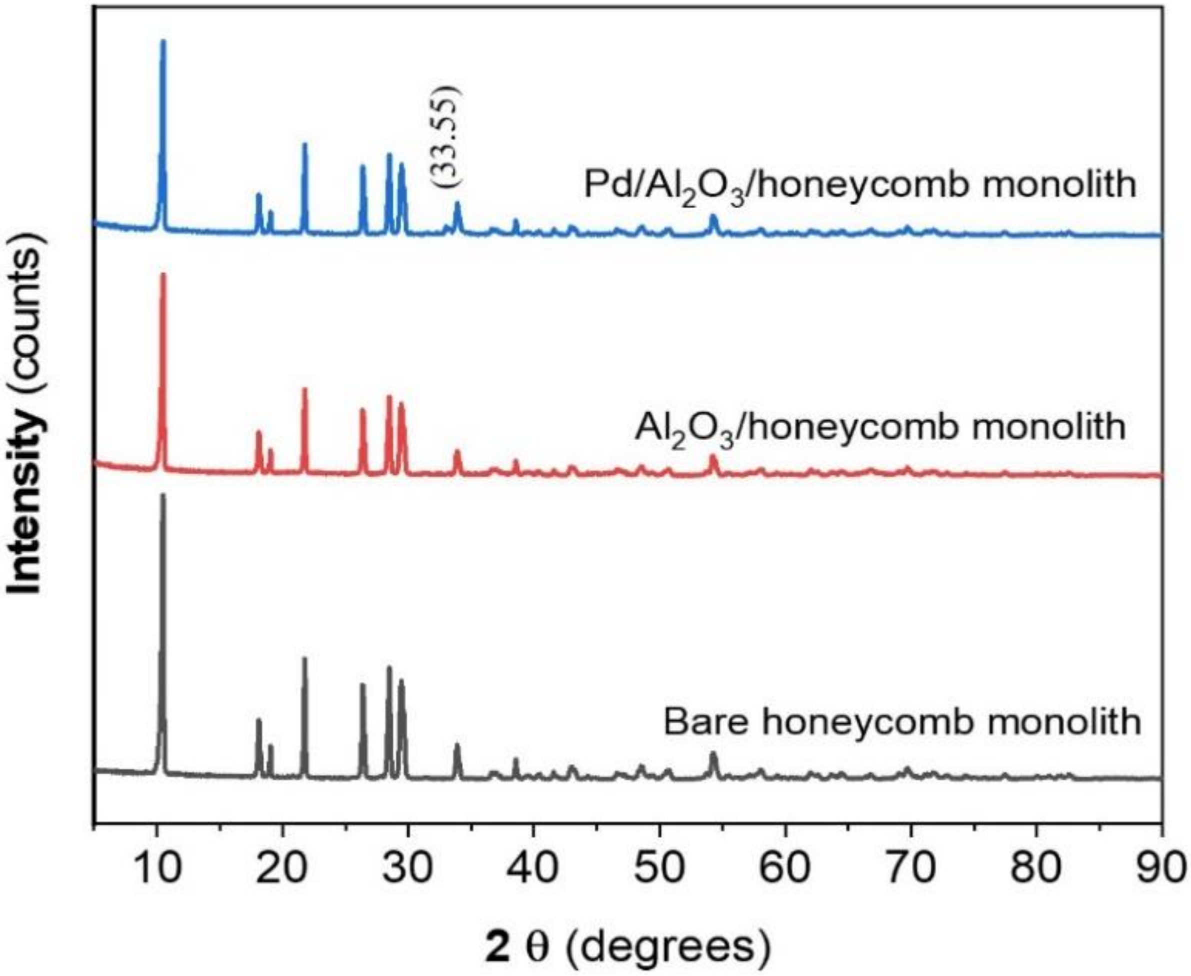

Fig. 5.1. XRD patterns of the bare honeycomb monolith, γ-Al_2O_3/ honeycomb monolith, and Pd/γ-Al_2O_3/honeycomb monolith.

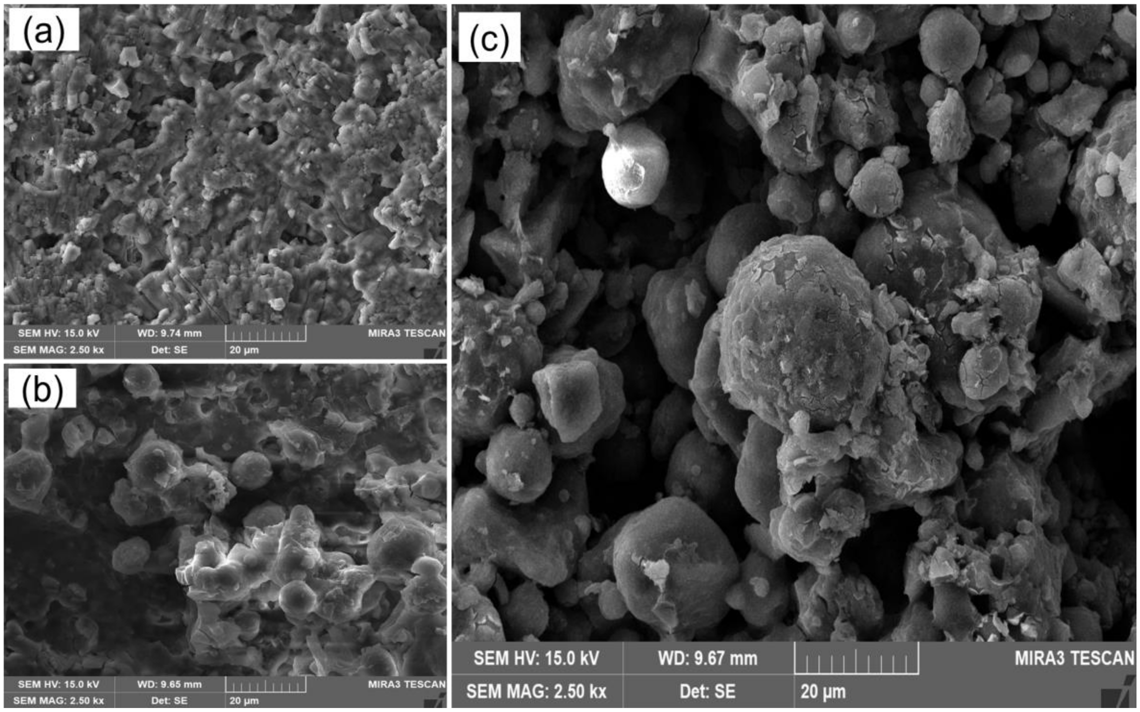

Fig. 5.2. SEM images of (a) the bare honeycomb monolith, (b) ɣ-Al_2O_3/ honeycomb monolith, and (c) Pd/ɣ-Al_2O_3/honeycomb monolith.

SEM analyses were performed to examine the microstructure and surface appearance of the catalyst. Fig. 5.2 presents SEM images of the bare honeycomb monolith, ɣ-Al_2O_3/honeycomb monolith, and Pd/ɣ-Al_2O_3/ honeycomb monolith. Fig. 5.2(b-c) reveals that both alumina oxide and palladium totally covered the surface of the bare monolith. Furthermore, it can be seen in Fig. 5.2c that the PdO particles are well dispersed in the ɣ-Al_2O_3 grains, which is also confirmed by the energy-dispersive X-ray spectroscopy (EDS) elemental mapping images for a selected area of the Pd/ɣ-Al_2O_3/honeycomb catalyst (Fig. 5.3). It can be clearly seen that Al, Si, and Pd exist on the catalyst surface as Al oxide, Si oxide, and Pd oxide, respectively. The high distribution of the PdO would be responsible for the enhanced EA degradation and the surface conductivity of the catalyst.

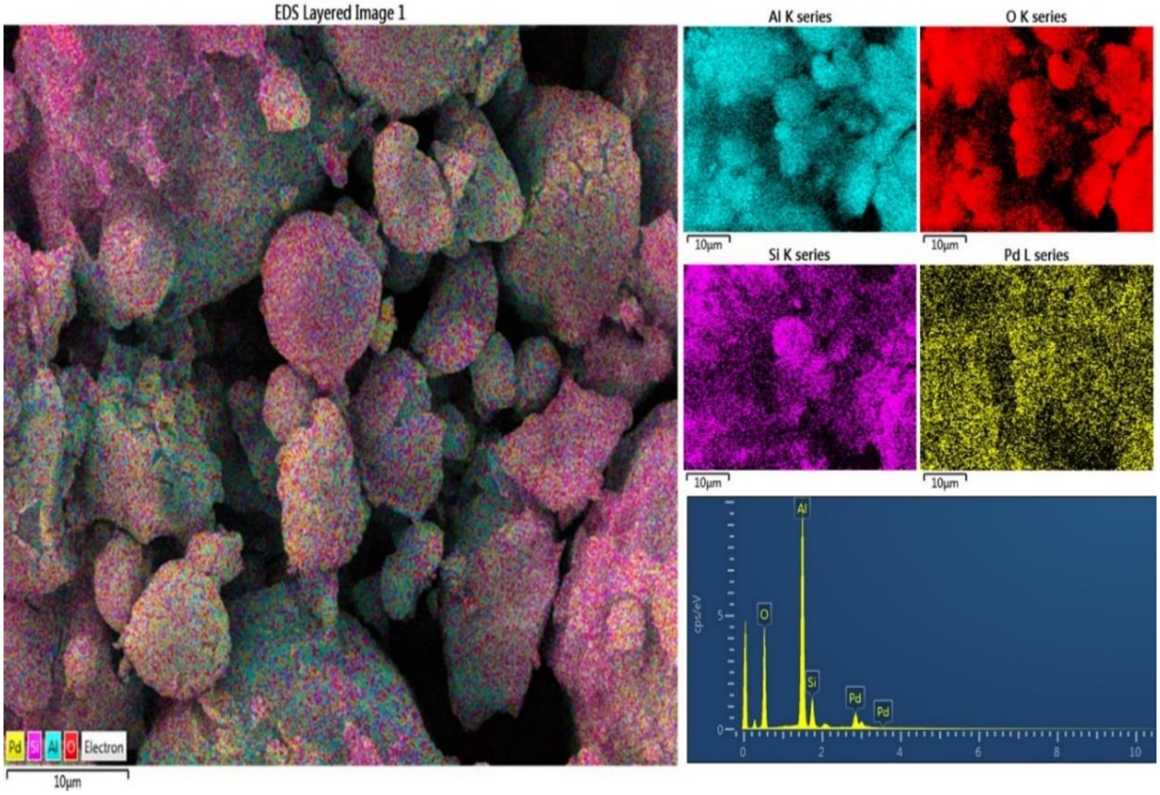

Fig. 5.3. EDS elemental mapping images for a selected area of the Pd/ɣ-Al_2O_3/honeycomb monolith.

5.3.2.Characterization of AC & DC corona plasma within Pd/γ-Al_2O_3/honeycomb catalyst

Characterization of both the AC and DC corona plasma that was uniformly generated within the honeycomb monolith catalyst was achieved under various conditions. Fig. 2.5(b) shows that the plasma discharge was uniformly spread over the holes of the honeycomb monolith containing the catalyst. The image shows that many holes in the honeycomb catalyst glow on both sides of the electrode. This also indicated that most of the channels would be simultaneously filled with plasma. To verify the type of discharge during the process, the typical waveforms of the applied voltage and current of the AC and DC corona discharge were recorded and are shown in Fig. 5.4(a-b).

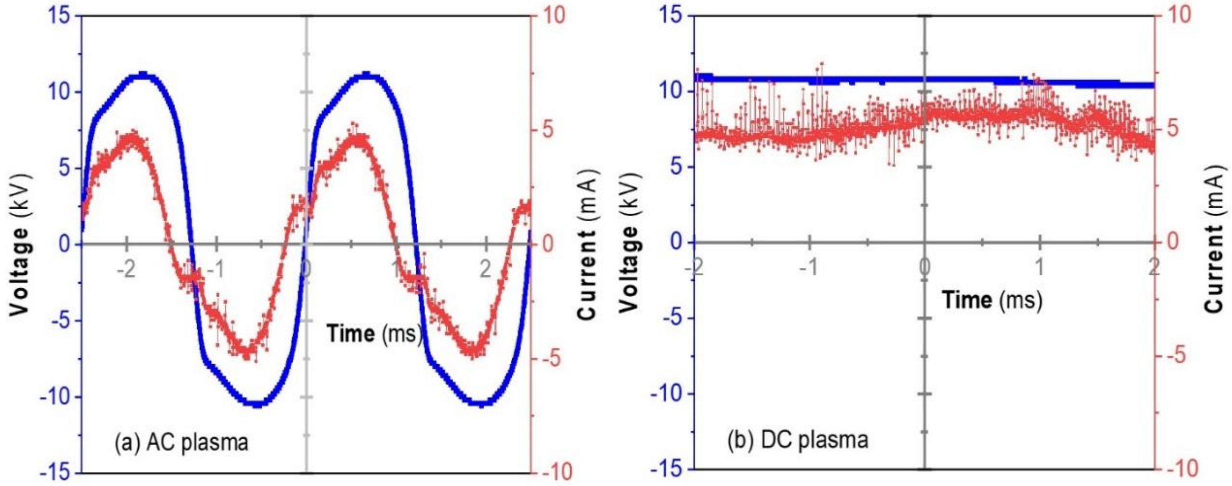

Fig. 5.4. Waveforms of the voltage and current of the corona plasma in the honeycomb obtained: (a) the AC plasma source, and (b) DC plasma source (applied voltage: 11.2 kV, GHSV: 9000 h^{-1}, water vapor: 3%(v/v)).

Obvious differences exist in the shape of the voltage and current waveform between the AC and DC corona discharge at the applied voltage of 11.2 kV. The voltage and discharge current line of the AC discharge are sinusoidal over time, whereas it is always positive in the case of the DC discharge. This determined that DC positive corona discharge would be generated the electric field higher than AC corona discharge. Increasing the electric field would increase the decomposition efficiency of the pollutions [30]. Fig. 5.5 shows the temporal variations in the discharge power and I_{RMS} of the AC and DC corona plasma within the honeycomb catalyst for various levels of water vapor. In the case of the AC corona plasma, the water vapor strongly affected the characteristics of the discharge. Upon closer inspection of the results, the discharge power appeared to sharply decrease with time during the early stage before stabilizing. This can be explained by considering that, initially, the humidified monolith rapidly loses captured water molecules when exposed to the low-humidity feed gas. Apart from this, the discharge power of the AC corona discharge significantly increased as the water vapor in the gas stream increased. For an applied voltage of 11.2 kV to generate the AC corona plasma, a discharge power of 8 W was measured in dry air, whereas the corresponding power is 14 W when approximately 3% of water vapor is present in the gas stream.

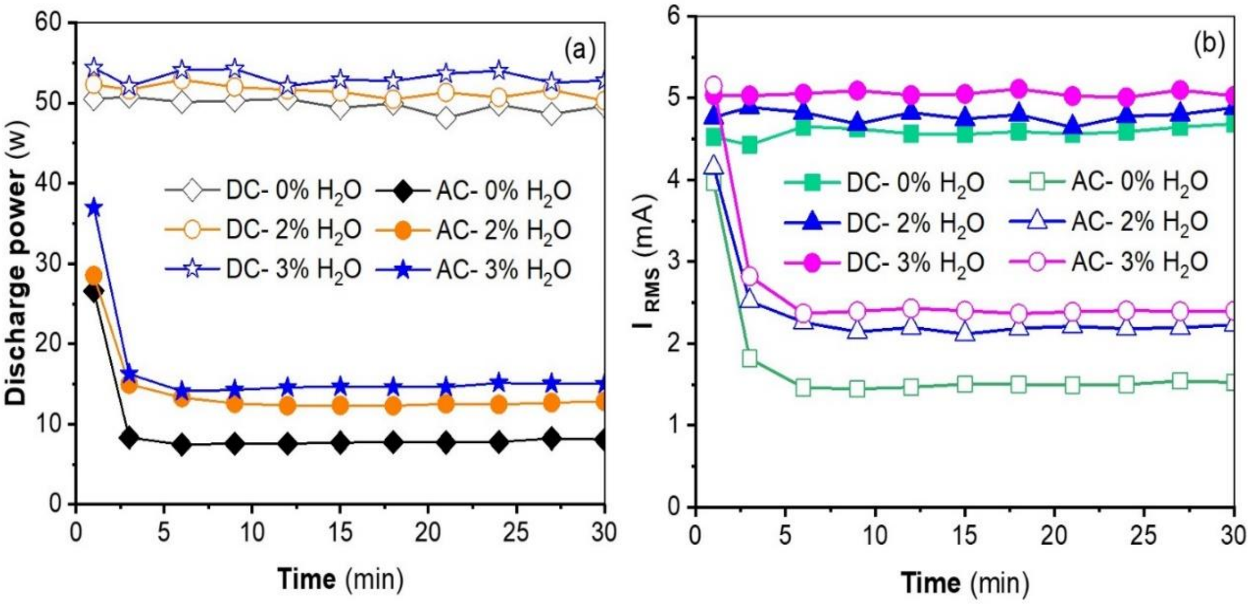

Fig. 5.5. Effect of water vapor content on (a) discharge power, and (b) I_{RMS} for both the AC & DC corona at atmosphere pressure (GHSV: 9000 h^{-1}, applied voltage: 11.2 kV).

The I_{RSM} is another plasma parameter that represents the discharge intensity. Increasing the current density of the micro-discharges creates a stronger micro-discharge in the channels of the honeycomb monolith. In Fig. 5.5(b) the I_{RSM} follows the same tendency by increasing from 1.5 mA to 2.6 mA as the water vapor concentration increases up to 3%. Indeed, water can be absorbed into the cell walls of the honeycomb catalyst and assists the plasma to propagate along the channels of the honeycomb catalyst as a result of increased surface conductivity [38], [44].

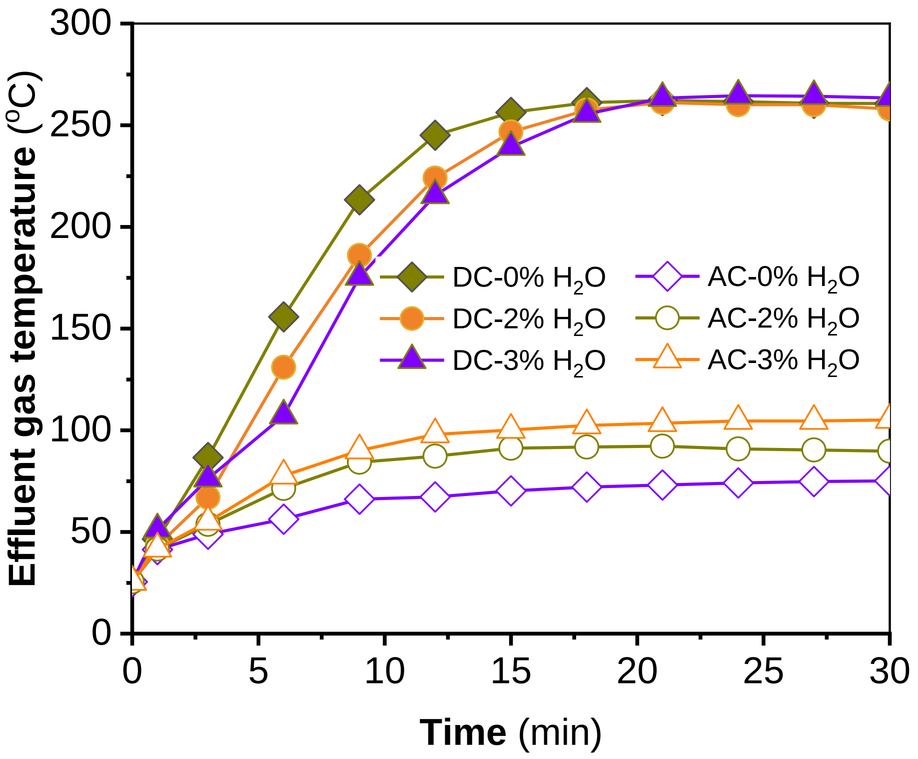

Fig. 5.6. Temporal variations of the effluent gas temperature at different water vapor for both AC & DC corona at atmosphere pressure (GHSV: 9000 h^{-1}, applied voltage: 11.2 kV).

The electrical conductivity of pure water is 0.055 µS/cm at 25 °C and atmospheric pressure [152]. In comparison, the electrical characteristics of the DC discharge are insensitive to variations in the atmospheric conditions. The influence of water on the DC plasma discharge is negligible. As shown in Fig. 5.5(a-b), the discharge power and corona current seem to fluctuate slightly when the water vapor concentration of the feed gas changes. The maximum DC discharge power and I_{RSM} are always much higher than the AC discharge power at the corresponding voltage level. As seen in Fig. 5.6, the effluent gas temperature from the reactor started to increase when a high voltage was applied and reached a steady state after approximately 20 min, during which time the reactor temperature of the AC plasma was much lower than that of the DC plasma.

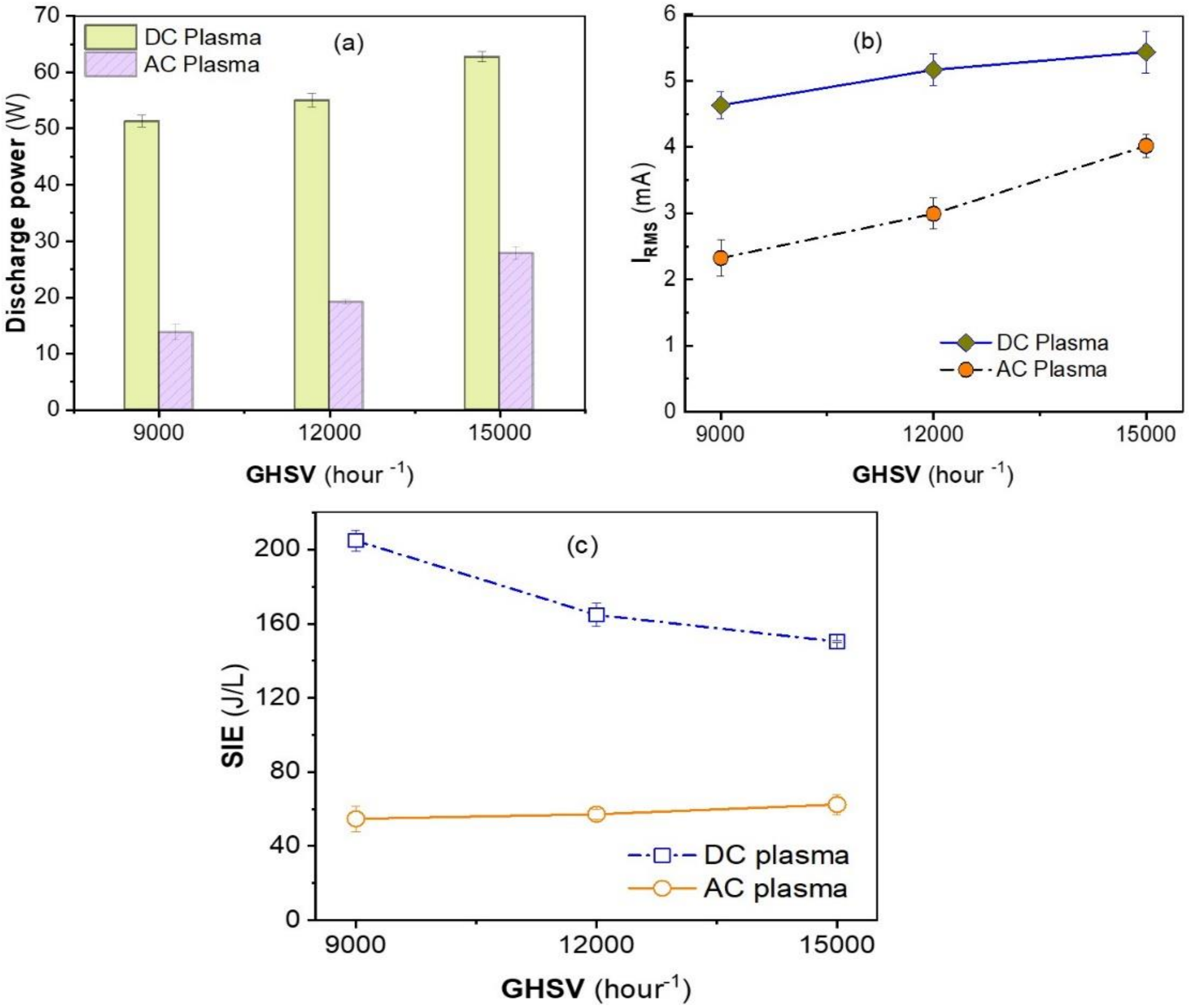

Fig. 5.7 Effect of GHSV on: (a) discharge power, (b) I_{RMS} for both the AC & DC corona plasma, and (c) variation of SIE as a function of GHSV for both the AC & DC corona plasma (humidity: 3%(v/v); applied voltage: 11.2 kV).

This could explain the observation that the discharge power of the DC plasma is higher than that of the AC plasma at the same voltage level. Figure 5.7 (a) shows the effect of the GHSV on the electrical characteristics of the AC and DC corona discharge generated within the honeycomb-supported catalyst at 11.2 kV. The discharge power and I_{RMS} of both the AC and

DC corona discharge significantly depended on the space velocity. An increase in the GHSV leads to an increase in discharge power and I_{RMS}. Specifically, the discharge power of the AC and DC plasma increased remarkably from 14 W to approximately 27 W, and from 52 to 64 W as the GHSV increased from 9,000 to 15,000 h^{-1}, respectively. This behavior can be attributed to the rapid transport of charged particles to the ground electrode when the gas flow rate is high. As shown in Fig. 5.7(b), the discharge current increases with increasing the GHSV. The variation of SIE as a function of GHSV is shown in Fig 5.7(c).

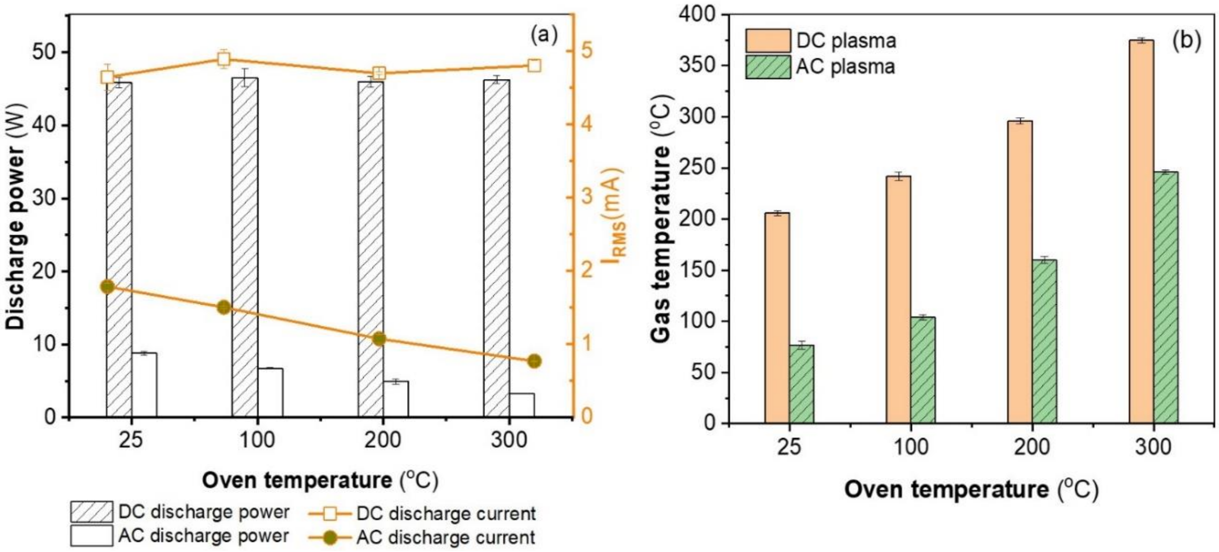

Fig. 5.8. Effect of temperature on the discharge power and current characteristic for both the AC & DC corona discharge; (b) variation effluent gas temperature of both AC & DC honeycomb discharge as a function of oven temperature (GHSV: 9000 h^{-1}, humidity: 3%(v/v); applied voltage: 10 kV).

To investigate the effect of the temperature on the discharge characteristics for both AC and DC corona discharge combined with honeycomb catalyst, the reactor was placed in an electric furnace that was controlled in the range of 25–300 °C. Figure 5.8 (a) indicates the dependence of the electrical characteristics of the plasma on the temperature. The results show that the discharge power and current measurement of the AC corona discharge strongly depend on the operating temperature. Specifically, the discharge power decreased markedly from 9 to 3 W as the oven temperature increased from 25 to 300 °C at the applied voltage of 10 kV. As discussed above, the AC discharge is sensitive to humidity, which means that the adsorption of water molecules plays an important role in the propagation of plasma. The adsorption of water molecules decreases as the temperature increases, which can interpret the decreased discharge power with increasing the temperature. Interestingly, the DC discharge is insensitive to temperature variations. In fact, the discharge power and current of the DC plasma only vary slightly across different temperatures at the same applied voltage of 10 kV. As mentioned above, the effect of H_2O on the DC corona discharge is negligible, indicating that the decrease in the adsorption of water molecules at high temperatures does not affect the discharge. Fig. 5.8(b) shows the variation effluent gas temperature as a function of the oven temperature. As result, the effluent gas temperature of the honeycomb AC plasma reactor is lower than that of the oven temperature when the oven temperature is obtained 200 °C. It may be due to the decrease in plasma intensity caused by the AC corona discharge as the reactor temperature increase. Meanwhile, the effluent gas temperature of the honeycomb DC corona reactor is always higher than that of the set temperature of the electric furnace. This reaffirms that the plasma is maintained even at temperatures over 200 °C. Maintaining the discharge plasma during temperature changes is very important for automobile exhaust treatment or other environmental applications.

Take all into account, DC corona discharge is more easily created by virtue of a high electrical field by using a DC power supply; it means that DC corona discharge can be created at much lower applied voltage compared to AC corona discharge. In addition, the DC corona discharge can be stably operated, less dependent on operating conditions such as humility, gas temperature, and GHSV. This point is very important for real applications because the real operating conditions (i.e., humidity and exhaust gas temperature) are usually changing.

5.3.3. Analysis of optical emission spectra

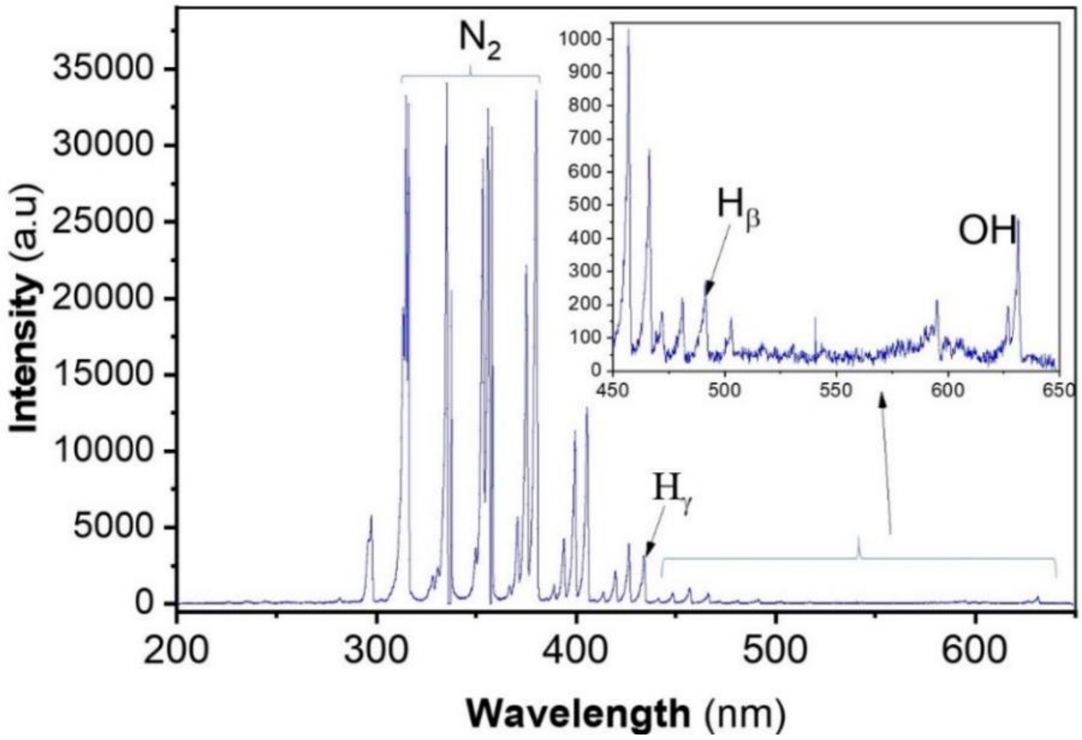

Fig. 5.9. Optical emission spectra of the corona discharge plasma in air (GHSV: 9000 h^{-1}, humidity: 3%(v/v); applied voltage: 11.2 kV).

Active species such as OH, H, O, N_2, and high-energy electrons are formed in the air plasma as a result of the collision between highly energetic electrons and the dominant air molecules [34]. Figure 5.9 shows the optical emission spectrum of the corona discharge in the air atmosphere. The composition of the gas mixture includes the EA of which the concentration is diluted by the air stream with GHSV of 9000 h^{-1} and approximately 3% H_2O. As shown in

Fig. 5.9, various emission peaks related to excited N_2, NO, and OH were detected in the spectral range 200–650 nm [44], [153], [154]. The emission peak in the range of 621- 627 nm confirms the formation of OH radicals [154], [155]. These radicals are strongly oxidative species and could promote the oxidation of EA. The peaks related to the atomic hydrogen are located at H_β (486.5 nm) and H_γ (433.5 nm) [154], [156]. The emission bands in the range of 323–410 nm are attributed to the excited N_2 [44], [153].

5.3.4. Evaluation of the EA removal efficiency of the AC and DC corona discharge by the Pd/γ-Al_2O_3/honeycomb catalyst

1. Effect of humidity

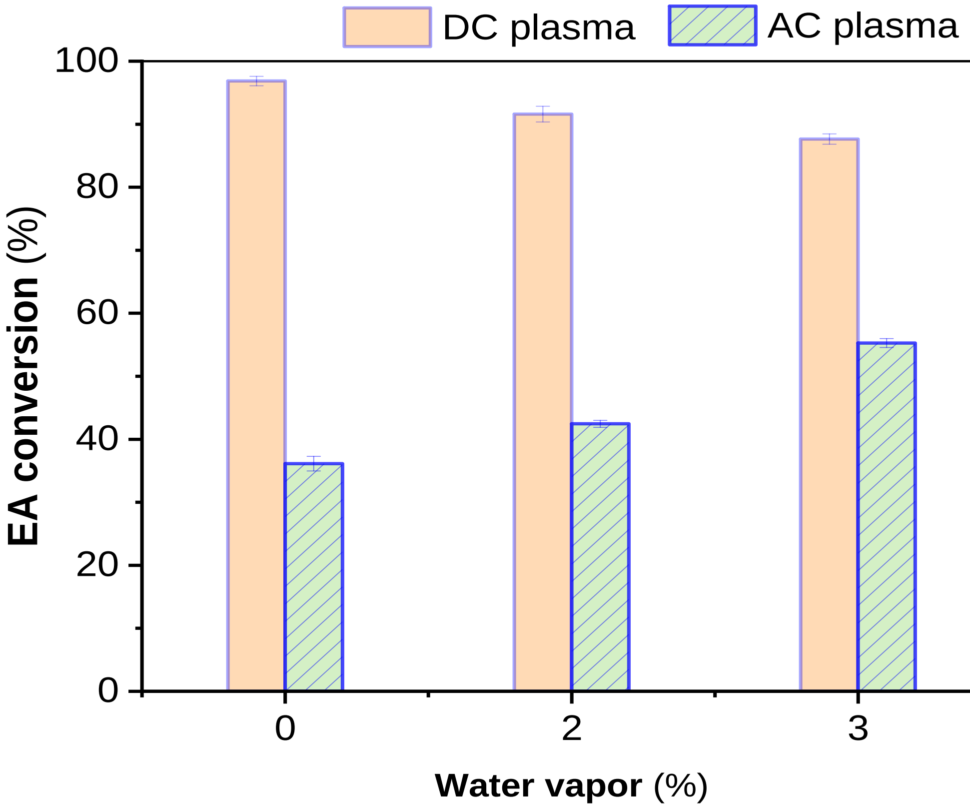

Fig. 5.10. The conversion efficiency of EA by both AC & DC corona for various water vapor contents in the gas stream (GHSV: 9000 h^{-1}, applied voltage: 11.2 kV).

Different environments have variable humidity levels. Thus, the effect of humidity is indeed of great interest because, in practice, processes are carried out in ambient air. Figure 5.10 shows the EA removal efficiency as a function of the amount of water vapor. The results indicate that the DC corona discharge is always more effective than the AC corona discharge. As the water vapor increases from 0 to 3 %, the removal efficiency of the DC corona discharge tends to decrease slightly. The dissociation adsorption of water by the high-energy electron in the plasma zone leads to the formation of additional surface hydroxyls that will neutralize the acid sites and thus decrease the catalytic activity [157]. Further, the discharge power of the DC corona was hardly affected by the humidity, as shown above. The slight decrease in the EA removal efficiency at higher humidity can be explained by the scavenging of ozone by OH radicals produced from H_2O. In contrast, the AC corona discharge realizes a slight increase in efficiency at higher water vapor content. As mentioned above, the discharge power of the AC corona improved significantly as the water vapor content of the feed gas increased, thereby enhancing the EA removal efficiency. In other words, the effect of discharge power increase was more dominant than the ozone scavenging effect of the OH radical.

2. Effect of GHSV

Figure 5.11 shows the effect of the feed gas flow rate or GHSV on the EA removal efficiency. A GHSV of 9,000 to 15,000 h^{-1} corresponds to a residence time of 0.392 to 0.235 s. The EA conversion efficiency decreases markedly for both the AC and DC discharge plasma with increasing GHSV. It is worth noting that the EA removal efficiency drops significantly from 64% to approximately 20% in the AC discharge plasma, whereas it only decreases slightly from 88% to 78% in the DC discharge plasma at 11.2 kV of applied voltage with 3% water vapor in the feed gas. Obviously, the higher the gas velocity, the shorter the reaction time of the EA molecules in the plasma region due to the decrease of contact times between the catalysts, reactive species, and reactant molecules. Moreover, the SIE value decreases with increasing GHSV, i.e., the power input relative to the gas flow rate decreases, which is the reason for the decreased EA removal efficiency at higher GHSV.

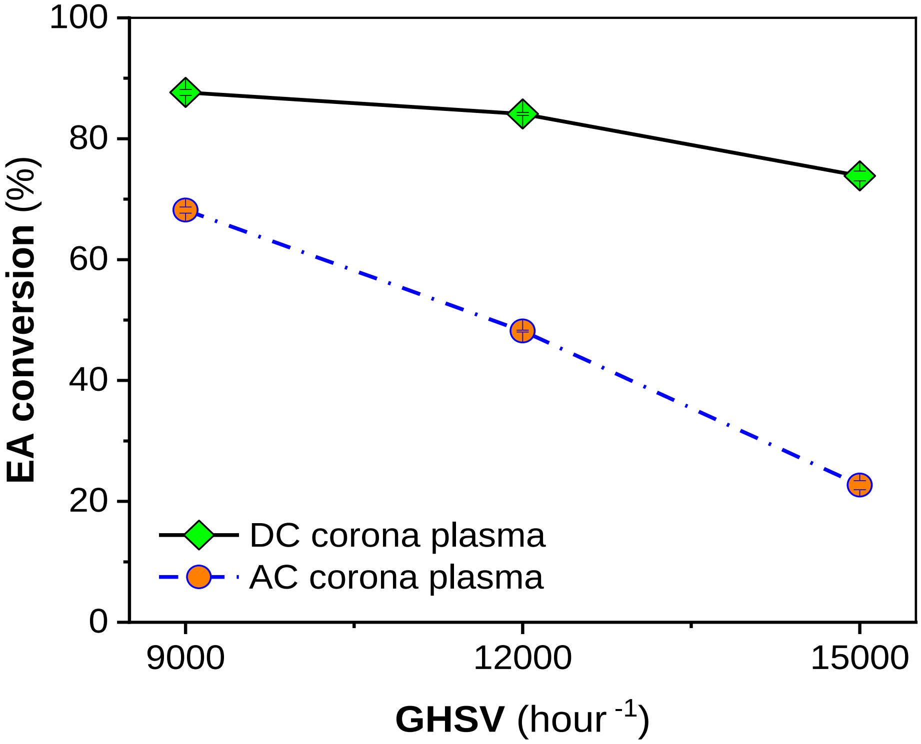

Fig. 5.11. Conversion efficiency of EA by both AC & DC corona for different GHSV values (applied voltage: 11.2 kV, water vapor content: 3%(v/v)).

3. Effect of SIE

Figure 5.12(a) presents the relationship between the removal efficiency and treatment time at different SIE values of the DC discharge. The removal efficiency changes slightly with time and is maintained at approximately 96% at 220 J/L. For an SIE of 100 and 160 J/L, the EA removal efficiency increased with time in the first 15 min and then leveled off. Observation of the results shows that EA removal efficiency increased with increasing SIE. The enhanced EA removal effect may be the result of the participation of more active species and high-energy electrons in the destruction of EA with higher SIE. The increase in the SIE as the applied voltage increases is known to strengthen the electron energy and the electric field to form more active species in the plasma region [34], [158]. Furthermore, the temperature of the gas increased with time and stabilized after a certain period of reaction time. Generally, the catalyst exhibits higher activity at a higher temperature, which explains the increase in the EA removal in the early stage.

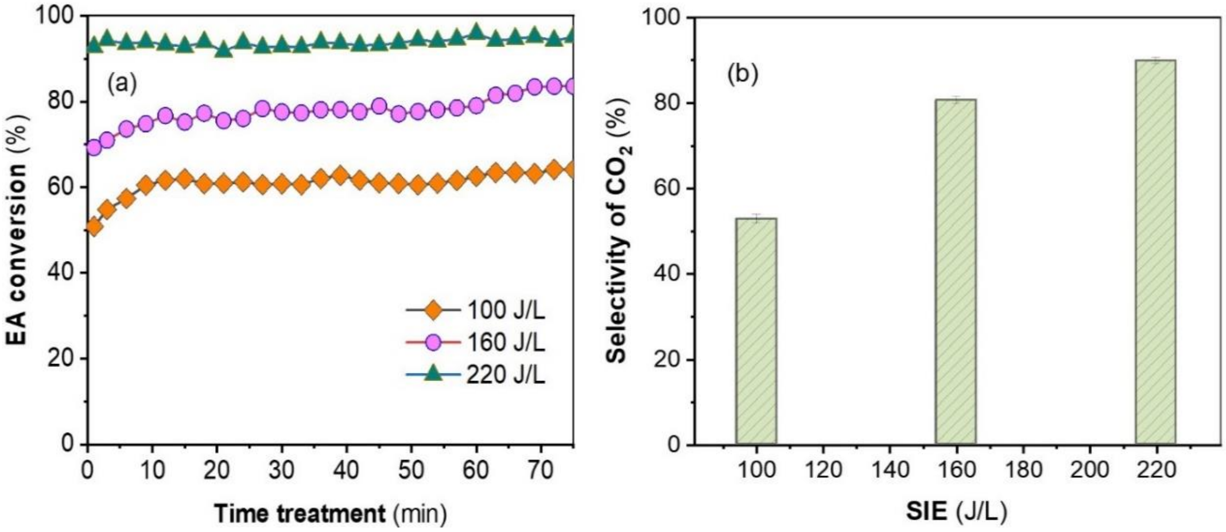

Fig. 5.12. (a) Temporal variations of the plasma–catalytic EA removal effciency at diferent SIE values, and (b) the steady-state CO_2 selectivities (GHSV: 9000 h^{-1}, water vapor: 3%(v/v)).

The CO_2 selectivity is an important indicator with which to evaluate the oxidation performance towards EA degradation. Fig. 5.12(b) shows the CO_2 selectivity for various SIE levels of the DC discharge plasma. These results show that the CO_2 selectivity is worse for low

SIE. This is because the EA is not completely mineralized and because hydrocarbon intermediate byproducts are present at low SIE. Increased energy density leads to enhanced CO_2 selectivity. An increase in the SIE from 100 to 220 J/L is accompanied by an increase in the CO_2 selectivity from 52% to approximately 89.8%.

5.3.5. A comparison of ethyl acetate removal between honeycomb corona discharge and other processes

Table 2 presents published papers regarding ethyl-acetate with different plasma-catalyst systems. As can be seen from this table, almost all previous study are used a DBD reactor configuration filled with catalysts (i.e., pellets or powder) for the decomposition of EA.

Table 2. Comparison between different plasma configurations for ethyl-acetate removal process under atmospheric pressure condition.

Reactor type	**Packing materials**	**Flow rate (L/min)**	**GHSV (hour^{-1})**	**$C_4H_8O_2$ -inlet (ppm)**	**SIE (J/L) /applied voltage (kV)**	**η (%)**	**EE (gkW^{-1} h^{-1})**	**Ref**
DBD	$LaCoO_3$	1	42441	100	595.9 J/L	98.8	2.15	[159]
DBD	-	7	2210	400	9 kV	72.6	-	[160]
DBD	$La_{0.8}Ce_{0.2}MnO_3$	1	2827	100	495.9 J/L	94.2	2.46	[149]
DBD	$La_{1-x}Ce_xCoO_{3+\delta}$	1	26525	100	558 J/L	100	1.162	[9]
DBD	Bi_2MoO_6-MnO_2	3	23386	200	392 J/L	100	6.62	[161]
DDBD	-	1	4074	8	1158 J/L	96.4	0.086	[150]
HCD	$Pd/\gamma Al_2O_3$-honeycomb	15	9000	30	220 J/L	96	1.7	This work

HCD: honeycomb corona discharge; SIE: specific input energy; η: removal efficiency; EE: energy efficiency; GHSV was calculated as the airflow rate divided by the catalyst volume.

As mentioned before, although a DBD reactor can produce a stable and effective plasma discharge and provide high removal performance; however, this configuration is difficult to be commercialized or scaled up [44], [144]. Furthermore, the packed-bed DBD reactor needs to be bundled to process a large flow rate of contaminated gas, and the high-pressure drop across the catalyst bed also causes the operating cost to increase. This work has used the honeycomb corona discharge (HCD) reactor configuration. An attempt has been made to successfully generated a large volume of stable and homogenous plasma at atmospheric pressure in the channels of the honeycomb catalyst (Fig.2.5(b)). In comparison between this work and other plasma-catalyst reactor configurations, the EA removal efficiency is obtained high with lower energy density for the HCD reactor configuration. The table indicated that the energy efficiency of the HCD reactor was supperless than that of other processes. The lower required energy density of the honeycomb corona discharge reactor can be explained by the high feed gas through the honeycomb catalyst reactor. Our work has proven that HCD not only has high efficiency in removing EA but also has great potential for practical application.

5.3.6. Analysis of byproduct

Ozone is one of the main oxidative species generated by air corona plasma, which can contributed to heterogeneous oxidation reactions on the catalyst surface and enhances the catalytic activity [50,51]. Figure 5.13(a-b) shows the ozone concentration of both the AC and DC plasma for various parameters such as the relative humidity and the GHSV at SIE of 220 J/L, measured 25 min after the plasma reaction started. Although the energy density in the DC plasma reactor is much higher than that in the AC plasma reactor, the amount of ozone that is generated does not differ much between the two types of plasma sources. As described in relation to Fig. 5.6, the gas temperature of the DC discharge is much higher than that of the AC

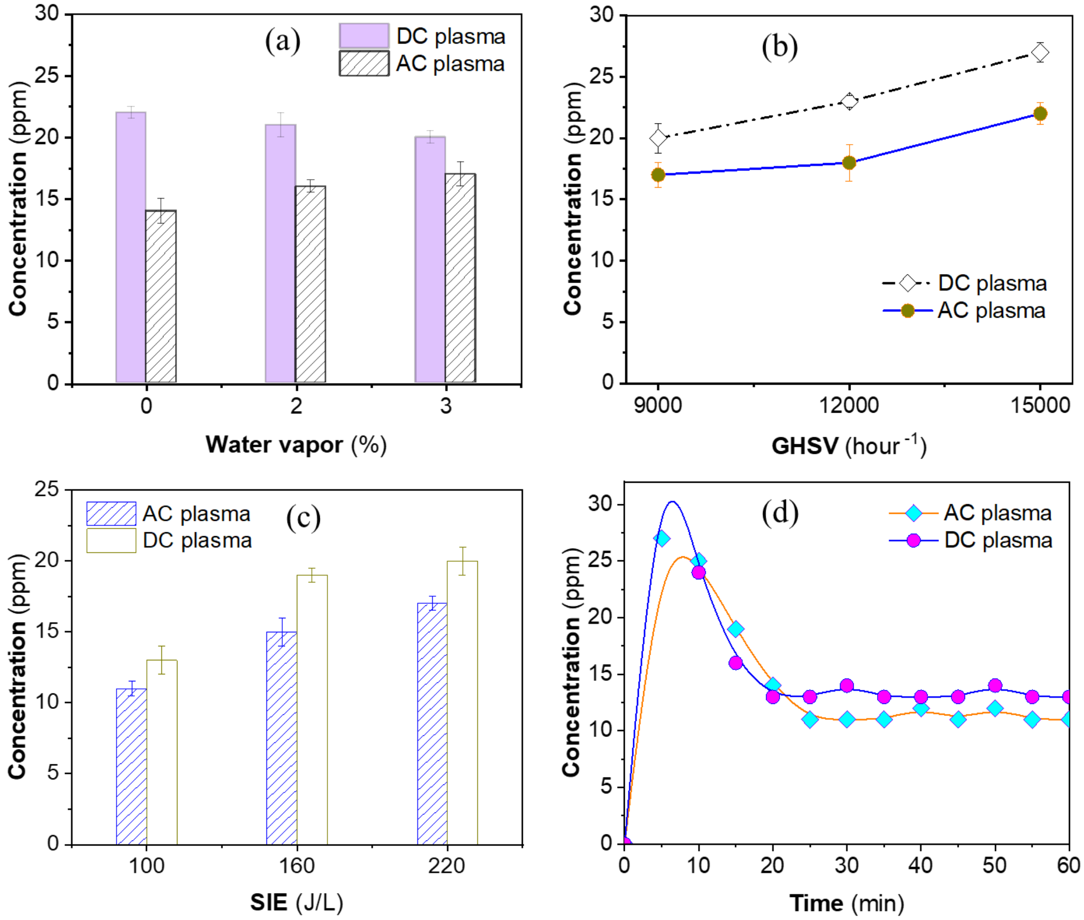

Fig. 5.13. Ozone concentration generated by both AC and DC plasma as a function of; (a) the effect of humidity (SIE: 220 J/L, GHSV: 9000 h^{-1}); (b) the effect of GHSV (SIE: 220 J/L, water vapor: 3%(v/v), (c) the effect of SIE (GHSV: 9000 h^{-1}, water vapor: 3%(v/v), and (d) the temporal variations of the ozone concentration during the operation at 100 J/L.

discharge, which could explain the decrease in the O_3 concentration. Note that the decomposition of ozone strongly depends on the temperature [14]. In addition, ozone could also gain access to the pores in the catalyst and then dissociate into atomic oxygen species which would react with the EA molecules, resulting in decreased ozone levels [52]. Fig. 5.13(a) shows that the ozone concentration decreases with increasing water vapor in the feed gas in the case of

DC plasma. Indeed, the water vapor could inhibit ozone generation. However, contrary thereto, the ozone concentration increases slightly in spite of increasing water vapor in the AC plasma. This result is because the discharge power increases were more dominant than the inhibition of ozone generation by water. The dependence of the O_3 concentration on the GHSV is indicated in Fig. 5.13(b), which shows that the ozone concentration increases with increasing GHSV for both types of plasma sources. These results maybe this is due to an increase in the inlet O_2 due to the increase of flow rate. In addition, a possible reason for this observation is that the residence time of the feed gas was not sufficient to consume ozone through the reactions with EA and its byproducts. The results in Fig. 5.13(c) shows that the ozone concentration increased with SIE for both the AC and DC plasma. The increase in the SIE promotes the generation of energetic electrons in the plasma region, leading to an increase in the collisions between them and oxygen molecules, increasing the concentration of ozone. The temporal variations of the ozone concentration at the reactor outlet obtained at 100 J/L is shown in Fig. 5.13d. The concentration of ozone sharply increased in the early state (10 min) and then decreased and reached the steady state. The gas temperature started to increase when the plasma was turned on (Fig. 5.6). In the early stage, the reactor temperature was low, which can explain the sharp increase in the ozone concentration.

The mechanisms whereby EA oxidation takes place may be understood and elucidated by identifying the byproducts. Figure 5.14 shows the infrared spectra of the gas phase products generated in the DC plasma in the honeycomb structure containing the catalyst when processing dilute EA in air. The time evolution of the FTIR absorption spectra was monitored in the wavenumber range from 1000 cm^{-1} to 4000 cm^{-1}. The results show that the spectrum consists of many different emission peaks. The EA absorption bands at 1048, 1244, 1376, 1762, and 2992 cm^{-1} showed a significant decrease after the plasma treatment. The emission peak that appears at 2355 cm^{-1} is confirmed to be CO_2, which intensified as the applied voltage increased, indicating that the complete oxidation of EA strongly improved.

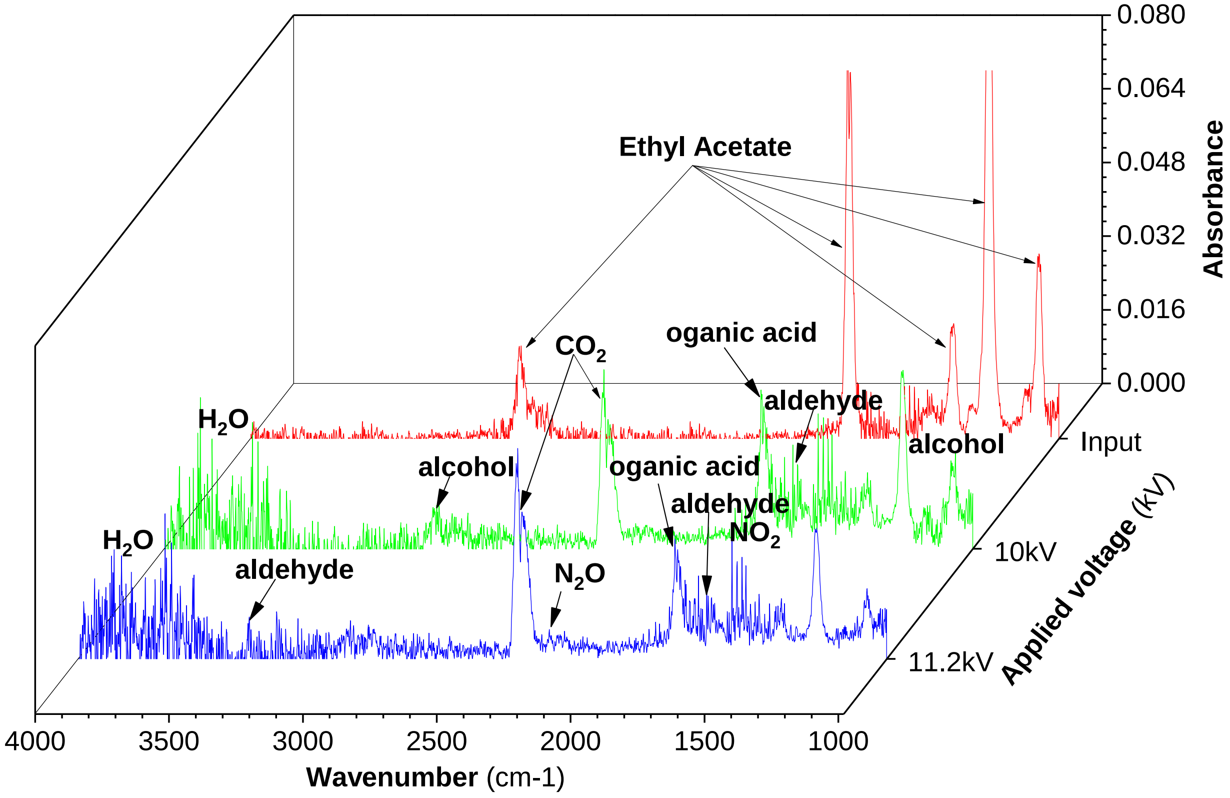

Fig. 5.14. FTIR spectra of the effluent gas produced by DC corona discharge by varying the applied voltage (inlet concentration: 300 ppm, dry air, GHSV: 9000h^{-1}).

In the plasma zone, the collision between energetic electrons and the EA molecules in the carrier gases (N_2 and O_2) forms a variety of reactive species and intermediate byproducts. The radicals, electrons, and excited molecules can react with chemical bonds such as C–H, C=O, and C–C. The mean energy of the energetic electrons was shown to be 1−10 eV [164]. The bond dissociation energies of C–H, C–C, and C=O are 4.3 eV, 3.44 eV, and 7.55 eV, respectively, which are larger than the dissociation energy of the C–O bonds (3.38 eV) [165]. Therefore, the C−O bond can easily be destroyed by energetic electrons and reactive species to generate methyl

(CH_3), acetate (CH_3COO), and acetyl (CH_3CO) groups [9], [166], [167]. Afterward, the fragments from EA can further react with oxidative species such as O, O_3, and OH radicals to form methyl (CH_3). The partial oxidations of the fragments by O atom and OH radical can explain the formation of some intermediates byproducts such as HCHO, HCOOH, or CH_3OH [9]. Besides, the plasma-assisted catalyst surface reaction also contributes to the oxidation of EA. The catalyst plays an important role in determining the reaction performance of the plasma-catalytic for the EA removal process and plasma-catalytic chemical reaction [149]. A previous study reported that the oxidation process of EA base an alumina catalyst can produce the byproducts such as ethanol, acetic acid, and aldehyde [167]. Moreover, the catalyst with adsorption capability can prolong the retention of the reactants, leading to higher reaction probability [36]. The coated catalytic layer improved the catalytic performance, creating more catalyst active sites, where reactions could take place on those sites [168]. Both EA and intermediates from the gas phase reactions can be adsorbed onto the surface of the catalyst [9]. Furthermore, ozone adsorption to the catalyst surface and its subsequent dissociation into reactive atomic oxygen species are an important step in the heterogeneous destruction of VOC [169].

In this study, the Pd/γ-Al_2O_3 honeycomb catalyst was placed in the discharge zone and directly in contact with the plasma. Chemical reactions are improved due to a large volume of uniform plasma successfully generated inside honeycomb catalysts without pressure drop [140]. Herein, there will be plasma gas-phase reactions and plasma-assisted catalytic surface reactions. The reactive species can be generated inside pores of structured catalysts (in the µm range), on the surface of the catalyst, and at the interface between the gas phase and the catalyst surface [69], [170]. The diffusion of the short-lived reactive species (i.e., O atom, OH radicals) onto the

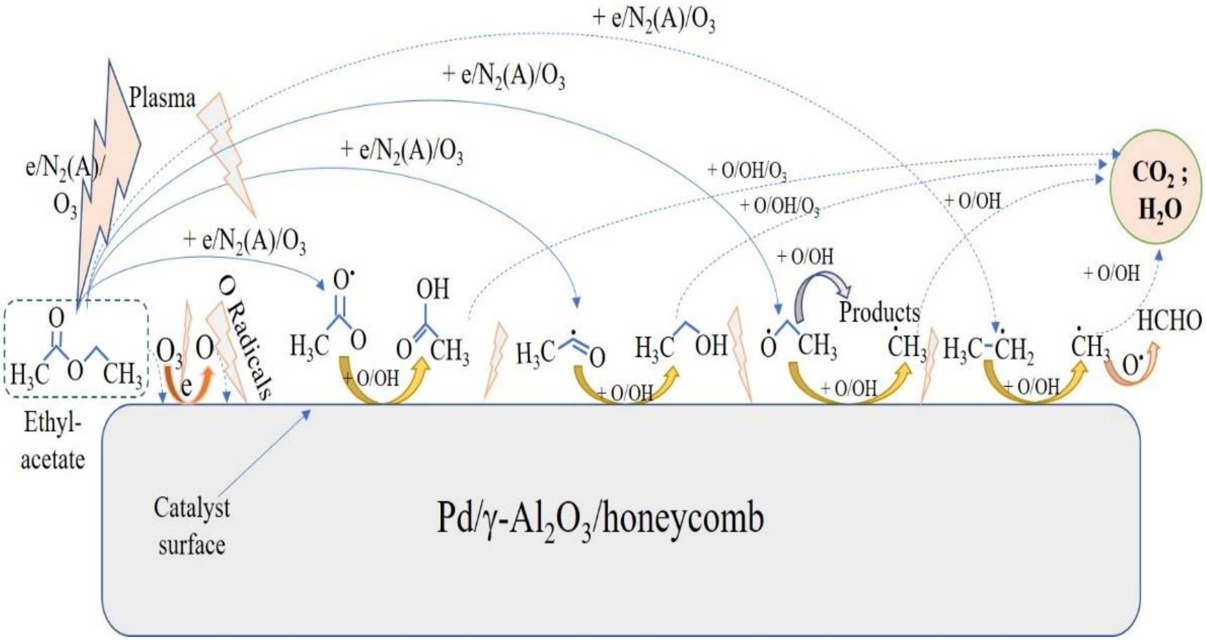

Fig. 5.15. The plausible reaction mechanism in the plasma-assisted surface oxidation of EA

micro-pore of the catalyst surface will participate in the surface reactions with EA and intermediates byproducts [9], [69]. The simultaneous homogeneous and heterogeneous reactions efficiently decompose the EA molecules. The main gaseous products from the plasma-catalytic reaction were CO_x and H_2O, while minor products were observed. As shown in Fig. 5.14, minor intermediate byproducts may include ethanol, aldehydes, and acetic acid. The reaction proceeds by a series of oxidation steps that involve O atom and OH radical attack, finally leading to the formation of CO_2 and H_2O. A plausible reaction mechanism was proposed where removal of EA mainly proceeds on the surface of catalysts (Fig. 5.15). Regarding the decomposition of EA, numerous reactions can be involved. The reactions related to the production of reactive species and inorganic byproducts are presented in Table 3. The reactions responsible for the decomposition of EA are summarized in Table 4, which are taken from the NIST Chemical Kinetics Database at 298 K [171].

Table 3. Reactions leading to the formation of reactive species and inorganic byproducts

Reaction	**Rate constant at 298 K** (**cm^3s^{-1} or cm^6s^{-1}**)	
$N_2 + e \rightarrow N(4S) + N(4S, 2D) + e$	9.79 eV/bond	(R7)
$O_2 + e \rightarrow O(3P) + O(3P, 1D) + e$	5.15 eV/bond	(R8)
$\bullet O + O_2 + M \rightarrow O_3 + M$	$k=6.01 \times 10^{-34}$	(R9)
$O_3 + O_2 \rightarrow \bullet O + O_2 + O_2$	$k=2.04 \times 10^{-27}$	(R10)
$H_2O + e \rightarrow \bullet OH + H\bullet + e$	4.46 eV/bond	(R11)
$N(2D) + O_2 \rightarrow NO + O\bullet$	$k=4.21 \times 10^{-12}$	(R12)
$N_2 + O\bullet \rightarrow NO + N$	$k=1.31 \times 10^{-11}$	(R13)
$NO + N \rightarrow N_2 + O\bullet$	$k=2.93 \times 10^{-11}$	(R14)
$NO + O\bullet + M \rightarrow NO_2 + M$	$k=9.02 \times 10^{-32}$	(R15)
$O\bullet + N_2 + M \rightarrow N_2O + M$	$k=5.02 \times 10^{-38}$	(R16)

M stands for three-body reaction partner, e stands for energetic electron, and N(4S) and N(4S, 2D) are ground-state and a metastable excited-state nitrogen atom, and O(3P) and O(3P, 1D) denotes for ground-state and a metastable excited-state oxygen atom, respectively.

Table 4. Possible reactions for the oxidative decomposition of ethyl acetate

Reaction	**Rate constant at 298 K** (**cm^3s^{-1} or cm^6s^{-1}**)	
$CH_3COOC_2H_5 + e/M \rightarrow CH_3CO\bullet + CH_3CH_2O\bullet + e/M$	7.55 eV/bond	(R17)
$CH_3COOC_2H_5 + e/M \rightarrow CH_3CH_2\bullet + CH_3COO\bullet + e/M$	4.3 eV/bond	(R18)
$CH_3COOC_2H_5 + e/M \rightarrow CH_3\bullet + CH_2CH_3COO\bullet + e/M$	4.3 eV/bond	(R19)
$CH_3COOC_2H_5 + O\bullet \rightarrow CH_3CH(\bullet)C(O)OCH_2 + \bullet OH$	$k=3.86 \times 10^{-16}$	(R20)
$CH_3COOC_2H_5 + \bullet OH \rightarrow$ Products	$k=1.1\times 10^{-10}$	(R21)
$\bullet CH_3CO + O\bullet \rightarrow CO_2 + \bullet CH_3$	$k=1.6 \times 10^{-11}$	(R22)

$\bullet CH_3CO + \bullet OH \rightarrow CH_2CO\bullet + H_2O$	$k=2.0 \times 10^{-11}$	(R23)
$CH_3CH_2\bullet + O\bullet \rightarrow HCHO + \bullet CH_3$	$k=2.67 \times 10^{-11}$	(R24)
$CH_3CH_2\bullet + O\bullet \rightarrow CH_3CH_2O\bullet$	$k=1.23\times 10^{-10}$	(R25)
$CH_3CH_2O\bullet + O\bullet \rightarrow HCOOH + \bullet CH_3$	$k=3.89 \times 10^{-10}$	(R26)
$HCOOH + \bullet OH \rightarrow$ Products	$k=4.5 \times 10^{-13}$	(R27)
$\bullet CH_3 + O\bullet \rightarrow CH_2O\bullet + H\bullet$	$k=9.4 \times 10^{-11}$	(R28)
$\bullet CH_3 + \bullet OH + M \rightarrow CH_3OH + M$	$k=2.25 \times 10^{-24}$	(R29)
$\bullet CH_3 + \bullet OH \rightarrow HCHO + H_2$	$k=9.1 \times 10^{-11}$	(R30)
$CH_3OH + OH \rightarrow \bullet CH_2OH + H_2O$	$k=8.8 \times 10^{-13}$	(R31)
$\bullet CH_2OH + O \rightarrow HCHO + OH$	$k=7.01 \times 10^{-11}$	(R32)
$\bullet CH_2OH + OH \rightarrow HCHO + H_2O$	$k=4 \times 10^{-11}$	(R33)
$CH_3OH + \bullet OH \rightarrow HCHO + H_2O + H\bullet$	$k=1.1 \times 10^{-12}$	(R34)
$CH_3OH + \bullet OH \rightarrow CH_3O + H_2O$	$k=9.45 \times 10^{-13}$	(R35)
$HCHO + \bullet OH \rightarrow HCOOH + H\bullet$	$k=2.01 \times 10^{-13}$	(R36)
$HCHO + \bullet OH \rightarrow CO_2 + H_2 + H\bullet$	$k=1.79 \times 10^{-11}$	(R37)
$HCHO + O\bullet \rightarrow HCO\bullet + OH$	$k=1.67 \times 10^{-13}$	(R38)
$HCHO + O\bullet \rightarrow CO + \bullet OH + H\bullet$	$k=1.0 \times 10^{-10}$	(R39)

5.4. Summary

The discussion of this work based on corona discharge produced by alternating current (AC) and direct current (DC) over a Pd/ ɣ-Al_2O_3 catalyst supported on a honeycomb structure monolith was developed to eliminate ethyl acetate (EA) in the air at atmospheric pressure. The characteristics of the AC and DC corona discharge generated inside the honeycomb structure monolith were investigated by varying the humidity, gas hourly space velocity (GHSV), and temperature. The results showed that the DC corona discharge is more stable and easily operated at different operating conditions such as humility, GHSV, and gas temperature compared to the AC discharge. At a given applied voltage, the EA conversion in the DC honeycomb catalyst discharge is, therefore, higher compared with that in the AC honeycomb catalyst discharge (e.g., 96% of EA conversion compared with approximately 68%, respectively, at 11.2 kV). These new results can open opportunities for wide applications of DC corona discharge combined with catalysts for VOC treatment in real-time. Additionally, we revealed new possible reaction pathways of plasma VOC oxidation reaction through investigating the byproducts in the process.

CHAPTER 6

CONCLUSIONS

The performance of plasma catalytic reactor for removal NO_x & soot at low temperature and VOC decomposition in the air at atmospheric pressure was demonstrated in this dissertation. The main conclusions of this work were made as follows.

1. The first research has evaluated low-temperature and fluctuating temperature conditions for NO_x removal over Ag/ZSM5 and Cu/ZSM5 catalysts coupled with plasma. It was observed that the Ag/ZSM5 catalyst showed better than the Cu/ZSM5 catalyst at the same conditions. NO conversion of approximately 100% in the approximate range from 200 to 300 °C and optimal NO_x removal above 80% was achieved by using the Ag/ZSM5 catalyst coupled with plasma. Furthermore, we found that the combination of plasma with the catalyst at high temperatures (>350 °C) is not needed because of two reasons as follows:

i. NO removal rate with the catalyst alone is really high, and, the addition of plasma is a waste of energy.

ii. The plasma produces NO_x, decreasing the net NO_x removal efficiency

The plasma electrical power or the appropriate energy density should be adjusted based on the exhaust gas temperature to minimize energy consumption

Simulated diesel exhaust gas was obtained by adding the naphthalene (soot simulant) to the gas stream. The removal of NO_x and naphthalene was examined in the operating temperature range from 150 to 350 °C and by varying the SIE in the range up to 210 J/L. The result indicated that the presence of plasma-enhanced the efficiency of removing NO_x and soot simulant at low temperatures. Soot can play the role of reducing agents in the NO_x removal process. However, high-efficiency NO_x removal requires an additional reducing agent. The $Ag/\alpha-Al_2O_3$ presented a narrow temperature window for NO_x and soot simulant removal. However, the presence of plasma expanded the temperature window toward low operating temperatures. As a result, the high efficiency of NO_x and soot simulant removal were obtained by using the catalyst coupled with plasma under fluctuating temperature conditions.

2. The second research has dealt with the efficient degradation of styrene in a DBD plasma-catalytic reactor over Pd/ZSM5 catalyst at room temperature. The combination of the catalyst with the plasma strongly improved the styrene oxidation and the CO_2 selectivity. The Pd/ZSM5 exhibited good catalytic activity at low temperatures under the influence of plasma, improving the mineralization of styrene. As well, the presence of the Pd/ZSM5 largely decreased the formation of secondary pollutants such as NO_2 and O_3. Ozone played an important role in the removal of styrene. The styrene oxidation reactions performed in the infrared gas cell exhibited that the combination of the plasma with the catalyst greatly reduced the formation of byproducts such as aldehydes, formic acid, and O_3.

3. The third research was performed the results provide profound and comprehensive insight into the characteristics of the plasma as well as the degradation of EA using both AC and DC honeycomb catalyst discharge under various conditions (i.e., humidity, GHSV, and temperature). The DC honeycomb catalyst discharge is more stable and easier to operate at higher voltages compared to the AC honeycomb discharge under various atmospheric conditions. Furthermore, EA conversion in the DC honeycomb catalyst discharge (96%) is significantly higher than that in the AC discharge at the given applied voltage. The DC plasma discharge in combination with the honeycomb catalyst renders the proposed system suitable for practical applications.

BIBLIOGRAPHY

[1] E. P. A. EPA, “Nitrogen Oxides (NO_x), Why and How They Are Controlled,” *http://www.epa.gov/ttn/catc/dir1/fnoxdoc.pdf*, no. November, p. 48, 1999.

[2] M. Z. Jacobson, Air Pollution and Global Warming: History, Science, and Solutions. *Cambridge University Press*, 2012.

[3] H. H. Kim, “Nonthermal plasma processing for air-pollution control: A historical review, current issues, and future prospects,” *Plasma Process. Polym.*, vol. 1, no. 2, pp. 91–110, 2004.

[4] K. Skalska, J. S. Miller, and S. Ledakowicz, “Trends in NO_x abatement: A review,” *Sci. Total Environ.*, vol. 408, no. 19, pp. 3976–3989, 2010.

[5] O. Kamat, “A review on selective catalytic reduction for NO_x Reduction,” *Int. J. Emerg. Trends Sci. Technol.*, vol. 89, no. 04, pp. 5090–5093, 2017.

[6] C. He, J. Cheng, X. Zhang, M. Douthwaite, S. Pattisson, and Z. Hao, “Recent Advances in the Catalytic Oxidation of Volatile Organic Compounds: A Review Based on Pollutant Sorts and Sources,” *Chem. Rev.*, vol. 119, no. 7, pp. 4471–4568, 2019.

[7] M. N. Kajama, N. C. Nwogu, E. Gobina, and A. T. Oxidation, “Volatile Organic Compounds Destruction by Catalytic Oxidation for Environmental Applications,” vol. 9, no. 6, pp. 635–638, 2015.

[8] B. F. Gibbs and C. N. Mulligan, “Styrene toxicity: An ecotoxicological assessment,” *Ecotoxicol. Environ. Saf.*, vol. 38, no. 3, pp. 181–194, 1997.

[9] X. Zhu *et al.*, “Enhanced performance for plasma-catalytic oxidation of ethyl acetate over La1-xCexCoO3+Δ catalysts,” *Appl. Catal. B Environ.*, vol. 213, pp. 97–105, 2017.

[10] S. Elzey, A. Mubayi, S. C. Larsen, and V. H. Grassian, “FTIR study of the selective catalytic reduction of NO2 with ammonia on nanocrystalline NaY and CuY,” *J. Mol. Catal. A Chem.*, vol. 285, no. 1–2, pp. 48–57, 2008.

[11] K. Skalska, J. S. Miller, and S. Ledakowicz, “Trends in NOx abatement: A review,” *Sci. Total Environ.*, vol. 408, no. 19, pp. 3976–3989, 2010.

[12] M. A. Gómez-García, V. Pitchon, and A. Kiennemann, “Pollution by nitrogen oxides: An approach to NOx abatement by using sorbing catalytic materials,” *Environ. Int.*, vol. 31, no. 3, pp. 445–467, 2005.

[13] J. Van Durme, J. Dewulf, C. Leys, and H. Van Langenhove, “Combining non-thermal plasma with heterogeneous catalysis in waste gas treatment: A review,” *Appl. Catal. B Environ.*, vol. 78, no. 3–4, pp. 324–333, 2008.

[14] Z. Wang, J. Zhou, Y. Zhu, Z. Wen, J. Liu, and K. Cen, “Simultaneous removal of NO_x, SO_2 and Hg in nitrogen flow in a narrow reactor by ozone injection: Experimental results,” *Fuel Process. Technol.*, vol. 88, no. 8, pp. 817–823, 2007.

[15] P. Woodrow, “Nitric oxide: Some nursing implications,” *Intensive Crit. Care Nurs.*, vol. 13, no. 2, pp. 87–92, 1997.

[16] W. Lu, Y. Abbas, M. F. Mustafa, C. Pan, and H. Wang, “A review on application of dielectric barrier discharge plasma technology on the abatement of volatile organic compounds,” *Front. Environ. Sci. Eng.*, vol. 13, no. 2, 2019.

[17] H. H. Kim, “Nonthermal plasma processing for air-pollution control: A historical review, current issues, and future prospects,” *Plasma Process. Polym.*, vol. 1, no. 2, pp. 91–110, 2004.

[18] P. Talebizadeh, M. Babaie, R. Brown, H. Rahimzadeh, Z. Ristovski, and M. Arai, “The role of non-thermal plasma technique in NO_x treatment: A review,” *Renew. Sustain.*

Energy Rev., vol. 40, no. x, pp. 886–901, 2014.

[19] K. Urashima and J. S. Chang, “Removal of volatile organic compounds from air streams and industrial flue gases by non-thermal plasma technology,” *IEEE Trans. Dielectr. Electr. Insul.*, vol. 7, no. 5, pp. 602–614, 2000.

[20] M. Tomatis, H. H. Xu, J. He, and X. D. Zhang, “Recent Development of Catalysts for Removal of Volatile Organic Compounds in Flue Gas by Combustion: A Review,” *J. Chem.*, vol. 2016, no. x, 2016.

[21] L. J. Hsu and C. C. Lin, “Removal of methanol and 1-butanol from binary mixtures by absorption in rotating packed beds with blade packings,” *Chem. Eng. J.*, vol. 168, no. 1, pp. 190–200, 2011.

[22] H. H. Kim and A. Ogata, “Interaction of nonthermal plasma with catalyst for the air pollution control,” *Int. J. Plasma Environ. Sci. Technol.*, vol. 6, no. 1, pp. 43–48, 2012.

[23] S. Veerapandian, C. Leys, N. De Geyter, and R. Morent, “Abatement of VOCs using packed bed non-thermal plasma reactors: A review,” *Catalysts*, vol. 7, no. 12, p. 113, 2017.

[24] F. I. Khan and A. K. Ghoshal, “Removal of Volatile Organic Compounds from polluted air,” *J. Loss Prev. Process Ind.*, vol. 13, no. x, pp. 527–545, 2000.

[25] S. Wang, L. Zhang, C. Long, and A. Li, “Enhanced adsorption and desorption of VOCs vapor on novel micro-mesoporous polymeric adsorbents,” *J. Colloid Interface Sci.*, vol. 428, pp. 185–190, 2014.

[26] M. V. Grabchenko, N. N. Mikheeva, G. V. Mamontov, M. A. Salaev, L. F. Liotta, and O. V. Vodyankina, “Ag/CeO_2 Composites for Catalytic Abatement of CO, Soot and VOCs,” *Catalysts*, vol. 8, no. 7, p. 285, 2018.

[27] M. S. Kamal, S. A. Razzak, and M. M. Hossain, “Catalytic oxidation of volatile organic

compounds (VOCs) - A review," *Atmos. Environ.*, vol. 140, pp. 117–134, 2016.

[28] K. Barbusinski, K. Kalemba, D. Kasperczyk, K. Urbaniec, and V. Kozik, "Biological methods for odor treatment – A review," *J. Clean. Prod.*, vol. 152, pp. 223–241, 2017.

[29] D. B. Nguyen, V. T. Nguyen, I. J. Heo, and Y. S. Mok, "Removal of NOx by selective catalytic reduction coupled with plasma under temperature fluctuation condition," *J. Ind. Eng. Chem.*, vol. 72, no. x, pp. 400–407, Apr. 2019.

[30] H. Zhang, K. Li, T. Sun, J. Jia, Z. Lou, and L. Feng, "Removal of styrene using dielectric barrier discharge plasmas combined with sol-gel prepared TiO2 coated γ-Al_2O_3," *Chem. Eng. J.*, vol. 241, pp. 92–102, 2014.

[31] A. Mizuno, "Industrial applications of atmospheric non-thermal plasma in environmental remediation," *Plasma Phys. Control. Fusion*, vol. 49, no. 5 A, 2007.

[32] K. L. L. Vercammen, A. A. Berezin, F. Lox, and J.-S. Chang, "Non-Thermal Plasma Techniques for the Reduction of Volatile Organic Compounds in Air Streams: A Critical Review," *J. Adv. Oxid. Technol.*, vol. 2, no. 2, pp. 312–329, 2017.

[33] M. Yousfi *et al.*, "Basic data for atmospheric pressure non-thermal plasma investigations in environmental and biomedical applications," *Plasma Sources Sci. Technol.*, vol. 19, no. 3, 2010.

[34] Q. Tang, W. Jiang, Y. Cheng, S. Lin, T. M. Lim, and J. Xiong, "Generation of reactive species by gas-phase dielectric barrier discharges," *Ind. Eng. Chem. Res.*, vol. 50, no. 17, pp. 9839–9846, 2011.

[35] S. Pekárek and J. Khun, "Non-thermal plasma at atmospheric pressure for ozone generation and volatile organic compounds decomposition," *acta Phys. slovaca*, vol. 56, no. 2, pp. 109–113, 2006.

[36] G. Xiao *et al.*, "Non-thermal plasmas for VOCs abatement," *Plasma Chemistry and*

Plasma Processing, vol. 34, no. 5. pp. 1033–1065, 2014.

[37] M. Ondarts, W. Hajji, J. Outin, T. Bejat, and E. Gonze, “Non-Thermal Plasma for indoor air treatment: Toluene degradation in a corona discharge at ppbv levels,” *Chem. Eng. Res. Des.*, vol. 118, pp. 194–205, 2017.

[38] D. B. Nguyen, S. Shirjana, M. M. Hossain, I. Heo, and Y. S. Mok, “Effective generation of atmospheric pressure plasma in a sandwich-type honeycomb monolith reactor by humidity control,” *Chem. Eng. J.*, vol. 401, no. June, p. 125970, 2020.

[39] Z. Yang *et al.*, “Potential demonstrations of ‘hot spots’ presence by adsorption-desorption of toluene vapor onto granular activated carbon under microwave radiation,” *Chem. Eng. J.*, vol. 319, pp. 191–199, 2017.

[40] S. Choi, M. S. Lee, and D. W. Park, “Photocatalytic performance of TiO_2/V_2O_5 nanocomposite powder prepared by DC arc plasma,” *Curr. Appl. Phys.*, vol. 14, no. 3, pp. 433–438, 2014.

[41] M. Młotek, E. Reda, P. Jóźwik, K. Krawczyk, and Z. Bojar, “Plasma-catalytic decomposition of cyclohexane in gliding discharge reactor,” *Appl. Catal. A Gen.*, vol. 505, pp. 150–158, 2015.

[42] V. T. Nguyen, D. B. Nguyen, I. Heo, and Y. S. Mok, “Efficient Degradation of Styrene in a Nonthermal Plasma–Catalytic System Over Pd/ZSM-5 Catalyst,” *Plasma Chem. Plasma Process.*, vol. 40, no. 5, pp. 1207–1220, 2020.

[43] V. T. Nguyen, D. B. Nguyen, I. Heo, D. K. Dinh, and Y. S. Mok, “Evaluation of Low-Temperature NO_x Removal Over Ag/ZSM5 and Cu/ZSM5 Catalysts Coupled With Plasma,” *IEEE Trans. PLASMA Sci.*, vol. 48, no. 7, pp. 2448–2456, 2020.

[44] M. M. Hossain *et al.*, “Nonthermal plasma in practical-scale honeycomb catalysts for the removal of toluene,” *J. Hazard. Mater.*, vol. 404, no. PB, p. 123958, 2021.

[45] V. T. Nguyen, D. B. Nguyen, I. Heo, and Y. S. Mok, “Plasma-assisted selective catalytic reduction for low-temperature removal of NOx and soot simulant,” *Catalysts*, vol. 9, no. 10, 2019.

[46] M. Magureanu, N. B. Mandache, V. I. Parvulescu, C. Subrahmanyam, A. Renken, and L. Kiwi-Minsker, “Improved performance of non-thermal plasma reactor during decomposition of trichloroethylene: Optimization of the reactor geometry and introduction of catalytic electrode,” *Appl. Catal. B Environ.*, vol. 74, no. 3–4, pp. 270–277, 2007.

[47] W. Mista and R. Kacprzyk, “Decomposition of toluene using non-thermal plasma reactor at room temperature,” *Catal. Today*, vol. 137, no. 2–4, pp. 345–349, 2008.

[48] Q. H. Trinh and Y. S. Mok, “Effect of the adsorbent/catalyst preparation method and plasma reactor configuration on the removal of dilute ethylene from air stream,” *Catal. Today*, vol. 256, no. P1, pp. 170–177, 2015.

[49] A. Baylet, P. Marécot, D. Duprez, X. Jeandel, K. Lombaert, and J. M. Tatibouët, “Synergetic effect of plasma/catalysis hybrid system for CH 4 removal,” *Appl. Catal. B Environ.*, vol. 113–114, pp. 31–36, 2012.

[50] T. Pham Huu, S. Gil, P. Da Costa, A. Giroir-Fendler, and A. Khacef, “Plasma-catalytic hybrid reactor: Application to methane removal,” *Catal. Today*, vol. 257, no. P1, pp. 86–92, 2015.

[51] J. C. Whitehead, “Plasma catalysis: A solution for environmental problems,” *Pure Appl. Chem.*, vol. 82, no. 6, pp. 1329–1336, 2010.

[52] E. C. Neyts and A. Bogaerts, “Understanding plasma catalysis through modelling and simulation - A review,” *J. Phys. D. Appl. Phys.*, vol. 47, no. 22, 2014.

[53] T. Nozaki and K. Okazaki, “Non-thermal plasma catalysis of methane: Principles, energy

efficiency, and applications," *Catal. Today*, vol. 211, pp. 29–38, 2013.

[54] Y. S. Mok and D. H. Kim, "Treatment of toluene by using adsorption and nonthermal plasma oxidation process," *Curr. Appl. Phys.*, vol. 11, no. 5 SUPPL., pp. S58–S62, 2011.

[55] Z. Jia, X. Wang, E. Foucher, F. Thevenet, and A. Rousseau, "Plasma-Catalytic Mineralization of Toluene Adsorbed on CeO_2," *Catalysts*, vol. 8, no. 8, p. 303, 2018.

[56] V. R. Chirumamilla, *Plasma-assisted catalysis for air purification*, no. 2018. 2018.

[57] T. Yamamoto, S. Member, C. Yang, M. R. Beltran, and Z. Kravets, "Plasma-Assisted Chemical Process for NO_x Control," *IEEE Trans. Ind. Appl.*, vol. 36, no. 3, pp. 923–927, 2000.

[58] T. Wang, X. Zhang, J. Liu, H. Liu, Y. Wang, and B. Sun, "Effects of temperature on NO_x removal with Mn-Cu/ZSM5 catalysts assisted by plasma," *Appl. Therm. Eng.*, vol. 130, pp. 1224–1232, 2018.

[59] S. K. P. Veerapandian, N. De Geyter, J.-M. Giraudon, J.-F. Lamonier, and R. Morent, "The use of zeolites for VOCs abatement by combining Non-thermal plasma, adsorption, and/or catalysis: A Review," *Catalysts*, vol. 9, no. 1, p. 98, 2019.

[60] K. Abedi, F. Ghorbani-Shahna, B. Jaleh, A. Bahrami, and R. Yarahmadi, "Enhanced performance of non-thermal plasma coupled with TiO_2/GAC for decomposition of chlorinated organic compounds: Influence of a hydrogen-rich substance," *J. Environ. Heal. Sci. Eng.*, vol. 12, no. 1, pp. 1–13, 2014.

[61] J. Jolibois, K. Takashima, and A. Mizuno, "Application of a non-thermal surface plasma discharge in wet condition for gas exhaust treatment: NO_x removal," *J. Electrostat.*, vol. 70, no. 3, pp. 300–308, 2012.

[62] C. Qin, X. Dang, J. Huang, J. Teng, and X. Huang, "Plasma-catalytic oxidation of adsorbed toluene on Ag-Mn/γ-Al_2O_3: Comparison of gas flow-through and gas

circulation treatment," *Chem. Eng. J.*, vol. 299, pp. 85–92, 2016.

[63] C. Norsic, J. M. Tatibouët, C. Batiot-Dupeyrat, and E. Fourré, "Non thermal plasma assisted catalysis of methanol oxidation on Mn, Ce and Cu oxides supported on γ-Al_2O_3," *Chem. Eng. J.*, vol. 304, pp. 563–572, 2016.

[64] G. C. Dhal, S. Dey, D. Mohan, and R. Prasad, "Simultaneous control of NO_x-soot by substitutions of Ag and K on perovskite ($LaMnO_3$) catalyst," *Bull. Chem. React. Eng. Catal.*, vol. 13, no. 1, pp. 144–154, 2018.

[65] M. Mihet and M. D. Lazar, "Effect of Pd and Rh promotion on Ni/Al_2O_3 for NO reduction by hydrogen for stationary applications," *Chem. Eng. J.*, vol. 251, pp. 310–318, 2014.

[66] A. M. Vandenbroucke, R. Morent, N. De Geyter, and C. Leys, "Non-thermal plasmas for non-catalytic and catalytic VOC abatement," *J. Hazard. Mater.*, vol. 195, no. x, pp. 30–54, 2011.

[67] H. H. Kim, Y. Teramoto, T. Sano, N. Negishi, and A. Ogata, "Effects of Si/Al ratio on the interaction of nonthermal plasma and Ag/HY catalysts," *Appl. Catal. B Environ.*, vol. 166–167, pp. 9–17, 2015.

[68] M. Stöcker, "Gas phase catalysis by zeolites," *Microporous Mesoporous Mater.*, vol. 82, no. 3, pp. 257–292, 2005.

[69] Y. R. Zhang, K. Van Laer, E. C. Neyts, and A. Bogaerts, "Can plasma be formed in catalyst pores? A modeling investigation," *Appl. Catal. B Environ.*, vol. 185, pp. 56–67, 2016.

[70] M. Trueba and S. P. Trasatti, "γ-alumina as a support for catalysts: A review of fundamental aspects," *Eur. J. Inorg. Chem.*, no. 17, pp. 3393–3403, 2005.

[71] M. Fu *et al.*, "A review on selective catalytic reduction of NOx by supported catalysts at 100-300°C - Catalysts, mechanism, kinetics," *Catal. Sci. Technol.*, vol. 4, no. 1, pp. 14–

25, 2014.

[72] Q. Sun, X.-F. Yang, J.-H. Niu, Y.Xu, Z.-M. Song, and J. Liu, “Selective catalytic reduction of NOx in dielectric barrier discharge,” *Eur. Phys. J. - Appl. Phys.*, vol. 30, no. x, pp. 129–133, 2005.

[73] B. J. Lee, H. C. Kang, J. O. Jo, and Y. S. Mok, “Consideration of the role of plasma in a plasma-coupled selective catalytic reduction of nitrogen oxides with a hydrocarbon reducing agent,” *Catalysts*, vol. 7, no. 11, 2017.

[74] C. M. A. S. Freitas, O. S. G. P. Soares, J. J. M. Órfão, A. M. Fonseca, M. F. R. Pereira, and I. C. Neves, “Highly efficient reduction of bromate to bromide over mono and bimetallic ZSM5 catalysts,” *Green Chem.*, vol. 17, no. 8, pp. 4247–4254, 2015.

[75] M. Lu, R. Huang, J. Wu, M. Fu, L. Chen, and D. Ye, “On the performance and mechanisms of toluene removal by FeOx/SBA-15-assisted non-thermal plasma at atmospheric pressure and room temperature,” *Catal. Today*, vol. 242, no. PB, pp. 274–286, 2015.

[76] L. Castoldi *et al.*, “Silver-based catalytic materials for the simultaneous removal of soot and NOx,” *Catal. Today*, vol. 258, pp. 405–415, 2015.

[77] Q. H. Trinh, S. B. Lee, and Y. S. Mok, “Removal of ethylene from air stream by adsorption and plasma-catalytic oxidation using silver-based bimetallic catalysts supported on zeolite,” *J. Hazard. Mater.*, vol. 285, pp. 525–534, 2015.

[78] C. Xu, W. Sun, L. Cao, and J. Yang, “Selective catalytic reduction of nitric oxide by hydrogen over $NiFe_2$-$xPdxO_4$ catalysts at low temperature,” *Chem. Eng. J.*, vol. 283, pp. 1137–1144, 2016.

[79] M. A. Goula *et al.*, “A comparative study of the H_2-assisted selective catalytic reduction of nitric oxide by propene over noble metal (Pt, Pd, Ir)/γ-Al_2O_3 catalysts,” *J. Environ.*

Chem. Eng., vol. 4, no. 2, pp. 1629–1641, 2016.

[80] F. Gao *et al.*, A Review on Selective Catalytic Reduction of NO_x by NH_3 over Mn–Based Catalysts at Low Temperatures: Catalysts, Mechanisms, Kinetics and DFT Calculations," *Catalysts*, vol. 7, no. 7. 2017.

[81] Y. Miao, L. Der Chen, Y. He, and T. wei Kuo, "Study of SCR cold-start by energy method," *Chem. Eng. J.*, vol. 155, no. 1–2, pp. 260–265, 2009.

[82] K. Arve, F. Klingstedt, K. Eränen, J. Wärnå, L. E. Lindfors, and D. Y. Murzin, "Kinetics of NO_x reduction over Ag/alumina by higher hydrocarbon in excess of oxygen," *Chem. Eng. J.*, vol. 107, no. 1–3, pp. 215–220, 2005.

[83] Z.-S. Zhang, M. Crocker, and B.-B. Chen, "Non-thermal plasma-assisted NO_x storage and reduction over cobalt-containing LNT catalysts," *Catal. Today 258*, pp. 386–395, 2015.

[84] B. K. Cho *et al.*, "Selective catalytic reduction of NO_x by diesel fuel: Plasma-assisted HC/SCR system," *Catal. Today*, vol. 191, no. 1, pp. 20–24, 2012.

[85] L.-H. Tsui, V. Stetsovych, B. Pereda-ayo, and J. R. González-velasco, "NO_x Storage and Reduction for Diesel Engine Exhaust Aftertreatment," *Diesel Engine Combust. Emiss. Cond. Monit.*, no. x, p. 266, 2015.

[86] H. J. Curran, P. Gaffuri, W. J. Pitz, and C. K. Westbrook, "A comprehensive modeling study of n-heptane oxidation," *Combust. Flame*, vol. 114, no. 1–2, pp. 149–177, 1998.

[87] B. Yang, M. Yao, W. K. Cheng, Y. Li, Z. Zheng, and S. Li, "Experimental and numerical study on different dual-fuel combustion modes fuelled with gasoline and diesel," *Appl. Energy*, vol. 113, pp. 722–733, 2014.

[88] Y. Li, H. Guo, and H. Li, "Evaluation of Kinetics Process in CFD Model and Its Application in Ignition Process Analysis of a Natural Gas-Diesel Dual Fuel Engine," *SAE*

Tech. Pap., vol. 2017-March, no. March, 2017.

[89] J. C. S. M. Iwamoto, H. Furukawa, Y. Mine, F. Uemura, S.I. Mikuriya, S. Kagawa, “123,” *Chem. Commun*, pp. 1272–1273, 1986.

[90] R. McAdams, “Prospects for non-thermal atmospheric plasmas for pollution abatement,” *J. Phys. D. Appl. Phys.*, vol. 34, no. 18, pp. 2810–2821, 2001.

[91] S. Futamura, H. Einaga, and A. Zhang, “Comparison of reactor performance in the nonthermal plasma chemical processing of hazardous air pollutants,” *IEEE Trans. Ind. Appl.*, vol. 37, no. 4, pp. 978–985, 2001.

[92] V. Tomašić, “Application of the monoliths in DeNO$_x$ catalysis,” *Catal. Today*, vol. 119, no. 1–4, pp. 106–113, 2007.

[93] T. H. E. Electric, C. Of, and T. H. E. Ozonator, “The electric characteristics of the ozonator discharge,” vol. 16, no. 1909, pp. 450–460, 1943.

[94] S. Mahammadunnisa, P. Manoj Kumar Reddy, E. Linga Reddy, and C. Subrahmanyam, “Catalytic DBD plasma reactor for CO oxidation by in situ N$_2$O decomposition,” *Catal. Today*, vol. 211, pp. 53–57, 2013.

[95] D. B. Nguyen, I. J. Heo, and Y. S. Mok, “Enhanced performance at an early state of hydrocarbon selective catalyst reduction of NO$_x$ by atmospheric pressure plasma,” *J. Ind. Eng. Chem.*, vol. 68, no. x, pp. 372–379, Dec. 2018.

[96] T. T. Yang, H. T. Bi, and X. Cheng, “Effects of O$_2$, CO$_2$ and H$_2$O on NO$_x$ adsorption and selective catalytic reduction over Fe/ZSM-5,” *Appl. Catal. B Environ.*, vol. 102, no. 1–2, pp. 163–171, 2011.

[97] M. Anpo, M. Matsuoka, H. Mishima, and H. Yamashita, “The design of photocatalysts for the removal of NO$_x$ at normal temperatures - Copper (I) and silver (I) ion catalysts anchored within zeolite cavities,” *Res. Chem. Intermed.*, vol. 23, no. 3, pp. 197–217,

1997.

[98] J. C. Groen, L. A. A. Peffer, and J. Pérez-Ramírez, "Pore size determination in modified micro- and mesoporous materials. Pitfalls and limitations in gas adsorption data analysis," *Microporous Mesoporous Mater.*, vol. 60, no. 1–3, pp. 1–17, 2003.

[99] J. C. Groen, L. A. A. Peffer, J. A. Moulijn, and J. Pérez-Ramírez, "On the introduction of intracrystalline mesoporosity in zeolites upon desilication in alkaline medium," *Microporous Mesoporous Mater.*, vol. 69, no. 1–2, pp. 29–34, 2004.

[100] J. Despres, M. Koebel, O. Kröcher, M. Elsener, and A. Wokaun, "Adsorption and desorption of NO and NO_2 on Cu-ZSM-5," *Microporous Mesoporous Mater.*, vol. 58, no. 2, pp. 175–183, 2003.

[101] Y. Sun Mok and E. Young Yoon, "Effect of ozone injection on the catalytic reduction of nitrogen oxides," *Ozone Sci. Eng.*, vol. 28, no. 2, pp. 105–110, 2006.

[102] M. Arai, M. Saito, and S. Yoshinaga, "Effect of oxygen on NO_x removal in corona discharge field: NO_x behavior without a reducing agent," *Combust. Sci. Technol.*, vol. 176, no. 10, pp. 1653–1665, 2004.

[103] B. Eliasson and U. Kogelschatz, "Modeling and Applications of Silent Discharge Plasmas," *IEEE Trans. Plasma Sci.*, vol. 19, no. 2, pp. 309–323, 1991.

[104] H. E. Wagner, R. Brandenburg, K. V. Kozlov, A. Sonnenfeld, P. Michel, and J. F. Behnke, "The barrier discharge: Basic properties and applications to surface treatment," *Vacuum*, vol. 71, no. 3 SPEC., pp. 417–436, 2003.

[105] R. Brandenburg and R. Brandenburg, "Dielectric barrier discharges : progress on plasma sources and on the understanding of regimes and single fi laments," *Plasma Sources Sci. Technol.*, vol. 26, p. 053001, 2017.

[106] A. Jahanmiri, M. R. Rahimpour, M. Mohamadzadeh Shirazi, N. Hooshmand, and H.

Taghvaei, “Naphtha cracking through a pulsed DBD plasma reactor: Effect of applied voltage, pulse repetition frequency and electrode material,” *Chem. Eng. J.*, vol. 191, pp. 416–425, 2012.

[107] A. Fridman, “Plasma chemistry,” *Plasma Chem.*, vol. 9780521847, pp. 1–978, 2008.

[108] A. Khacef, P. Da Costa, and G. Djéga-Mariadassou, “Plasma Assisted Catalyst for NO_x Remediation from Lean Gas Exhaust,” *J. Eng. Technol. Res.*, vol. 1, no. 1, pp. 112–122, 2013.

[109] R. Gholami, C. E. Stere, A. Goguet, and C. Hardacre, “Non-thermal-plasma-activated de-NO_x catalysis,” *Philos. Trans. R. Soc. A Math. Phys. Eng. Sci.*, vol. 376, no. 2110, p. 20170054, Jan. 2018.

[110] Q. Sun, A. Zhu, X. Yang, J. Niu, and Y. Xu, “Formation of NO_x from N_2 and O_2 in catalyst-pellet filled dielectric barrier discharges at atmospheric pressure,” *Chem. Commun.*, vol. 9, no. 12, pp. 1418–1419, 2003.

[111] G. Landi, L. Lisi, R. Pirone, G. Russo, and M. Tortorelli, “Effect of water on NO adsorption over Cu-ZSM-5 based catalysts,” *Catal. Today*, vol. 191, no. 1, pp. 138–141, 2012.

[112] K. Shimizu, T. Hirano, and T. Oda, “Effect of water vapor and hydrocarbons in removing NO_x by using nonthermal plasma and catalyst,” *IEEE Trans. Ind. Appl.*, vol. 37, no. 2, pp. 464–471, 2001.

[113] K. E. Voss *et al.*, “Plasma-Assisted Catalytic Reduction of NO_x,” *SAE Tech. Pap. Ser.*, 1998.

[114] J. O. Jo and Y. S. Mok, “Conversion of NO_x by plasma-hydrocarbon Selective Catalytic Reduction Process,” *Appl. Chem. Eng*, vol. 29, pp. 103–111, 2018.

[115] B. M. Penetrante *et al.*, “Plasma-assisted heterogeneous catalysis for NO_x reduction in

lean-burn engine exhaust.” p. Proceedings of the 1997 Diesel Engine Emissions Re.

[116] I. Jõgi, K. Erme, E. Levoll, J. Raud, and E. Stamate, “Plasma and catalyst for the oxidation of NO_x,” *Plasma Sources Sci. Technol.*, vol. 27, no. 3, 2018.

[117] D. B. Nguyen and W. G. Lee, “Implementation of alternative gas compositions and effects on discharge properties of atmospheric pressure plasma in decomposition of CHF_3,” *J. Ind. Eng. Chem.*, vol. 52, pp. 7–11, 2017.

[118] D. B. Nguyen and W. G. Lee, “Effects of self-heating in a dielectric barrier discharge reactor on CHF3 decomposition,” *Chem. Eng. J.*, vol. 294, pp. 58–64, 2016.

[119] F. Portet-Koltalo and N. Machour, “Analytical Methodologies for the Control of Particle-Phase Polycyclic Aromatic Compounds from Diesel Engine Exhaust,” *Diesel Engine - Combust. Emiss. Cond. Monit.*, 2013.

[120] C. Liu *et al.*, “Plasma application for more environmentally friendly catalyst preparation,” *Pure Appl. Chem.*, vol. 78, no. 6, pp. 1227–1238, 2006.

[121] M. S. Gandhi, A. Ananth, Y. S. Mok, J. I. Song, and K. H. Park, “Effect of porosity of α-alumina on non-thermal plasma decomposition of ethylene in a dielectric-packed bed reactor,” *Res. Chem. Intermed.*, vol. 40, no. 4, pp. 1483–1493, 2014.

[122] Z. Bo, J. H. Yan, X. D. Li, Y. Chi, K. F. Cen, and B. G. Chéron, “Effects of oxygen and water vapor on volatile organic compounds decomposition using gliding arc gas discharge,” *Plasma Chem. Plasma Process.*, vol. 27, no. 5, pp. 546–558, 2007.

[123] H. L. Chen, H. M. Lee, S. H. Chen, and M. B. Chang, “Review of packed-bed plasma reactor for ozone generation and air pollution control,” *Ind. Eng. Chem. Res.*, vol. 47, no. 7, pp. 2122–2130, 2008.

[124] K. Sekiguchi, A. Sanada, and K. Sakamoto, “Degradation of toluene with an ozone-decomposition catalyst in the presence of ozone, and the combined effect of TiO_2

addition," *Catal. Commun.*, vol. 4, no. 5, pp. 247–252, 2003.

[125] P. Konova, M. Stoyanova, A. Naydenov, S. Christoskova, and D. Mehandjiev, "Catalytic oxidation of VOCs and CO by ozone over alumina supported cobalt oxide," *Appl. Catal. A Gen.*, vol. 298, no. 1–2, pp. 109–114, 2006.

[126] T. Zhu, J. Li, Y. Jin, Y. Liang, and G. Ma, "Decomposition of benzene by non-thermal plasma processing: Photocatalyst and ozone effect," *Int. J. Environ. Sci. Technol.*, vol. 5, no. 3, pp. 375–384, 2008.

[127] V. Demidiouk and Jae Ou Chae, "Decomposition of volatile organic compounds in plasma-catalytic system," *IEEE Trans. Plasma Sci.*, vol. 33, no. 1, pp. 157–161, Feb. 2005.

[128] N. Jiang, N. Lu, K. Shang, J. Li, and Y. Wu, "Innovative approach for benzene degradation using hybrid surface/packed-bed discharge plasmas," *Environ. Sci. Technol.*, vol. 47, no. 17, pp. 9898–9903, 2013.

[129] J. Mo, Y. Zhang, Q. Xu, J. J. Lamson, and R. Zhao, "Photocatalytic purification of volatile organic compounds in indoor air: A literature review," *Atmos. Environ.*, vol. 43, no. 14, pp. 2229–2246, 2009.

[130] A. Ogata, D. Ito, K. Mizuno, S. Kushiyama, A. Gal, and T. Yamamoto, "Effect of coexisting components on aromatic decomposition in a packed-bed plasma reactor," *Appl. Catal. A Gen.*, vol. 236, no. 1–2, pp. 9–15, 2002.

[131] H. Kohno, A. A. Berezin, and J. S. Chang, "Destruction of volatile organic compounds used in a semiconductor industry by a capillary tube discharge reactor," *IEEE Trans. Ind. Appl.*, vol. 34, no. 5, pp. 953–966, 1998.

[132] M. R. Mas Haris, S. Kathiresan, and S. Mohan, "FT-IR and FT-Raman spectra and normal coordinate analysis of poly methyl methacrylate," *Der Pharma Chem.*, vol. 2, no.

4, pp. 316–323, 2010.

[133] M. T. Islam, N. Rodríguez-Hornedo, S. Ciotti, and C. Ackermann, "Fourier transform infrared spectroscopy for the analysis of neutralizer-carbomer and surfactant-carbomer interactions in aqueous, hydroalcoholic and anhydrous gel formulations," *AAPS J.*, vol. 6, no. 4, pp. 4–10, 2004.

[134] T. Zhu, "Removal of VOCs Using Nonthermal Plasma Technology," *Chem. Emiss. Control. Radioact. Pollut. Indoor Air Qual.*, 2011.

[135] A. Eid, K. Takashima, and A. Mizuno, "Experimental Study of Dielectric-Barrier-Discharge Reactor for Plasma- Assisted-Combustion," vol. 9, no. 2, pp. 120–126, 2015.

[136] S. Sato and A. Mizuno, "NO_x Removal of Simulated Diesel Exhaust with Honeycomb Discharge," *Int. J. Plasma Environ. Sci. Technol.*, vol. 4, no. 1, pp. 18–23, 2010.

[137] S. Sato, K. Hensel, H. Hayashi, K. Takashima, and A. Mizuno, "Honeycomb discharge for diesel exhaust cleaning," *J. Electrostat.*, vol. 67, no. 2–3, pp. 77–83, 2009.

[138] S. Govender and H. B. Friedrich, "Monoliths: A review of the basics, preparation methods and their relevance to oxidation," *Catalysts*, vol. 7, no. 2, 2017.

[139] S. Hosseini, H. Moghaddas, S. Masoudi Soltani, and S. Kheawhom, "Technological Applications of Honeycomb Monoliths in Environmental Processes: A review," *Process Saf. Environ. Prot.*, vol. 133, pp. 286–300, 2020.

[140] A. Mizuno, "Generation of non-thermal plasma combined with catalysts and their application in environmental technology," *Catal. Today*, vol. 211, pp. 2–8, 2013.

[141] K. Hensel, S. Sato, and A. Mizuno, "Sliding discharge inside glass capillaries," *IEEE Trans. Plasma Sci.*, vol. 36, no. 4 PART 1, pp. 1282–1283, 2008.

[142] K. Hensel, S. Katsura, and A. Mizuno, "DC microdischarges inside porous ceramics," *IEEE Trans. Plasma Sci.*, vol. 33, no. 2 I, pp. 574–575, 2005.

[143] K. Hensel, “Microdischarges in ceramic foams and honeycombs,” *Eur. Phys. J. D*, vol. 54, no. 2, pp. 141–148, 2009.

[144] W. S. Kang, D. H. Lee, J. O. Lee, M. Hur, and Y. H. Song, “Combination of plasma with a honeycomb-structured catalyst for automobile exhaust treatment,” *Environ. Sci. Technol.*, vol. 47, no. 19, pp. 11358–11362, 2013.

[145] F. Feng *et al.*, “Characteristics of back corona discharge in a honeycomb catalyst and its application for treatment of volatile organic compounds,” *Environ. Sci. Technol.*, vol. 49, no. 11, pp. 6831–6837, 2015.

[146] T. Kuroki, T. Fujioka, R. Kawabata, M. Okubo, and T. Yamamoto, “Regeneration of honeycomb zeolite by nonthermal plasma desorption of toluene,” *IEEE Trans. Ind. Appl.*, vol. 45, no. 1, pp. 10–15, 2009.

[147] T. Kuroki, T. Fujioka, M. Okubo, and T. Yamamoto, “Toluene concentration using honeycomb nonthermal plasma desorption,” *Thin Solid Films*, vol. 515, no. 9, pp. 4272–4277, 2007.

[148] D. M. Gómez *et al.*, “A novel CoO_x/La-modified-CeO_2 formulation for powdered and washcoated onto cordierite honeycomb catalysts with application in VOCs oxidation,” *Appl. Catal. B Environ.*, vol. 144, pp. 425–434, 2014.

[149] X. Zhu *et al.*, “La0.8M0.2MnO3 (M = Ba, Ca, Ce, Mg and Sr) perovskite catalysts for plasma-catalytic oxidation of ethyl acetate,” *Catal. Commun.*, vol. 92, pp. 35–39, 2017.

[150] T. Guo *et al.*, “Real-time analysis of intermediate products from non-thermal plasma degradation of ethyl acetate in air using PTR-MS: Performance evaluation and mechanism study,” *Chemosphere*, vol. 264, 2021.

[151] C. Díaz, M. L. Valenzuela, C. Rios, and M. Segovia, “Oxidation facility by a temperature dependence on the metal noble nanostructured $M°/M_xO_y$ phase products using a solid

state method: The case of Pd," *J. Chil. Chem. Soc.*, vol. 61, no. 4, pp. 3273–3276, 2016.

[152] A. C. Mitchell and W. J. Nellis, "Equation of state and electrical conductivity of water and ammonia shocked to the 100 GPa (1 Mbar) pressure range," *J. Chem. Phys.*, vol. 76, no. 12, pp. 6273–6281, 1982.

[153] D. Liu, J. Niu, and N. Yu, " Optical emission characteristics of medium- to high-pressure N 2 dielectric barrier discharge plasmas during surface modification of polymers ," *J. Vac. Sci. Technol. A Vacuum, Surfaces, Film.*, vol. 29, no. 6, p. 061506, 2011.

[154] B. Sun, M. Sato, and J. S. Clements, "Optical study of active species produced by a pulsed streamer corona discharge," *J. Electrostat.*, vol. 39, no. 3, pp. 189–202, 1997.

[155] Z. Yang *et al.*, "Degradation of metronidazole by dielectric barrier discharge," *Front. Environ. Sci. Eng.*, vol. 13, no. 3, pp. 1–9, 2019.

[156] S. F. Miral, E. Monette, R. Bartnikas, G. Czeremuszkin, and M. R. Wertheimer, "Electrical and optical diagnostics of DBD in He and N2 for polymer-treatment," *Plasmas Polym.*, vol. 5, no. 2, pp. 63–77, 2000.

[157] W. S. Kijlstra, J. C. M. L. Daamen, J. M. Van De Graaf, B. Van Der Linden, E. K. Poels, and A. Bliek, "Inhibiting and deactivating effects of water on the selective catalytic reduction of nitric oxide with ammonia over MnOx/ Al2O3," *Appl. Catal. B Environ.*, vol. 7, no. 3–4, pp. 337–357, 1996.

[158] J. Kitayama and M. Kuzumoto, "Analysis of ozone generation from air in silent discharge," *J. Phys. D. Appl. Phys.*, vol. 32, no. 23, pp. 3032–3040, 1999.

[159] Y. Cai *et al.*, "Plasma-catalytic decomposition of ethyl acetate over LaMO3 (M = Mn, Fe, and Co) perovskite catalysts," *J. Ind. Eng. Chem.*, vol. 70, pp. 447–452, 2019.

[160] H. Yu, W. Hu, J. He, and Z. Ye, "Decomposition efficiency and aerosol by-products of toluene, ethyl acetate and acetone using dielectric barrier discharge technique,"

Chemosphere, vol. 237, no. X, p. 124439, 2019.

[161] H. Wang, S. Chen, Z. Wang, Y. Zhou, and Z. Wu, "A novel hybrid Bi2MoO6-MnO2 catalysts with the superior plasma induced pseudo photocatalytic-catalytic performance for ethyl acetate degradation," *Appl. Catal. B Environ.*, vol. 254, no. May, pp. 339–350, 2019.

[162] X. Fan, T. L. Zhu, M. Y. Wang, and X. M. Li, "Removal of low-concentration BTX in air using a combined plasma catalysis system," *Chemosphere*, vol. 75, no. 10, pp. 1301–1306, 2009.

[163] R. Huang *et al.*, "Enhancement of the non-thermal plasma-catalytic system with different zeolites for toluene removal," *RSC Adv.*, vol. 5, no. 88, pp. 72113–72120, 2015.

[164] Y. F. Guo, D. Q. Ye, K. F. Chen, J. C. He, and W. L. Chen, "Toluene decomposition using a wire-plate dielectric barrier discharge reactor with manganese oxide catalyst in situ," *J. Mol. Catal. A Chem.*, vol. 245, no. 1–2, pp. 93–100, 2006.

[165] C. Zheng *et al.*, "Experimental study of acetone removal by packed-bed dielectric barrier discharge reactor," *J. Ind. Eng. Chem.*, vol. 20, no. 5, pp. 2761–2768, 2014.

[166] M. R. Nimlos, E. J. Wolfrum, M. L. Brewer, J. A. Fennell, and G. Bintner, "Gas-phase heterogeneous photocatalytic oxidation of ethanol: Pathways and kinetic modeling," *Environ. Sci. Technol.*, vol. 30, no. 10, pp. 3102–3110, 1996.

[167] J. E. Sawyer, "Reaction pathways during the oxidation of ethyl acetate on a platinum/alumina catalyst," *Fuel Energy Abstr.*, vol. 36, no. 1, p. 54, 1995.

[168] T. Xin, T. Nozaki, and J. C. Whitehead, *Plasma Catalysis*. 2019.

[169] A. M. Harling, D. J. Glover, J. C. Whitehead, and K. Zhang, "The role of ozone in the plasma-catalytic destruction of environmental pollutants," *Appl. Catal. B Environ.*, vol. 90, no. 1–2, pp. 157–161, 2009.

[170] F. Holzer, U. Roland, and F. D. Kopinke, “Combination of non-thermal plasma and heterogeneous catalysis for oxidation of volatile organic compounds. Part 1. Accessibility of the intra-particle volume,” *Appl. Catal. B Environ.*, vol. 38, no. 3, pp. 163–181, 2002.

[171] J. J. Manion, R. Huie, R. Levin, D. Burgess Jr, V. Orkin, W. Tsang, W. McGivern, W. M. Hudgens, V. Knyazev, D. Atkinson, E. Chai, A. Tereza, C. Lin, T. Allison, and D. F. F. Westley, J. Herron, R.F. Hampson, “NIST Chemical Kinetics Database, Standard Reference Database 17, Version 7.0.” p. Web address: http://kinetics.nist.gov, 2020.

LIST OF PUBLICATIONS

❖ Journal publications

1. **V. T. Nguyen**, D. B. Nguyen, I. Heo, and Y. S. Mok, "Plasma-assisted selective catalytic reduction for low-temperature removal of NO_x and soot simulant," Catalysts, vol. 9, no. 10, 2019.
2. **V. T. Nguyen**, D. B. Nguyen, I. Heo, D. K. Dinh, and Y. S. Mok, "Evaluation of Low-Temperature NO_x Removal Over Ag/ZSM5 and Cu/ZSM5 Catalysts Coupled With Plasma," IEEE Trans. PLASMA Sci., vol. 48, no. 7, pp. 2448–2456, 2020.
3. **V. T. Nguyen**, D. B. Nguyen, I. Heo, and Y. S. Mok, "Efficient Degradation of Styrene in a Nonthermal Plasma–Catalytic System Over Pd/ZSM-5 Catalyst," Plasma Chem. Plasma Process., vol. 40, no. 5, pp. 1207–1220, 2020.
4. **V. T. Nguyen**, D. B. Nguyen, Y. S. Mok, M.M. Hossain, Shirjana Saud, Duy Khoe Dinh, Seungmin Ryu, Hyungwon Jeon, and Seong Bong Kim, "Removal of ethyl acetate in air by using different types of corona discharges generated in a honeycomb monolith structure coated with Pd/γ-alumina", J. Hazard. Mater, 2021.
5. D. B. Nguyen, **V. T. Nguyen**, I. J. Heo, and Y. S. Mok, "Removal of NO_x by selective catalytic reduction coupled with plasma under temperature fluctuation condition," J. Ind. Eng. Chem., vol. 72, no. x, pp. 400–407, Apr. 2019.

ACKNOWLEDGMENTS

First of all, I would like to express my sincere gratitude to my supervisor, **Professor, Dr. Young Sun Mok**. Thank you for believing in me and giving me this opportunity. Your excellent guidance, constant support on my research, and life in Korea are invaluable which has motivated me to complete the course of my Ph.D.

I would like to thank the rest of my dissertation committee members: Professor, Dr. Howon Lee; Professor, Dr. Heonju Lee; Professor, Dr. Hyomin Lee; and Dr. Duy Khoe Dinh. They have offered their time and support to enable me to complete my thesis.

My sincere appreciation goes to Dr. Nguyen Duc Ba and Dr. Dinh Duy Khoe for their willingness to discuss any difficulty I experienced throughout my research, offering their invaluable knowledge to help me along the way.

I should definitely convey my gratitude to Dr. Kim, I should accept that I could not have finished my thesis without your contribution. It is amazing that you are patient in dealing with my experimental material ordering and fix anything in the lab.

I feel happy to thank the staff of the Chemical & Biological Engineering Department for their kindness and great help in official issues during this course. Miss. Lee So Jung: I cannot thank you enough for all the help and support you have offered me.

My great appreciation also goes to other members of Prof. Mok's laboratory: Dr. Moopri Singer Pandiyarajan, Dr. Mokter Md. Hossain, Mr. Byeong Ju Lee, Miss. Dilafruz Kulmatova, Mr. Roshan, Miss. Saud Shirjana, Mr. Selven, Mr. Nosir, Mr. Kyeong Hwan Yoon, and Miss. SoShi for their kind help, cooperation, and creating a friendly environment in the laboratory.

I also thank the Jeju National University and the BK21 (Brain Korea 21 Program for

Leading Universities & Students) plus fellowship for providing me the financial support. A very special thanks to all the sponsors of the project who extended their financial support and sponsored this research.

I would like to express my deepest gratitude to the country of Korea. The friendliness, kindness of the people, and a civilized living environment have helped me have a great experience and accumulate a lot of useful knowledge. I love Korea.

Most of all, special thanks to my wonderful family. This thesis would not have been possible without the love and support from my parents. I am indebted to them for their belief and for allowing me to do what I wish in my life. Especially, great thanks with love to my wife for her understanding, trusting, and taking care of my family members while I'm away from home.

I would like to thank all those whom I have not mentioned above but helped me in numerous ways to my success. Above all, I wish for everyone to be happy and healthy.

NGUYEN VAN TOAN